基于离子阱系统的量子光学实验研究

（申请清华大学理学博士学位论文）

培 养 单 位 ： 交 叉 信 息 研 究 院

学　　　科 ： 物 理 学

研 究 生 ： 吕 定 顺

指 导 教 师 ： 金 奇 奂　副 教 授

二〇一八年五月

Experimental study of quantum optics in a trapped ion system

Dissertation Submitted to

Tsinghua University

in partial fulfillment of the requirement

for the degree of

Doctor of Philosophy

in

Physics

by

Lv Dingshun

Dissertation Supervisor :   Associate Professor Kihwan Kim

May, 2018

关于学位论文使用授权的说明

本人完全了解清华大学有关保留、使用学位论文的规定，即：

清华大学拥有在著作权法规定范围内学位论文的使用权，其中包括：（1）已获学位的研究生必须按学校规定提交学位论文，学校可以采用影印、缩印或其他复制手段保存研究生上交的学位论文；（2）为教学和科研目的，学校可以将公开的学位论文作为资料在图书馆、资料室等场所供校内师生阅读，或在校园网上供校内师生浏览部分内容；（3）根据《中华人民共和国学位条例暂行实施办法》，向国家图书馆报送可以公开的学位论文。

本人保证遵守上述规定。

（保密的论文在解密后应遵守此规定）

作者签名：＿＿＿＿＿＿＿＿　　　导师签名：＿＿＿＿＿＿＿＿

日　　期：＿＿＿＿＿＿＿＿　　　日　　期：＿＿＿＿＿＿＿＿

摘　要

量子拉比模型是描述二能级系统和玻色场之间的相互作用的模型, 也可以说是描述光与物质相互作用的最简单、最基础的模型。毫无疑问，量子拉比模型是在量子光学领域被理论和实验大量研究的著名模型。当光与物质的耦合强度g与玻色场模式频率相比要小很多的情况下，量子拉比模型在旋转波近似后退化到Jaynes- Cummings模型。离子阱系统以其高保真度的态制备、态测量以及精密的态操纵而闻名。这些特征使离子阱系统成为进一步研究Jaynes- Cummings模型和在旋转波近似无效下的量子拉比模型的理想的实验平台。在本论文中，我们使用被囚禁在线性射频Paul阱中的单个$^{171}Yb^+$离子。我们把离子的两个超精细能级当作自旋1/2系统, 并通过收集荧光来检测自旋状态。我们应用真空态测量的方法来研究Jaynes-Cummings模型在相空间中的动力学，通过Q函数状态演化。我们在相空间中观察到了期间初始相干态高斯峰的分裂和围绕原点的旋转。我们通过最小二乘法，重构了密度矩阵，并得到了相应的Wigner函数，其负值，表明了非经典态的出现。此外，我们通过失谐双边带激光模拟了不同耦合强度下的量子拉比模型.其所展示的量子模拟的可调控性使我们能够在实验中详细的研究量子拉比模型，如发生在超强耦合 $(0.1 < g/\omega_m)$ 和深强耦合 $(g/\omega_m > 1)$ 情况下的广泛的难以观测到的现象。在本文中，我们绝热地制备量子拉比模型的基态，在深强耦合状态下，我们检测到玻色场和二能级系统之间的量子纠缠。此外，当耦合强度增加时，我们观察到旋转波近似的失效，以及在达到深强耦合状态时，我们观测到了声子波包的周期性来回移动。

关键词：离子阱；量子光学； Jaynes-Cummings model；量子拉比模型；真空态测量；绝热

Abstract

The quantum Rabi model(QRM) is arguably one of the most fundamental models describing quantum light-matter interaction, which consists a quantum two-level system and a bosonic field. It is a famous model that has been theoretically and experimentally studied in the context of quantum optics. When the coupling strength g is much smaller compared to that of the bosonic field mode frequency ω_m, it can reduce to the Jaynes-Cummings model(JCM) after the rotating wave approximation. The trapped ion system are well known for the high fidelity state preparation, state read-out and more importantly the precise and versatility control of the ion-laser interaction. These features render the trapped ion system a ideal platform to further study the JCM and QRM, when the rotating wave approximation is not valid. In this thesis, we use a single $^{171}\mathrm{Yb}^+$ ion trapped in a linear radio-frequency Paul trap. Two of the hyperfine states of the ion serve as a spin 1/2 system. We detect the spin state by collecting state-dependent fluorescence. We apply the capability of the vacuum measurement to study the JCM dynamics. During the JCM dynamics, the Gaussian peak of the initial coherent state bifurcates and rotates around the origin of phase space. They merge at the so-called revival time at the other side of phase space. We reconstruct the density matrix directly from the Q function with the least square method and obtain the corresponding Wigner function, where we observe the emergence of non-classical state by the negativity. Further more, We simulate the QRM in all coupling regimes by means of detuned bichromatic sideband excitations. The controllability of the demonstrated quantum simulator enables us to experimentally explore the QRM in detail, including a wide range of otherwise unaccessible phenomena, such as those happening in the ultrastrong $(g/\omega_m > 0.1)$ and deep strong $(g/\omega_m > 1)$ coupling regimes. In this project, we adiabatically generate the ground state of the QRM in the deep strong coupling regime, where we detect the nontrivial entanglement between the bosonic field mode and the two-level system. Moreover, we experimentally observe the breakdown of the rotating-wave approximation when the coupling strength is increased, and the generation of phonon wave packets that bounce back and forth when the coupling strength reaches the deep strong coupling regime.

Key words: Trapped ion; Quantum optics; Jaynes-Cummings model; Quantum Rabi

model; Vacuum measurement; Adiabatic

目　录

个人简历、在学期间发表的学术论文与研究成果 ……………………………… 105

插图索引

主要符号对照表

Amp	Amplifier
AOM	Acousto Optic Modulators
AWG	Arbitrary Waveform Generator
BSB	Blue sideband
BS	Beam splitter
CCD	Charge-coupled device
DSC	Deep strong coupling
EOM	Electro-optic modulator
FP	Fabry-Pérot
FPGA	Field programmable gate array
HR	Helical resonator
JCM	Jaynes-Cummings model
LO	Local oscillator
PD	Photodiode
PBS	Polarizing beam splitters
PMT	Photomultiplier tube
QRM	Quantum Rabi model
RF	Radio frequency
RWA	Rotate wave approximation
RSB	Red sideband
USC	Ultra-strong coupling

第1章 Introduction

1.1 Quantum optics with trapped ions

The interaction between the electromagnetic field and matter in atomic system, is arguably one of the most fundamental physical processes. In recent decades, the study of light-matter interaction has achieved a variety of technological applications and novel scientific results. Indeed, the modern research field of quantum optics is based on the quantum theories of quantum coherence proposaled by Glauber [1]. Since then, the ability and interest to pursue controllable quantum systems have been growing dramatically, until reaching the accuracy needed to manipulate light-matter interactions at the single-photon or single atom level. This remarkable achievement was made possible via the confinement of atoms through the trapped ion system or confinement of the light in the cavity quantum electrodynamics (cavity QED) system. In this context, the concept of light-matter interaction has extended its meaning to that stated as the interaction between bosonic fields (light) and a two-level system (matter), which come up with the two famous model quantum Rabi model[2] and Jaynes- Cummings model[3]. The Jaynes-Cummings model is naturally derived from the quantum Rabi model after the rotating wave approximation when the coupling strength is much smaller compared to that of the mode frequency.In fact, the ability to control such interactions was demonstrated in the seminal works of Serge Haroche and David Wineland. In Serge Haroche's seminal work, a stream of atoms controls the field in a microwave cavity[4]. In David Wineland's work, the interaction between vibrations of the harmonic oscillator and electronic internal states of atoms (ions) in a harmonic trap is precisely controlled by means of optical lasers [5]. Both of them have won the Nobel prize in 2012 due to their amazing works.

Here, we particularly focus on the trapped system. In a trapped ion system, the nature optical or hyperfine states of the ion serve as the qubit, while the bosonic mode is given by the harmonic oscillations inside the trap. To be more specific, we use the two of the hyperfine states of $^{171}Yb^+$ as the internal electric state. The motional mode is cooled down to its ground state via Raman sideband cooling [6]. The interaction between internal electronic states and the external motion degree of freedom can be controlled by Raman laser drivings with precise and full control of intensity and pulse duration. Measurement of the internal electronic state is done via state-dependent fluorescence techniques, while

other observables such as bosonic mode population can be obtained in an indirect way, mapping the expected value to internal state transitions.

The trapped ions system are well known for the high fidelity achieved in state preparation, read-out, and control with the development of laser technology and optical detection (high N.A lens) techniques. Single-qubit gates can be implemented by addressing electronic transitions with laser drivings, while two-photon C-NOT gates[7] are realized using the motional degrees of freedom as a quantum bus to mediate interactions between distant ions. These features enable trapped ions as a promising platform not only for quantum computation but also for the implementation of quantum simulations [8–10].

Of specific interest for the present thesis is the possibility of using a single trapped ion to study the Jaynes Cummings model in the phase space via Q function and simulation of the quantum Rabi model in the regime where coupling strength is comparable or even larger compare to the bosonic mode frequency.

1.2 Quantum harmonic oscillator in phase space

In this section, I will introduce the quantum harmonic oscillator (treated as phonon), which is the essential part as the motional degree of freedom in trapped ion system, then I will talk about some important operators that are closely related to the harmonic oscillator. I will introduce the Husimi Q function and Wigner function, which equivalent to the density matrix to describe a state in phase space.

1.2.1 Quantum harmonic oscillator

The total the total of a particle with mass m and velocity v in a harmonic potential $V = \frac{m}{2}\omega^2\hat{x}^2$ has the form as

$$\hat{H} = \frac{\hat{p}^2}{2m} + \frac{m}{2}\omega^2\hat{x}^2. \tag{1-1}$$

Here $\hat{x}$ and $\hat{p}$ are the position operator and momentum operator, respectively. We resort to the annihilation operator $\hat{a}$ and creation operator $\hat{a}^\dagger$ defined as

$$\hat{a} = \sqrt{\frac{m\omega}{2\hbar}}(\hat{x} + i\frac{1}{m\omega}\hat{p}),$$
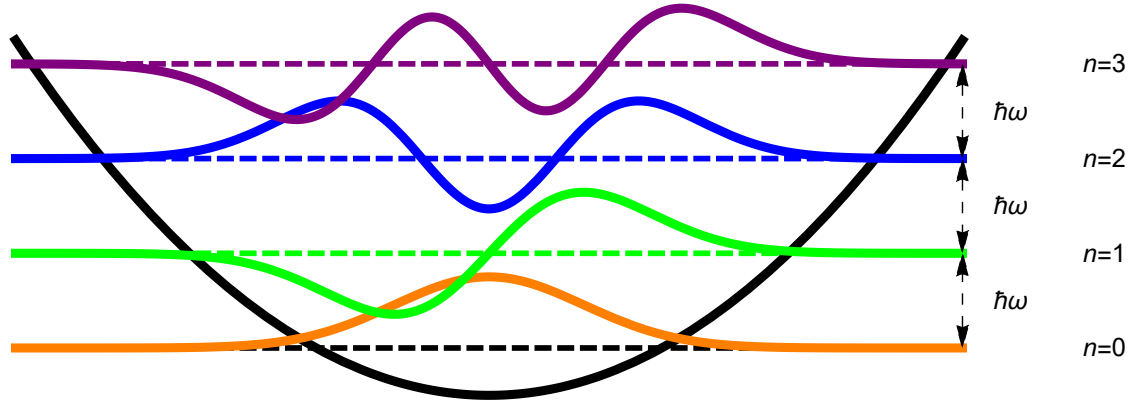
图 1.1 Quantum harmonic oscillator and its wave-function.

$$\hat{a}^{\dagger} = \sqrt{\frac{m\omega}{2\hbar}}(\hat{x} - i\frac{1}{m\omega}\hat{p}). \tag{1-2}$$

We solve these equations. 1-2 and obtain

$$\hat{x} = \sqrt{\frac{\hbar}{2m\omega}}(\hat{a}^{\dagger} + \hat{a}),$$

$$\hat{p} = i\sqrt{\frac{\hbar m\omega}{2}}(\hat{a}^{\dagger} - \hat{a}). \tag{1-3}$$

It is straightforward to rewritten the total Hamiltonian as

$$\hat{H} = \hbar\omega(\hat{N} + \frac{1}{2}), \tag{1-4}$$

where we define $\hat{N} = \hat{a}^{\dagger}\hat{a}$ as the number operator. Using the commutator relation $[\hat{x}, \hat{p}] = i\hbar$, and without going into many mathematical details, we list the form of its energy eigenfunctions and eigenvalues as

$$\begin{aligned}
\Psi_n(x) &= \frac{1}{\sqrt{2^n n!}} \cdot (\frac{m\omega}{\pi\hbar})^{1/4} \cdot exp(-\frac{m\omega x^2}{2\hbar})H_n(\sqrt{\frac{m\omega}{\hbar}}x), \\
E_n &= \hbar\omega(\hat{N} + \frac{1}{2}),
\end{aligned} \tag{1-5}$$

where $H_n(x)$ are the Hermite polynomials. We plot the first several energy levels and its corresponding wave-functions in Fig. 1.1. We clearly observe that the wave-function of odd n and even n belong to the different parities.

1.2.2 Displacement operator and squeeze operator

Any operator in the quantum phase space could be constructed from the basic two operators $\hat{a}$ and $\hat{a}^\dagger$. Considering a one-dimensional harmonic oscillator, the basic two operators are displacement operator and the squeeze operator. I will first talk about displacement operator and then move to the squeeze operator.

The displacement operator is defined as

$$\hat{D}(\lambda) = e^{\lambda \hat{a}^\dagger - \lambda^* \hat{a}}, \tag{1-6}$$

where $\lambda = |\lambda|e^{i\phi}$ is a complex number. It is easy to prove that the displacement operator is an unitary operator, which satisfies $\hat{D}^\dagger \hat{D} = \hat{1}$. In this context, if we define $\hat{A} = \lambda \hat{a}^\dagger$ and $\hat{B} = \lambda^* \hat{a}$, we calculate the commutator of $\hat{A}$ and $\hat{B}$,

$$
\begin{aligned}
[\hat{A}, \hat{B}] &= [\lambda \hat{a}^\dagger, \lambda^* \hat{a}] \\
&= \lambda \lambda^* [\hat{a}^\dagger, \hat{a}] \\
&= -|\lambda|^2.
\end{aligned}
\tag{1-7}
$$

We have the relations $[A, [A, B]] = [B, [A, B]] = 0$, then we can use the Baker-Hausdorff theorem, and immediately get the displacement operator in the following form

$$\hat{D}(\lambda) = e^{-\frac{\lambda^2}{2}} e^{\lambda \hat{a}^\dagger} e^{\lambda^* \hat{a}}. \tag{1-8}$$

Without further mathematical calculation, I list the main two properties
1. $\hat{D}^\dagger(\lambda) = \hat{D}^{-1}(\lambda) = \hat{D}(-\lambda)$
2. $\hat{D}(\lambda_1)\hat{D}(\lambda_2) = \hat{D}(\lambda_1 + \lambda_2)e^{iIm(\lambda_1 \lambda_2^*)}$

With the displacement operator, we can naturally generate the coherent state $|\alpha\rangle$ by displacing the vacuum state $|0\rangle$, which we shows in Fig. 1.2(a). The coherent state $|\alpha\rangle$ can further expanded in the Fock state basis as

$$|\alpha\rangle = e^{-\frac{\lambda^2}{2}} \sum_{i=0}^{+\infty} \frac{\alpha^n}{\sqrt{n!}} |n\rangle \tag{1-9}$$

Subsequently, we can calculate the probability distribution of the phonons in a coherent
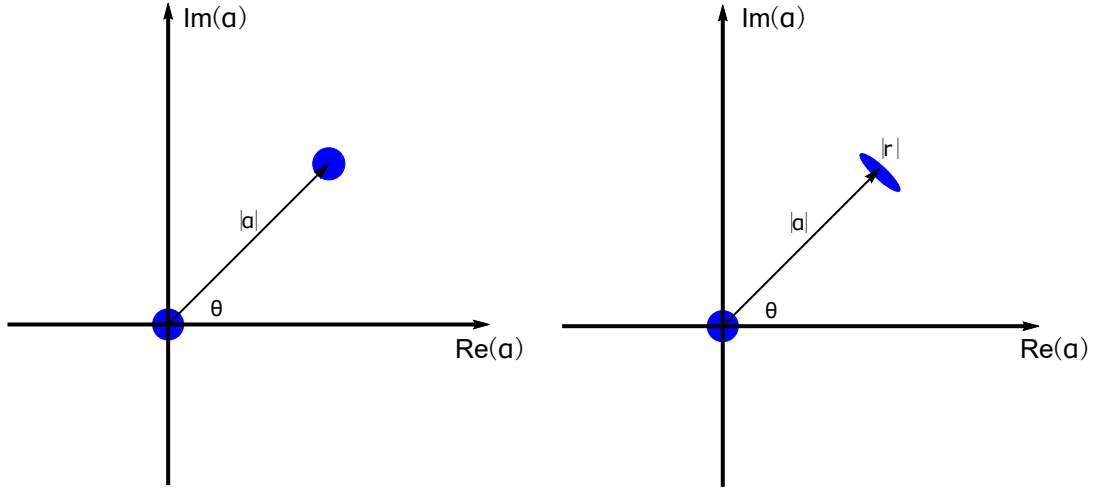
图 1.2　Displacement and squeezing-displacement of the vacuum state $|0\rangle$ in phase space.

state, given by

$$
\begin{aligned}
p(n) &= |\langle n|\alpha\rangle|^2 \\
&= \frac{|\alpha|^{2n}\mathrm{e}^{-|\alpha|^2}}{n!} \\
&= \frac{|\langle n\rangle|^n\mathrm{e}^{-|\alpha|^2}}{n!}.
\end{aligned}
\tag{1-10}
$$

Here $\langle n\rangle$ is the average phonon of the system, and thus the coherent state distribution follows Poisson distribution.

The squeeze operator is defined as

$$
\hat{S}(\zeta) = \mathrm{e}^{-\frac{1}{2}(\zeta\hat{a}^{\dagger 2}-\zeta^*\hat{a}^2)},
\tag{1-11}
$$

where $\zeta = |r|\mathrm{e}^{i\theta}$. $\hat{S}$ is a unitary operator and therefore obeys $\hat{S}(\zeta)\hat{S}^{\dagger}(\zeta) = \hat{S}^{\dagger}(\zeta)\hat{S}(\zeta) = \hat{1}$. The squeeze operator is widely used in quantum optics and can operate on any state. For instance, when acting on the vacuum state $|0\rangle$, the squeezing operator produces the squeezed vacuum state $|\zeta\rangle$. The squeezing operator can also act on coherent states $|\alpha\rangle$ and produce squeezed coherent states $|\zeta, \alpha\rangle$ shown in Fig. 1.2(b). We note that the squeezing operator is not commutate with the displacement operator. The squeezed vacuum state $|\zeta\rangle$, which is squeezed vacuum $|0\rangle$ in one direction, while stretched in the other direction. The ratio between this two direction is determined by the $|r|$. As seen from the Hamiltonian, the Squeeze operator involves two phonons creation or annihilation, which does not change

the state's parity. For the squeezed vacuum state, here we list the phonon distributions as

$$
\begin{aligned}
p_{2n} &= |\langle 2n|\zeta\rangle|^2 \\
&= \frac{(2n)!}{2^{2n}(n!)^2}\frac{\tanh^{2n} r}{\cosh r}, \\
p_{2n+1} &= 0.
\end{aligned}
\tag{1-12}
$$

1.2.3 The Husimi-Q function

In the quantum optics, to describe a state, their are mainly three functions, which are equivalent to the density matrix, namely the P function, the Husimi Q function and Wigner function W. All of them actually are the Fourier transforms of characteristic functions, linked to the quantum average of the displacement operator as mentioned above, in a state described by the density matrix ρ[11,12]. Here for the sake of this these, we focus on the Husimi Q function and Wigner function.

When operators appear as arguments of a function, we must take their ordering into consideration. Here we consider the two cases of characteristic function based on the different order of $\hat{a}$ and $\hat{a}^\dagger$, where on the anti-normal order the $\hat{a}$ always on the left and the symmetric order with all products of operators are symmetry

$$
\begin{aligned}
C^{\rho}_{an}(\lambda) &= \mathrm{Tr}[\rho e^{-\lambda^*\hat{a}}e^{\lambda\hat{a}^\dagger}], \\
C^{\rho}_{s}(\lambda) &= \langle \hat{D}^\dagger(\lambda)\rangle = \mathrm{Tr}[\rho e^{\lambda\hat{a}^\dagger-\lambda^*\hat{a}}]
\end{aligned}
\tag{1-13}
$$

The corresponding Q function and Wigner W function are two dimensional Fourier transforms of these two characteristic functions, respectively. I will first talk about the Q function and then move to the Wigner function W.

The Q function is the Fourier transform of the anti-normal-order characteristic function with the formula

$$
Q^{\rho}(\alpha) = \frac{1}{\pi^2}\int d^2\lambda e^{\alpha\lambda^*-\alpha^*\lambda}C^{\rho}_{an}(\lambda).
\tag{1-14}
$$

With the help of the close relationship

$$
\frac{1}{\pi}\int d^2\beta = \hat{1},
\tag{1-15}
$$

and two-dimensional Dirac δ function

$$\delta(\lambda) = \frac{1}{\pi} \int d^2\alpha \, e^{\alpha\lambda^* - \alpha^*\lambda}. \tag{1-16}$$

We derive it to a simplified version of Q function

$$Q(\alpha) = \frac{1}{\pi} \langle \alpha | \rho | \alpha \rangle. \tag{1-17}$$

This Eq. (1-17) can be further extended to the following form

$$Q(\alpha) = \frac{1}{\pi} \langle 0 | \hat{D}(-\alpha) \rho \hat{D}(\alpha) | 0 \rangle. \tag{1-18}$$

In this case, the Q function is equal to the vacuum component in the field displaced by
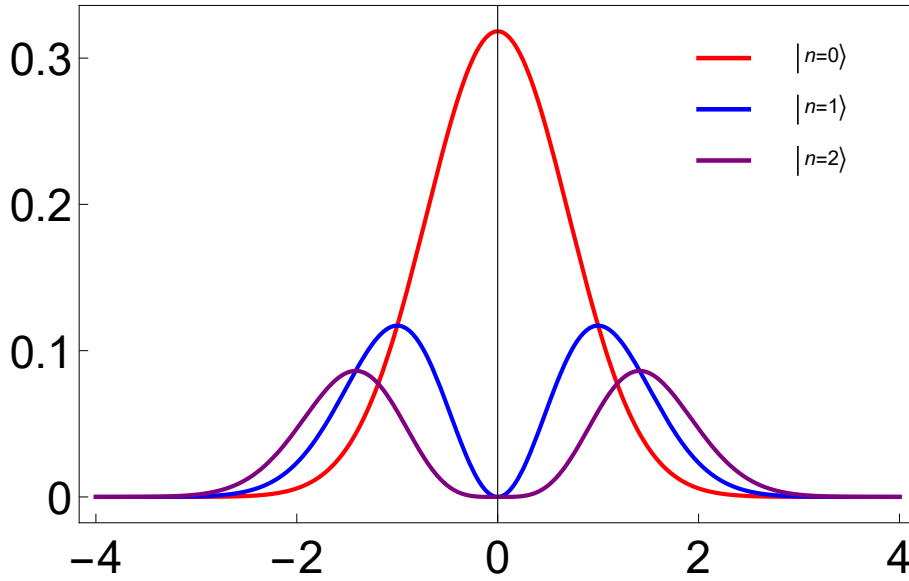
图 1.3　The Q function of the Fock states $|n = 0, 1, 2\rangle$.

$-\alpha$ in phase space. For this vacuum measurement method, we will discuss in detail in Chapter 4. As a simple example, we plot the Q function for the Fock states $|n = 0, 1, 2\rangle$, respectively, as shown in Fig. 1.3, and we clearly see the lower bound of Q function is zero, while the upper bound is $\frac{1}{\pi}$. The Q function is suitable to observe dynamic evolution in phase space, and we extend this study in Chapter 4. However, as for the non-classical feature, a Wigner function is much helpful due to its sensitivity to the interference, which I will talk in the following part.

1.2.4 The Wigner function

The W function is the Fourier transform of the system-order characteristic function with formula

$$W^\rho(\alpha) = \frac{1}{\pi^2} \int d^2\lambda e^{\alpha\lambda^* - \alpha^*\lambda} C_s^\rho(\lambda). \tag{1-19}$$

Omitting the relative complicated calculation, we directly give another equivalent expression (which used frequently in the experiments to construct the Wigner function)

$$W(\alpha) = \frac{2}{\pi} \text{Tr}[\hat{D}(-\alpha)\rho\hat{D}(\alpha)\hat{P}]. \tag{1-20}$$

The Wigner function is proportional to the expectation value of $\hat{P}$ in the state obtained by displacing the state in phase space by the amount by $-\alpha$. Here the $\hat{P}$ is the phonon parity operator with eigenvalues ± 1, so the Wigner function is bounded between $\frac{-2}{\pi}$ and $\frac{2}{\pi}$. We particularly point out, the negativity of the Wigner function, demonstrates it is a non-classical state. Here, to give an impression, we plot the results of Wigner function for the Fock states $|n = 0, 1, 2\rangle$ respectively shown in Fig. 1.4. We see the negativity in the Fock states $|n = 1\rangle$ and $|n = 2\rangle$, and their difference is quite obvious.
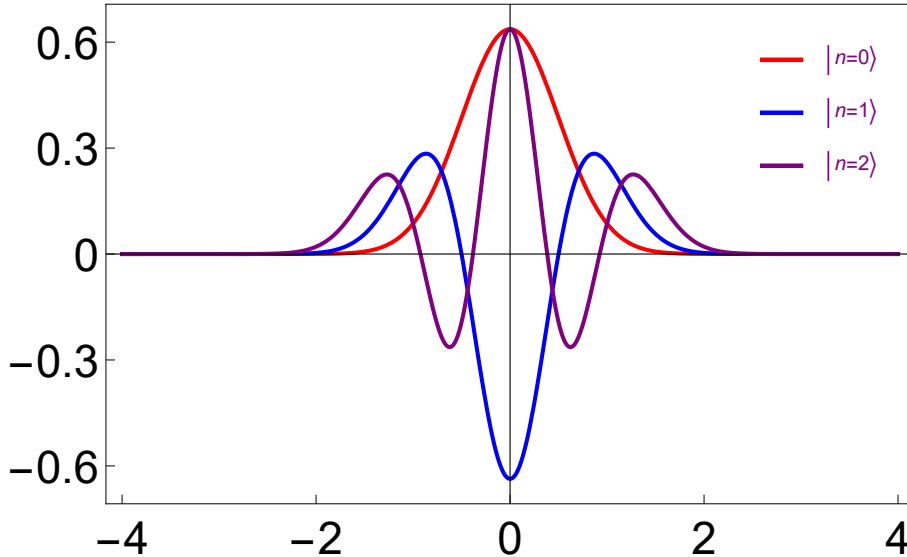
图 1.4　The Wigner function of the Fock states $|n = 0, 1, 2\rangle$.

1.3 Thesis organization

The thesis is organized as follows.

Chapter 2: I will first introduce the basic principle of an ion trap, then I will focus on the Ytterbium ion, where I will discuss the ionization, cooling, optical pumping and state-dependent fluorescence detection of the trapped ion. I will show the experimental setup relates to diode lasers in this chapter.

Chapter 3: I will introduce the basic ion-laser interaction. Firstly, I will begin with a simple two-level system atom-laser interaction. Then I will move to the three-level Λ-type atom-laser interaction, where I will resort to the effective Hamiltonian theory to derive the basic Hamiltonian. Then I will discuss the experimental part, where we engineer the Hamiltonian with Raman laser system. In this experimental part, I focus on the laser configuration, the optimization of our system, the control system, and the general experimental procedures. I will show some experimental results that we observed. Finally, I will discuss two imperfections of our motional degree of freedom, the motional heating rate and dephasing that relate to the motional coherence time.

Chapter 4: I will present the study of the Jaynes-Cummings model. During the JCM dynamics, we observe the Gaussian peak of the initial coherent state bifurcates and rotates around the origin of phase space. They merge at the so-called revival time at the other side of phase space. We reconstruct the density matrix directly from the Q function with the least square method and obtain the corresponding Wigner function, where we observe the non-classical state emergence by the negativity.

Chapter 5: I will present the simulation of quantum Rabi model, where we access deep strong coupling regime and have adiabatically prepared its ground state in this regime. For the ground state, we observe the property of parity conservation and entanglement.

Chapter 6: The summary and outlook.

第2章　Ytterbium ion

In this chapter, I briefly talk about the principle of the Paul trap, then move to the ^{171}Yb$^+$ ion part. In the ^{171}Yb$^+$ ion part, I talk about the hyperfine clock state, which is mathematically equivalent to a pseudo spin $1/2$ system. After that, I will discuss the loading of ^{171}Yb$^+$, and diode lasers that needed to cool, repump, initialize and detect the internal states of an ion.

2.1　The Paul trap

It was proved by Earnshaw's theorem that a charge acted on by electrostatic forces cannot rest in stable equilibrium in an electrical field. Thus, it is impossible to confine an ion using only an electric static field. This theorem is based on the fact that an electric field has no divergence in a region without any free charge density distribution, $\vec{\nabla}.\vec{E} = 0$. Zero divergence means there are no sources or sinks in that region of interest, and all the field lines come in must come out. Similarly, the Gauss' theorem also shows that the integral of the normal component of the $\vec{E}$ over the boundary surface equals the volume of the $\vec{\nabla}.\vec{E}$, which is zero

$$\oint \vec{E}.d\mathbf{S} = \int \int \int \vec{\nabla}.\vec{E} d^3 r = 0. \tag{2-1}$$

In order to get the zero value, the $\vec{E}.d\mathbf{S}$ should have different signs over all the surface. Where $\vec{E}.d\mathbf{S} < 0$, the electric field lines point inward and a positively charged ion will feel the force to push it back to the volume, while for the surface where $\vec{E}.d\mathbf{S} > 0$, the ion escapes along that direction. The argument means that not all the field lines are directed inward for a positive charged ion. Thus any deviation from the equilibrium position will accelerate the ion away. That position can be described as a saddle point of the electrostatic potential.

In the work of the trapped ion system, we apply either an oscillating electric (AC) field (Paul traps[13,14]) or a static magnetic field (Penning traps[15]) together with static electric field to create an effective time-averaged potential to confine the ion. In our work, we use a radio-frequency (RF) Paul trap for the experiments.

2.1.1 Principle of ion trap

As shown in Fig. 2.1, the four rods lie parallel to the z-axis and at the square corner is the xy-plane. The two opposite electrodes are connected to each other. The rods of the blue pair are applied the RF signal with $V = V_0 \cos(\Omega_{rf}t)$, while the rods of black pair are connected to the ground. The distance between the two pairs is $2r_0$, which is much larger than the distance between two needles. The potential of the varying field satisfies the Laplace equation $\nabla^2\phi = 0$ (note $\vec{\nabla}.\vec{E} = 0$ and $\vec{E} = -\nabla$), thus, we can reasonably assume the potential that close to the z axis($z = 0$) has the general form (with the symmetry voltage in the electrodes considered)
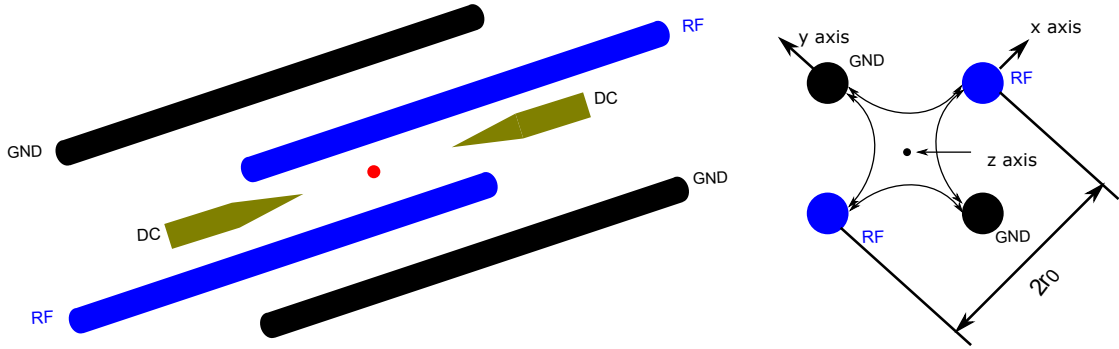
图 2.1 Schematic of four-rod trap. The two blue rods are the RF electric connect with a varying field $V = V_0 \cos(\Omega_{rf}t)$, while two black rods are grounded, the z axis is along the needle direction, where DC voltage is connected, the xy-plane is clearly shown as in the side view. The z axis is parallel to the needle direction. The distance between the pairs of electric rod and needle are $2r_0$ and $2d_0$, respectively.

$$\phi = a_0 + a_2(x^2 - y^2). \tag{2-2}$$

The coefficients are determined by the boundary conditions

$$\phi = \phi_0 + \frac{V_0}{2}\cos(\Omega_{rf}t), x = \pm r_0, y = 0, \tag{2-3}$$

$$\phi = \phi_0 - \frac{V_0}{2}\cos(\Omega_{rf}t), y = \pm r_0, x = 0. \tag{2-4}$$

Thus, the potential can be simplified to

$$\phi = \phi_0 + \frac{V_0}{r_0^2}\cos(\Omega_{rf}t)(x^2 - y^2). \tag{2-5}$$

This potential has a saddle point in the xy-plane in the middle of the electrodes, a potential hill in one direction and a valley in the other direction. From the gradient of the potential, we have the electric field

$$
\begin{aligned}
\vec{E} &= E_0(\vec{r}) \cos(\Omega_{\mathrm{rf}} t) \\
&= -\frac{V_0}{r_0^2} \cos(\Omega_{\mathrm{rf}} t)(x \hat{e}_{\mathrm{x}} - y \hat{e}_{\mathrm{y}}).
\end{aligned}
\tag{2-6}
$$

In the following part, we focus on only x-direction(it is symmetric with y-direction). The equation for the x-direction is described as

$$
m \frac{d^2 x}{d^2 t} = -\frac{eV_0}{r_0^2} \cos(\Omega_{\mathrm{rf}} t) x.
\tag{2-7}
$$

By changing the variable $\tau = \frac{\Omega_{\mathrm{rf}} t}{2}$, we derive the equation as

$$
\frac{d^2 x}{d^2 \tau} = -\frac{4eV_0}{m \Omega_{\mathrm{rf}}^2 r_0^2} \cos(2\tau) x.
\tag{2-8}
$$

Eq. (2-8) is a simplified version of the Mathieu equation

$$
\frac{d^2 x}{d^2 \tau} + (a_{\mathrm{x}} - 2q_{\mathrm{x}} \cos(2\tau)) x = 0,
\tag{2-9}
$$

with $a_{\mathrm{x}} = 0$. Here, we define the parameters that in front of the oscillating term $\cos(2\tau)$ as $2q_{\mathrm{x}}$ follow the convention. The q_{x} has the form

$$
q_{\mathrm{x}} = \frac{2eV_0}{\Omega_{\mathrm{rf}}^2 m r_0^2}.
\tag{2-10}
$$

Here, I omit many mathematical details and directly list the solution of this Mathieu equation as

$$
x = x_0 \cos(\frac{q_{\mathrm{x}} \tau}{\sqrt{2}})(1 + \frac{q_{\mathrm{x}}}{2} \cos(2\tau)).
\tag{2-11}
$$

Here, the q_{x} and a_{x} are usually less than 1 to validate the solution. From the Eq.(2-10), we notice that the motion part of the ion is composed by two parts. One part describes

the oscillation with angular frequency $\omega_x = q_x\tau/(\sqrt{2}t) = \frac{q_x\Omega_{rf}}{2\sqrt{2}}$ and amplitude x_0, another part describes the motion with angular frequency $\omega_{micro} = 2\tau/t$ and amplitude $x_0\frac{q_x}{2}$. Remember that $q_x \ll 1$, the motion can be understood as harmonic oscillation together with a small fast oscillation at the drive frequency Ω_{rf}. This fast oscillation part is the micromotion. We insert the q_x into ω_x and consider the symmetry situation of the y-axis, then we get the corresponding angular frequency as

$$\omega_x = \omega_y = \frac{q_x\Omega_{rf}}{2\sqrt{2}} = \frac{eV_0}{\sqrt{2}m\Omega_{rf}r_0^2}. \tag{2-12}$$

This $\omega_{x,y}$ is also called the secular frequency. Note that in this thesis the trap frequency or radial trap frequency basically means angular frequency. Since I will use frequency or angular frequency here and there in this thesis, I make s statement here. If I do not give the exact value, each understand as frequency or angular frequency will not influence our understanding of the thesis, while if I give the value, as long as we have a bracket with 2π in front of the value, it represents a angular frequency, other situation, we can understand as frequency. In the above discussion, we ignore the small RF leakage in the z-direction due to the endcaps. This leakage drives the motion along the z direction to be approximated as a harmonic oscillator with secular frequency ω_z, which is much less than the $\omega_{x,y}$. So far, for all the experiments present in this thesis, we only deal with the corresponding $x - y$ motional mode $\omega_{x,y}$.

Note that the micromotion could heavily reduce the ion's lifetime. Therefore, before doing any experiment, we usually minimize the micromotion effects. I will discuss this part in detail in Chapter 3.

2.1.2　The helical resonator

In the trapped ion experiment, the high-speed manipulation of the external phonon degree of freedom and the internal electric state freedom requires high secular frequency. In our trapped ion system, since the Raman laser configuration perpendicular to the z axis, which limits our coupling between the laser and ion in the radial mode that is $\omega_{x,y}$ (We also call it radial trap frequency). Generally, we run the experiments with radial trap frequency around (2π) 2.5 MHz. Note here if it reprensent the angular frequency, I will put a 2π in a braket in front of the frequency value, otherwise it represent the frequency.

The oscillating field V_0 is large enough (V_0 more than 500 V) to reach a high trap

frequency. However, the commercial RF source cannot reach such high voltage even after the amplification, and the reflection signal may destroy the amplifier. To amplify the voltage, we employ the helical resonator[16], which shown as in Fig. 2.2. In this configuration, the voltage on the trap electrodes is given by $V_0 = \varepsilon\sqrt{P*Q}$, where ε is determined by the geometry of the helical resonator, P is the input power of RF and Q is the quality factor of the resonator. Our helical resonator has a resonance frequency of 25.8 MHz, $Q = 200$. At driven power $P = 3W$, the radial trap frequency reach around $(2\pi)3$ MHz as shown in Fig. 2.2.

Here, we measure the trap frequency by applying another external modulation RF source. When we have a single ion in the trap, we apply the external modulation field and scan the modulation frequency. When the modulation frequency equals to the trap frequency, we actually displace the ion in the phase space. From the charge-coupled device (CCD), we clearly observe the stretch of the ion, this demonstrates that resonance frequency is the trap frequency. When the trap power is larger, it confines the ion more tightly, we need to increase the modulation amplitude accordingly to see the displacement. The relationship between the radial trap frequency and its drive power is shown in Fig. 2.2, which follows the square root relation. We particularly point out that we remove the low pass filter ($\sim$ kHz) for this part of experiments, in this case, the modulation RF source can pass the circuit and enter into the blades of our trap. One of the advantages of this trap frequency measurement is that it gives us the sense of the relationship between the trap frequency and its drive power, which benefits us a lot to distinguish the sidebands of Raman spectroscopy.

图 2.2　Schematic of helical resonator to show the inductive coupling between the RF input antenna and the trap electrodes.
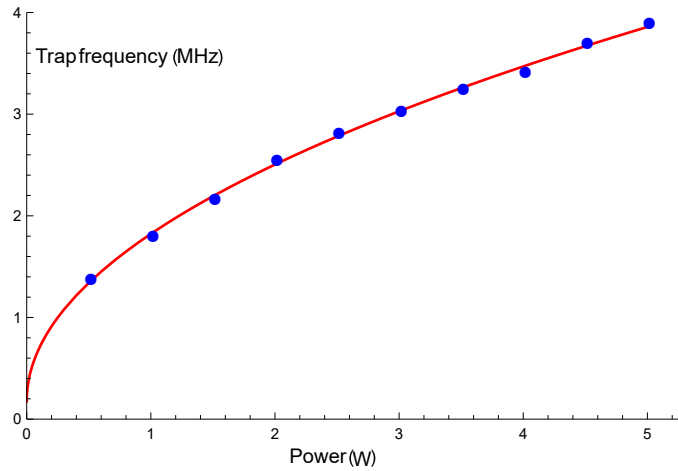
图 2.3　Relationship between the radial trap frequency and its drive power.

2.2　Trapping ^{171}Yb$^+$

2.2.1　Loading ^{174}Yb$^+$

During the Ph.D. carrier, I have worked in two different types of Paul trap, one is the four rods trap, the other one is the five segments blade trap. Here, I focus on the blade trap, which I have spent most of my effort. The blade trap is shown in Fig. 2.4. We particularly point out here for the sake of avoiding unwanted scattering, we design as shown in the geometry structure that the vertical distance between two blades is about 450 μm, which is smaller than that of the horizontal distance (550 μm). We carefully assemble the trap and put it into the chamber, bake the whole system about two weeks in the temperature around 200°C. If everything works smoothly, the chamber can reach the ultra-high vacuum less than 10^{-10} Torr, which is suitable for the future experiments. More details about the vacuum part should go to the my colleague's thesis[17]. Once we verify the chamber's vacuum, our work shift to the installation of the helical resonator, the connection of DC voltage to the segments of the blade, the alignment of the diode laser system, and the installation of image and photomultiplier tube (PMT) system.

The installation of helical resonator system

The installation of the helical resonator is a great work requires lots of experience. According to the reference[18], we design the parameters (structure) of the helical resonator, while to achieve higher Q factor, we test the helical resonator by trial and error and iterate several times to get proper parameters. Note that we must clean the copper before assembling. The diameter of the copper tube and coil is 10 cm, and 5 cm, respectively.
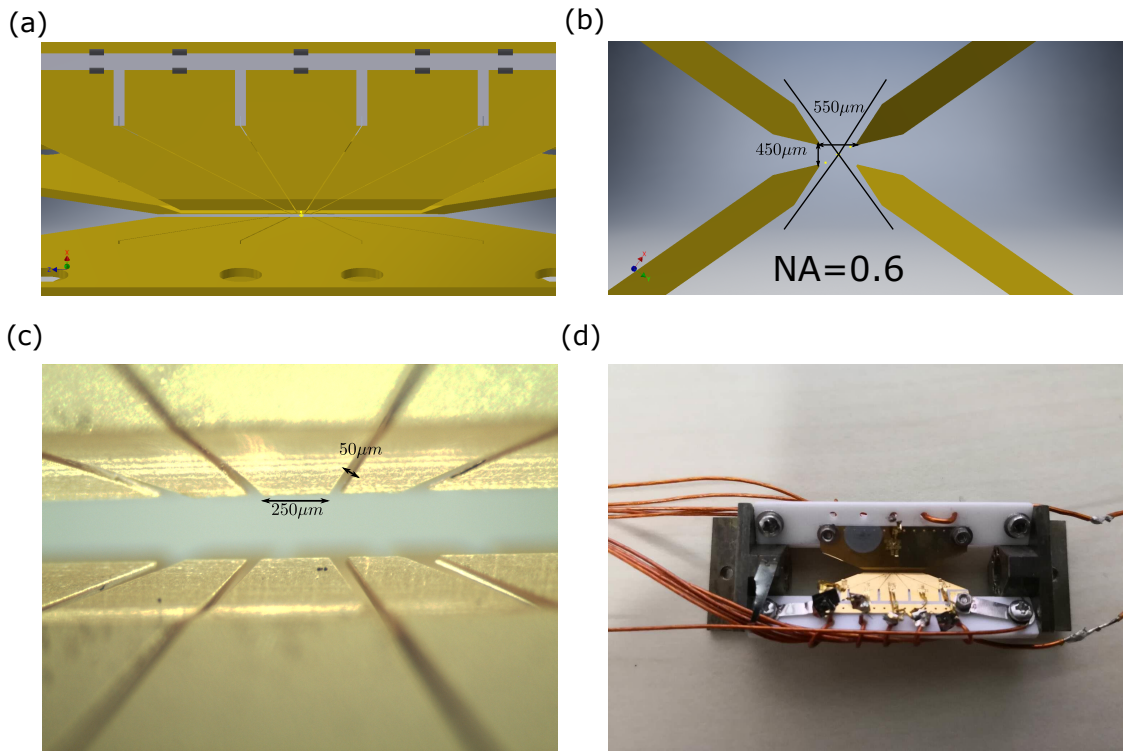
图 2.4 The five segments blade trap. Panel (a) shows the Inventor design of the blade trap. Here we show the basic sizes of our blade trap. Panel (b) shows the side view of the blade trap is a rectangle, with width 550 μm height 450 μm. This design is to to reduce the scattering from the blade.We use the high N.A=0.6 lens to collect the photons emitted by the ion. Panel (c) shows the specific parameter of the blade. The width of each segment in the DC blade is about 250 μm, and the distance between each segment is design to be approximately 50 μm. Panel (d) is the assemble blade that present here now is for the teaching of new students to understand the structure properly.

The number of turns of the coils is around 8. The Q factor of the helical resonator can achieve 200 after optimization when we connect it to the trap at drive frequency around 25.8 MHz. For the blade trap, we have to employ the bifilar coil inside the helical resonator tube. Thus, we can apply an independent DC voltage in one of the RF blades. The trick thing is that we need to add a capacity with a certain value between the two coils before connecting to the RF blades. The capacity is around 1nF, which serves as shortcut operation in the high-frequency AC circuit. Thus, it guarantees the two coils are in phase.

Connection of DC voltages

The DC voltages connected to the blade segments are used to separate the two radial modes, compensate the micromotion and form the boundary condition of the trapped ion

along the axial (z) direction. The DC voltages are not directly connected to the blade. To suppress the AC noise, which may come from the DC voltage or the other AC noise in the environment that couples to the cable, we design this two Π structure DC low pass filter with cut frequency at kHz level. Under this situation, we greatly suppress the noise at the frequency (equal to the trap frequency) that may kick the ion's motion and thermalize it. We show the circuit design and real instruments in Fig. 2.5(c,d). In fact, we put a voltage divider as shown in Fig. 2.5(a,b) before the DC voltage going into the DC low pass filter, which only samples about 1/20 of the DC voltages input. We do this based on two reasons. One reason is that our trap only needs a very low voltage (several Volts), the other reason is that our DC voltage is not precise when its output is low. So we produce high voltage output, while only sample part of it to improve the precision. In this circuit, all the resistors are insensitive to the temperature change.
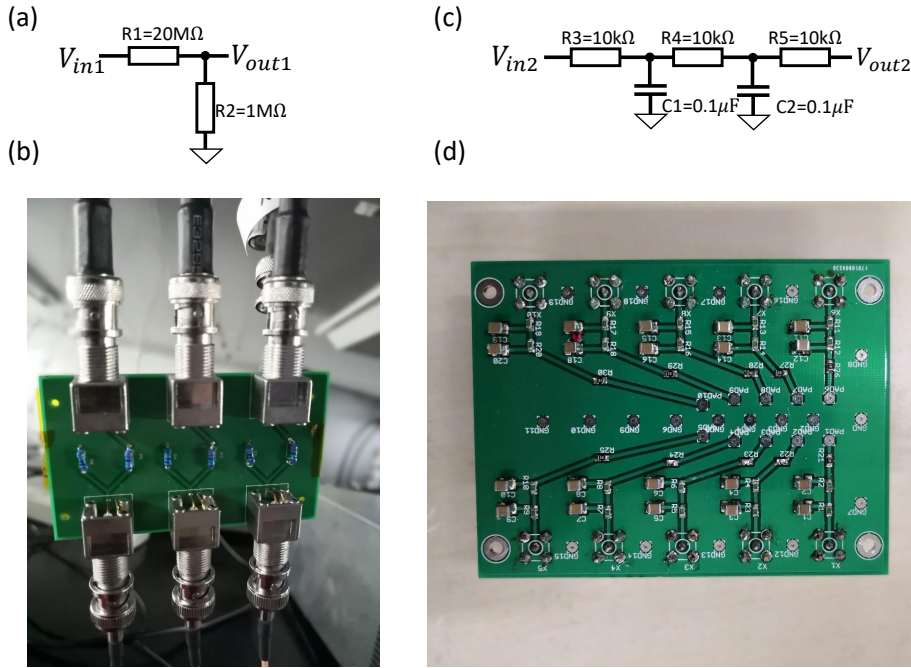
图 2.5　Voltage divider and low pass filter for the DC voltages. Panels(a,b) are the schematic and substantial of the voltage divider, we sample 1/20 of the input through this divider, and we increase our manipulation precision 20 times. Panels(c,d) are the schematic and substantial of 2 Π low pass filter structure.

2.2.1.1 The alignment of the diode laser system

For the trapped ion experiments, we mostly use the lasers to manipulate the states of the ion. The good thing for ^{171}Yb$^+$ is that we can buy the commercial lasers for all the relevant energy levels. In this way, we can save a lot of time, which can be used to do more important things for the experiment. Here, we show the optical path of the diode laser in Fig. 2.6. In the following several parts, I will explain it in detail.
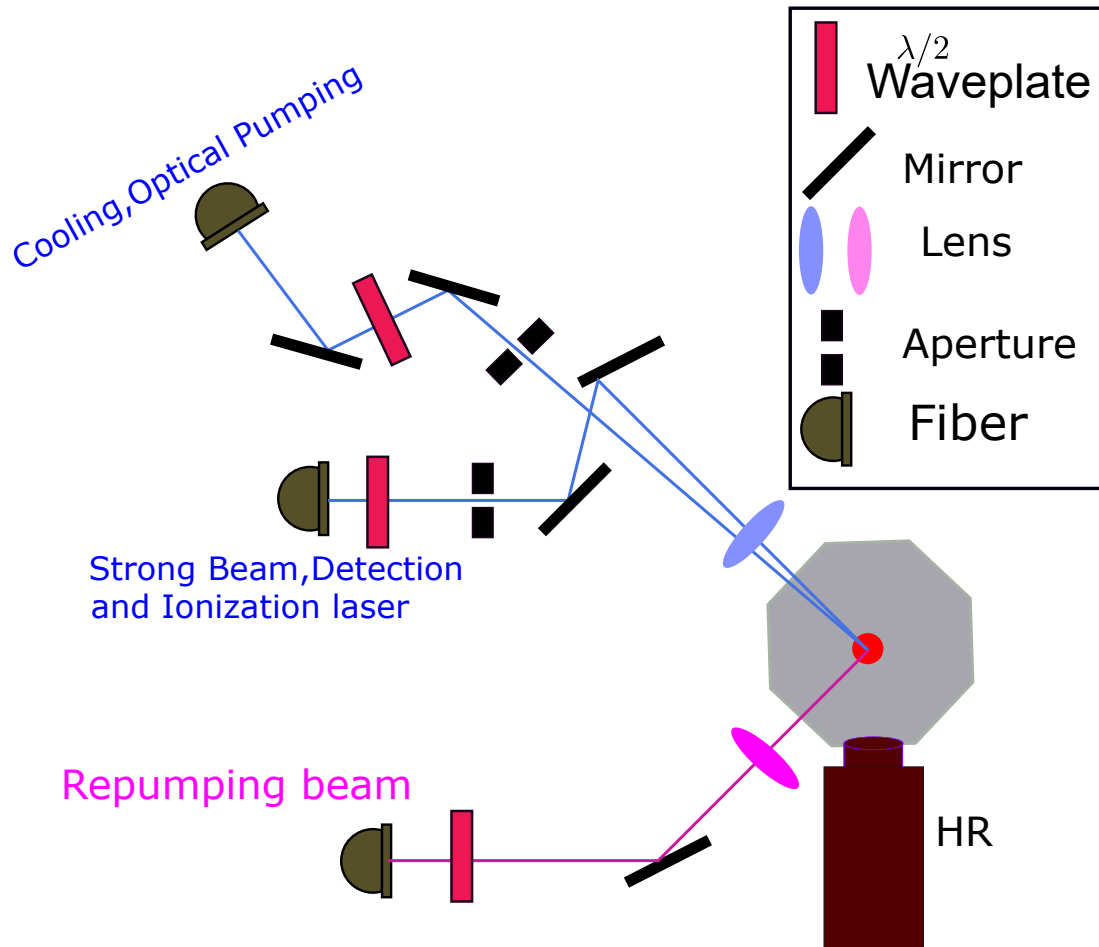
图 2.6 Overview of the diode-laser system with respect to the trap. The cooling beam and pumping beam come out from the polarization-maintain fiber, and strong beam, ionization beam(399 nm) beam and detection beam come out from another polarization-maintain fiber. The repumping beam(638 nmand 935 nm) beam come from another polarization-maintain fiber. All the beams are aligned to have 45 degree with respect to the z axis (parallel to the HR direction).

2.2.2　Trapping ^{171}Yb$^+$

When finishing all the above work, it is time to load the ion. Empirically, we try to load ^{174}Yb$^+$ first to double check the optical alignment. There are mainly two reasons. One reason is that the ^{174}Yb$^+$ has a zero nuclear spin and has no hyperfine structure in the electronic ground state which simplifies the lasers needed for the loading. For the other reason, the lack of hyperfine Zeeman sub-levels avoid the unwanted coherent population trapping in the dark states[19], and results in an increased fluorescence efficiency, which makes it sensitive to be detected through the PMT or CCD system. The loading stage is performed in two steps. Firstly, photoionization of the neutral atom, which emitted from the oven due to the high temperature that heated by the current. Once we have the ^{174}Yb$^+$, we also need to apply the cooling lasers and repumping lasers to detect the ion through the CCD or PMT. The photoionization is a two-photon process, which requires the laser with the wavelength about 398.9115 nm and the strong beam (with large power) around 369.5253 nm. These two beams are coupled to the same polarization (PM) fiber and then sent to the trap, and then go out together to the chamber as shown in Fig. 2.6, in this case, we guarantee whether they kick the ion or not simultaneously. Once we optimize the alignment of the strong beam (means we simultaneously optimize the 398.9115 nm laser), the next step is aligning the cooling beam. For this purpose, a convenient method is loading an ion crystal with the strong beam, and then we align the cooling beam with the block on and off the repumping beam at 935.1802 nm, which modulates with an electro-optical modulator (EOM) at frequency 3.0695 GHz. If the cooling beam hit the ion, we observe the count change, otherwise it stays same. By this way, it is not hard to find the cooling beam (usually the cooling beam is very close to the ion's position after the first round alignment by looking at the CCD scattering from the blade). Note that the repumping beam 935.1802 nm (935.1882 nm for the ^{171}Yb$^+$) should always keep on due to the leakage that $^2P_{1/2}$ has a probability of 0.5 % to decay to the metastable state $^2D_{3/2}$) for $^2D_{3/2}$ to $^2[3/2]_{1/2}$.

2.2.3　The energy schematic of ^{171}Yb$^+$

After finishing the alignment of the laser for the loading of ^{174}Yb$^+$, we finally move to the loading of ^{171}Yb$^+$. In this case, the wavelength of the photoionization are 398.9108 nm and 369.5263 nm. The main difference is that the hyperfine structure as shown in Fig. 2.7 requires the cooling beam to be modulated with a 14.7440 GHz sideband, which is
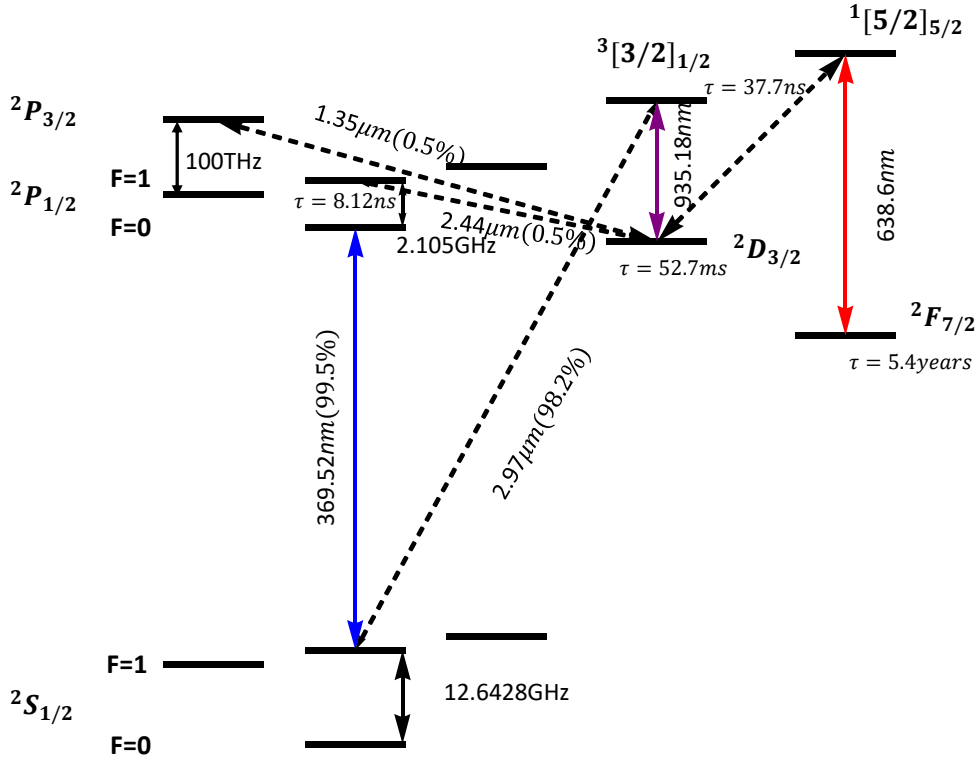
图 2.7　Schematic of ^{171}Yb$^+$ energy levels.

the second sideband of the 7.3720 GHz EOM. Recently, our group has bought the 14.7440 GHz EOM, which can have at most 10% efficiency.

2.2.4　Cooling and repumping

The initial kinetic energy of the ion after its capture following photoionization corresponds to a huge number of phonons, which must be suppressed before starting any quantum state manipulation. This is achieved by a combination of two procedures, called Doppler cooling and sideband cooling. In this section, I only talk about the Doppler cooling and leave the sideband cooling to Chapter 3.

The ^{171}Yb$^+$ ions are Doppler cooled on the relevant energies between $^2S_{1/2}$ and $^2P_{1/2}$, with a red detuned diode laser from the resonance by about 20 MHz. The cooling process works as follows, each time the ion absorbs a photon, it acquires a recoil momentum from the radiation field, where $\vec{k}$ is the momentum vector of the cooling light. When the ion moves opposite to the direction of beam propagation, the frequency of the light observed from the ion's rest frame is shifted to $\omega_1 + \frac{k}{c}$ due to the Doppler effect, it is closer to the atomic resonance, and the ion absorbs more photons. On the other hand, when the
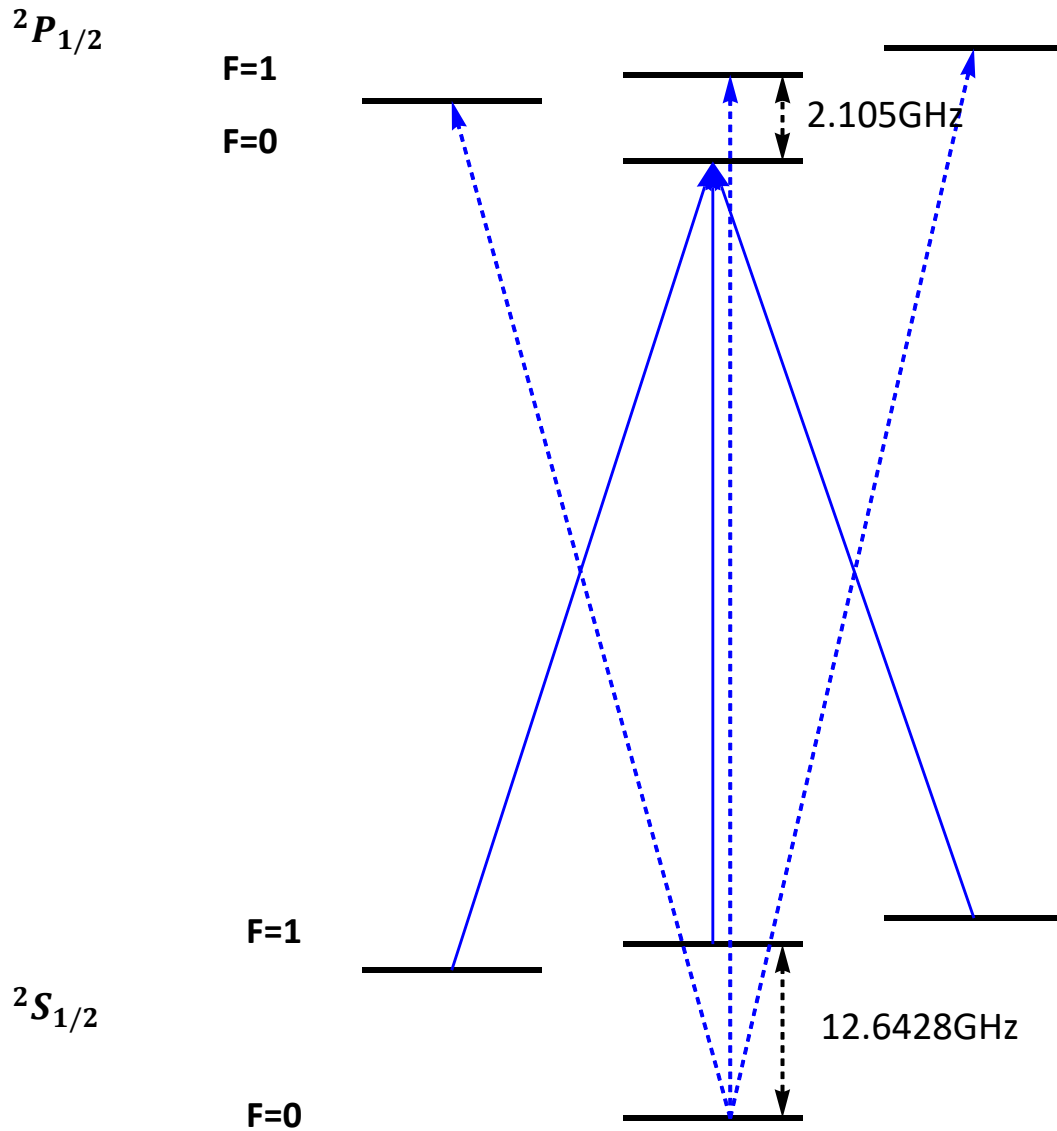
图 2.8　Schematic of Doppler cooling of ^{171}Yb$^+$. The Doppler cooling laser covers all the relevant energy levels. In the experiment, we generate the second sidebands of the 7.3720 GHzEOM, which can cover all the energy levels in the $^2S_{1/2}$ and $^2P_{1/2}$. To cool the three dimensions of an ion, the cooling beam need to have components along all the ion's dimension.

atom moves away from the source, it sees a frequency $\omega_1 - \frac{k}{c}$ of the cooling beam, which is far away from the resonance condition and hence absorbs less. Thus, on average, the ion experiences more momentum kick when moving opposite to the beam propagation than moving along the beam propagation direction. In the excited state, the ion emits the photon via spontaneous emission, however, this photon emitted in a random direction and on average its momentum is zero and the average momentum transferred to the ion from the cooling beam vanishes. Thus during one cycle, the ion slows down. In order to cool
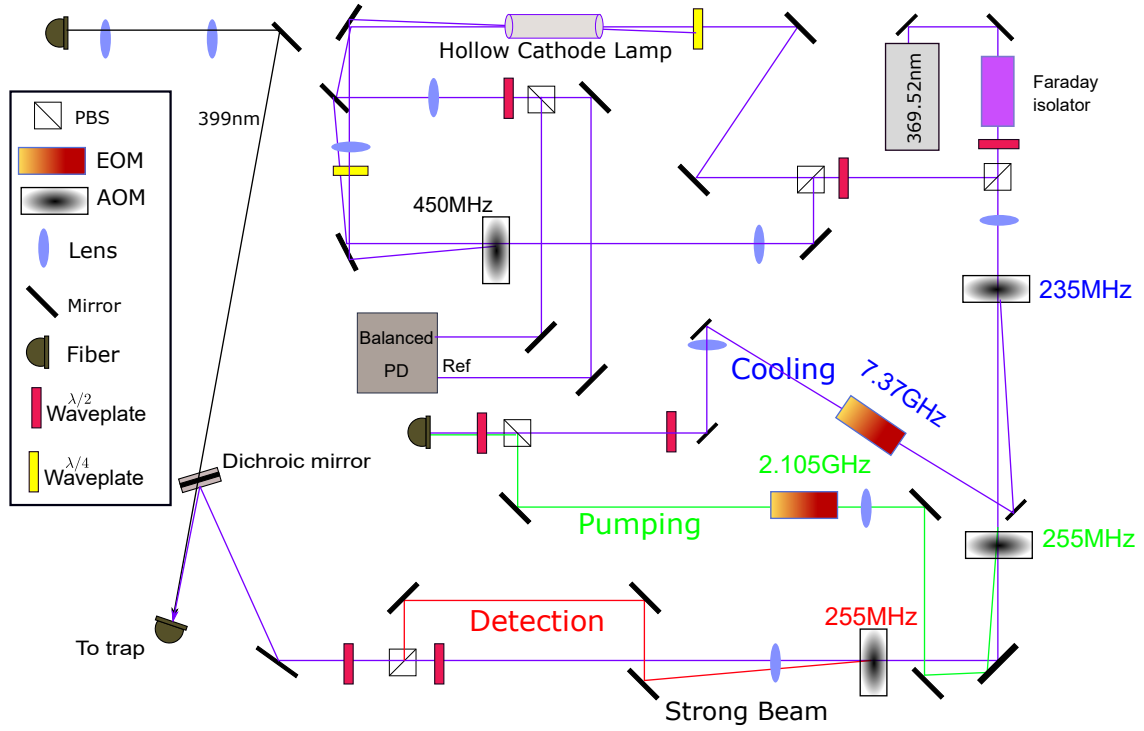
图 2.9 The optical path of 369.52 nm diode laser. The cooling beam, pumping beam, and detection beam are highlighted with blue color, green color and red color, respectively. The hollow cathode lamp and the balanced PD are used for the laser frequency stabilization. The 398.91 nm laser is coupled from another optical table through the fiber, which then combines with the strong beam in a PM fiber. Note here we show two digits after the dot of the laser wavelength for the reason loading ^{171}Yb$^+$ and ^{174}Yb$^+$ is on this range. Also due to we are not sensitive to the frequency of 398.91 nm laser, and itself is relatively stable in the short time, we do not stabilize this laser in the experiment.

the ion in three directions, we configure the cooling beam to have components in each direction as shown in Fig. 2.6.

On the other hand, though the average momentum of the photon emitted by the ion in the excited state is zero, however, the average kinetic of the phonon is proportion to $< v^2 >$, which is definitely not zero. This means the ion is heated from the emitted photon. The cooling process and the heating process end in a steady situation when their effects cancel each other. Then we reach the limit of Doppler cooling under the situation $\bar{n} = \frac{\Gamma}{2\omega_m}$, where Γ is the natural line-width of the cooling transition, $\bar{n}$ is ~ 10. Here, ω_m is the radial trap frequency. For this reason, we need the resolved sideband cooling to cool the motional degree of freedom, which I will discuss in the next chapter.

To cool down a ^{171}Yb$^+$, we need to take the following relevant energies into consid-

eration as shown in Fig. 2.8. Here, we use the second order sideband of the 7.3720 GHz EOM to modulate the cooling laser at 369.5253 nm. The 369.5263 nm laser is stabilized by the Ytterbium hollow cathode lamp[20]. In the optical path of this 369.5263 nm laser, we particularly use a blue color to highlight the cooling beam as shown in Fig. 2.9.
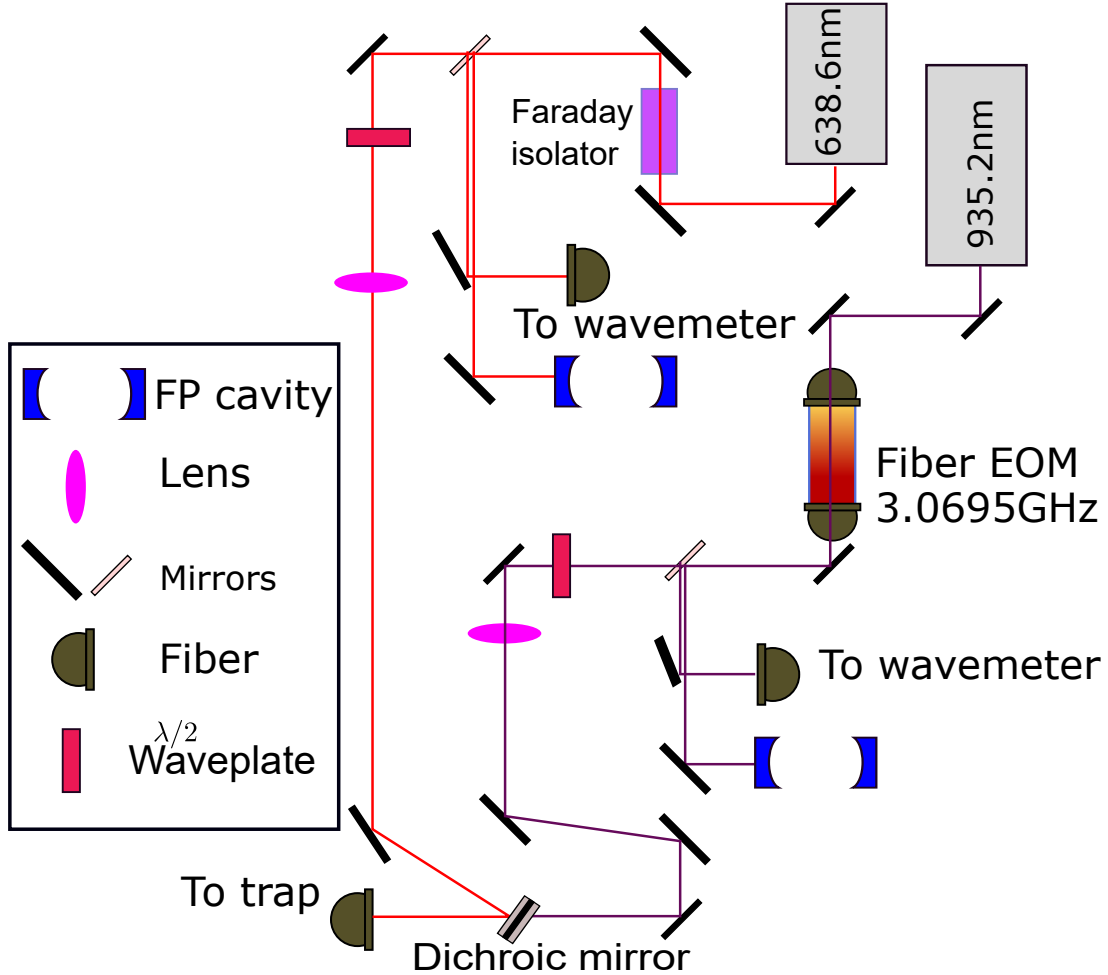
图 2.10　The optical path of the 935 nm and 638 nm repumping lasers. The 935 nmlaser is modulated by the fiber EOM with frequency 3.0695 GHz. We monitor its sideband with a commerical cavity. The 638 nm and 935 nm laser are coupled to the same fiber, which then sent to the trap. The 638 nm and 935 nm are both used to repumping the state back to the main cycle. Note we lock the 935 nm laser through the wavemeter which provides a reference. 638 nm is on the scan mode when we run the experiments, there no need to lock.

To close the cooling cycle, we apply the repumping laser 935.1882 nm and 638.6101 nm all the time. They are illustrated in Fig. 2.10, the line with purple color is the 935.1882 nm laser, while the red line is the 638.6101 nm laser. We couple these two lasers to the

same fiber and then direct to the trap in another viewport perpendicular to the cooling beam as shown in Fig. 2.6.

2.2.5　State initialization and detection
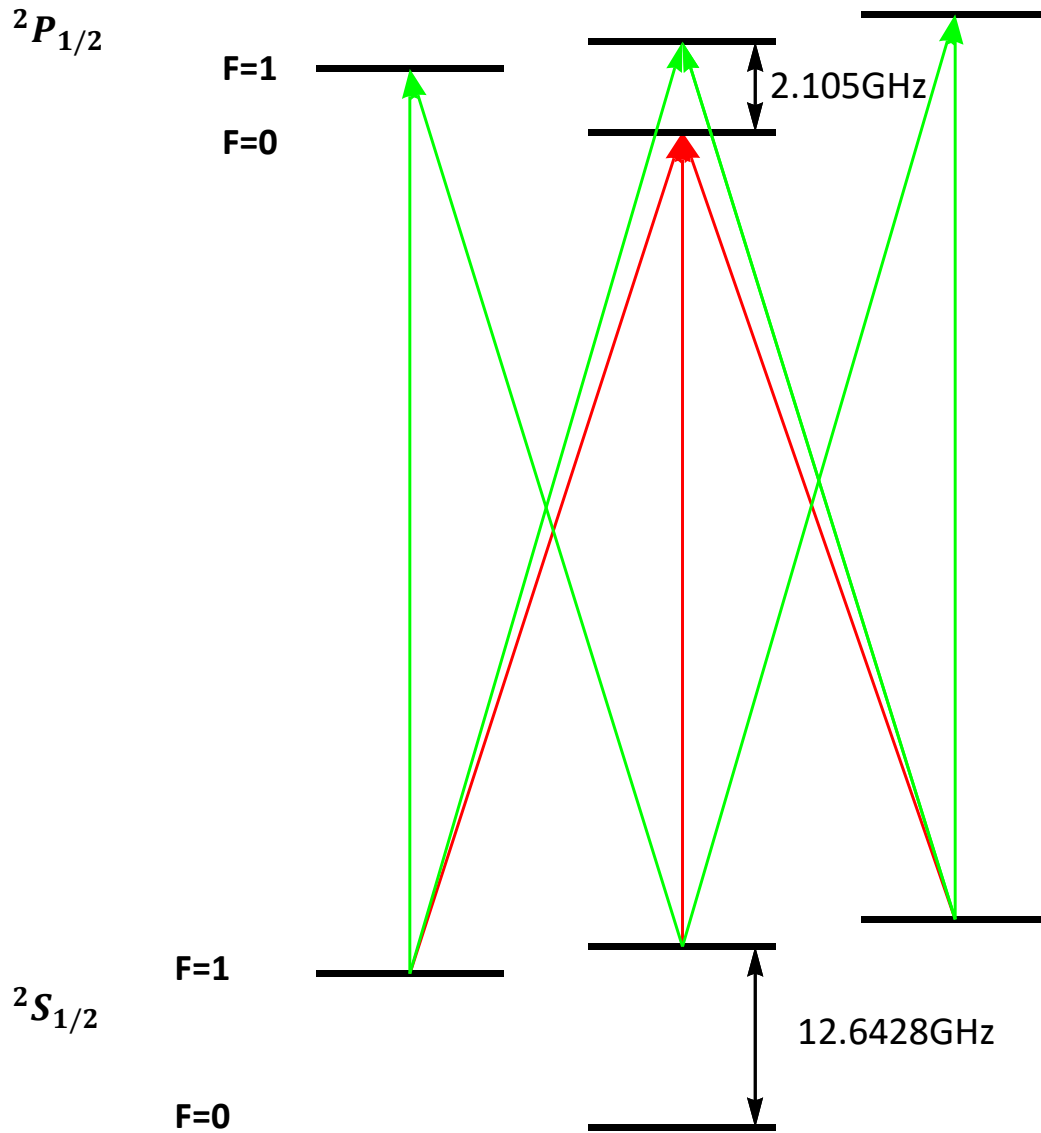
图 2.11　Schematic of optical pumping and detection of ^{171}Yb$^+$.

In all my experiments, I only use the clock state pair $|\downarrow\rangle, |\uparrow\rangle$ as the internal electronic state, which is insensitive to the first order of the magnetic noise. While in some cases, we may also use Zeeman pair $|\downarrow\rangle, |Z_+\rangle$ for the alignment of Raman lasers. The Zeeman symbols are shown in Fig. 2.11. The Zeeman splitting between the two nearby energy

levels is around 8 MHz, which means the magnetic field B is around 5 Gauss.

Before doing any experiment, we initialize the state to $|\downarrow\rangle$, which is implemented by optical pumping. Optical pumping covers the relevant energies with green color as shown in Fig. 2.11. This pumping is slightly different from that of cooling, it only needs first sideband of 2.1050 GHz EOM. This 2.1050 GHz makes it far detuned from the state $|\downarrow\rangle$, thus has no influence on the $|\downarrow\rangle$ state, which eventually drives all the state (around 99.5%) accumulated to the state $|\downarrow\rangle$.

In the optical path, I intentionally highlight the pumping beam with the green color as shown in Fig. 2.9. We then combine the pumping beam and the cooling beam with a polarize beam splitter (PBS) and then go to the same PM fiber. We do this for the sake of simplify the alignment of cooling and optical pumping beam. The optical path of the detection beam is shown in Fig. 2.9, with the red color highlighted. The detection beam is combined with the strong beam through the PBS, then enters into the same fiber with the 399 nm laser. We apply the detection laser for a certain of times, during which we collect the photons through the high N.A =0.63 lens that bought from PhotonGear company and then sent to the PMT or CCD system. For more details of the detection imaging system, I recommend you to see my colleague's thesis[17]. The detection that covers the relevant energies with red color is shown in Fig. 2.11. If the ion is in the state $|\downarrow\rangle$, which is far detuned from the detection beam and will not be driven to the excited state, thus, we will collect almost no fluorescence. If the ion is in the state $|\uparrow\rangle$, it will be driven to the state $^2P_{1/2}$, which will emit a lot of photons through the spontaneous radiation. We collect the photons with PMT for the state analysis.

第3章　Coherent Control of the ion-laser interaction through Raman transitions

In this chapter, I illustrate the theoretical part of the ion-laser interaction, then move to the experimental part of the Raman laser system. In the ion-laser interaction part, I will talk about the interaction between the two-level system and laser, then extend to the three-level Λ type system interact with the laser. Finally, we take the motional part of the ion into consideration, and derive the basic Hamiltonian in the trapped ion system. In the Raman laser system part, I discuss the laser configuration to implement the Raman transition and its related sideband cooling of the motional degree of freedom. I show the effort to improve the performance of our system and describe the experimental procedure to run an experiment. I show results of some experiments such as the generation of the coherent state, squeezed vacuum state and Schrödinger cat state. Finally, I briefly mention the imperfection of our system.

3.1　Ion-laser interaction

3.1.1　A two-level system atom-laser interaction

A two-level system atom, which is mathematically equivalent to a spin 1/2 particle. It has two energy levels and energy eigenstates that can be described by the 2×2 Pauli matrix. Here, we consider a two-level system atom with ground state $|\downarrow\rangle$ and excited state $|\uparrow\rangle$ interacts with the monochromatic light as shown in Fig. 3.1, the Hamiltonian of the system is composed of two parts, the static part H_0 and the atom-laser interaction part H_1

$$\hat{H}_0 = \frac{\hbar}{2}\omega\sigma_z, \hat{H}_1(t) = e\vec{r}.\vec{E}_0\cos(\omega_L t),$$

where ω and ω_L are the transition frequency of the two-level atom and the laser frequency, respectively. The interaction part can be further expanded in the energy representation of the two-level system as

$$
\begin{aligned}
\hat{H}_1(t) &= (|\downarrow\rangle\langle\downarrow| + |\uparrow\rangle\langle\uparrow|)e\vec{r}.\vec{E}_0\cos(\omega_L t)(|\downarrow\rangle\langle\downarrow| + |\uparrow\rangle\langle\uparrow|) \\
&= \hbar\frac{\Omega}{2}(\sigma_+ + \sigma_-)(e^{i\omega_L t} + e^{-i\omega_L t}),
\end{aligned}
\tag{3-1}
$$

26

$$|\uparrow\rangle$$

$$\Delta$$

$$\omega_{\mathrm{L}}$$

$$\uparrow$$

$$|\downarrow\rangle$$
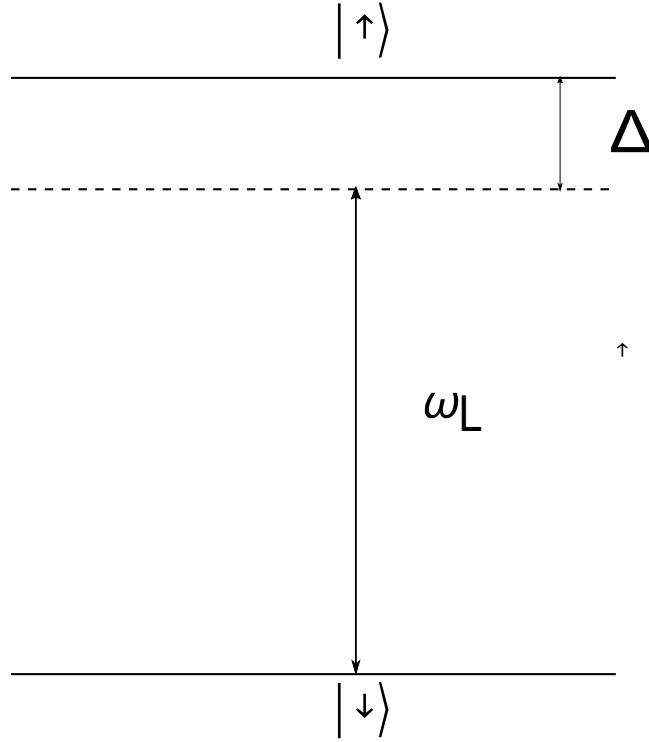
图 3.1　A two-level system atom-laser interaction.

where $\sigma_- = |\downarrow\rangle\langle\uparrow|$ $(\sigma_+ = |\uparrow\rangle\langle\downarrow|)$ is the raising(lowering) operator, and the Rabi frequency Ω (Here we assume it is real number) is defined as

$$\Omega = \frac{|e\vec{r}.\vec{E}_0|}{\hbar}. \tag{3-2}$$

Here, we assume the electrical field has almost uniform amplitude over the atom wavefunction, so we treat the amplitude as a constant $|E_0|$. In the interaction picture with respect to the static Hamiltonian $\hat{H}_0$, we transform the interaction part to the Hamiltonian $\hat{H}_{\mathrm{I}}(t) = \mathrm{e}^{i\frac{\hat{H}_0 t}{\hbar}}\hat{H}_{\mathrm{I}}(t)\mathrm{e}^{-i\frac{\hat{H}_0 t}{\hbar}}$

$$\hat{H}_{\mathrm{I}}(t) = \frac{\hbar}{2}(\sigma_+\mathrm{e}^{i\omega t} + \sigma_-\mathrm{e}^{-i\omega t})(\mathrm{e}^{i\omega_{\mathrm{L}}t} + \mathrm{e}^{-i\omega_{\mathrm{L}}t}) = \frac{\hbar}{2}(\sigma_+\mathrm{e}^{-i\Delta t} + \sigma_-\mathrm{e}^{i\Delta t}). \tag{3-3}$$

Here, we use the relation $\mathrm{e}^{i\frac{\hat{H}_0 t}{\hbar}}\sigma_+\mathrm{e}^{-i\frac{\hat{H}_0 t}{\hbar}} = \sigma_+\mathrm{e}^{i\omega t}$ and $\mathrm{e}^{i\frac{\hat{H}_0 t}{\hbar}}\sigma_-\mathrm{e}^{-i\frac{\hat{H}_0 t}{\hbar}} = \sigma_-\mathrm{e}^{-i\omega t}$, and apply the rotating wave approximation (RWA), where we ignore the fast oscillate term with frequencies $\pm(\omega + \omega_{\mathrm{L}})$. The $\Delta = \omega_{\mathrm{L}} - \omega$ is the frequency detuning between the laser frequency and the energy splitting. When the drive frequency is on resonance, we can observe the full contrast Rabi oscillation between $|\downarrow\rangle$ and $|\uparrow\rangle$. Moreover, the effect of such a perturbation slightly change the resonance frequency of the two levels of the atom

(known as the AC Stark shift), which can be described by an effective Hamiltonian of the following form

$$\hat{H}_{eff}(t) = -\frac{\hbar\Omega^2}{4}(|\uparrow\rangle\langle\uparrow| - |\downarrow\rangle\langle\downarrow|). \tag{3-4}$$

To simplify the calculation, actually, we will resort to the effective Hamiltonian theory[21]. In such systems, Hamiltonian has the following form

$$\hat{H}_{I}(t) = \sum_{n=1}^{N}(\hat{h}_{n}e^{-i\omega_n t} + \hat{h}_{n}^{\dagger}e^{i\omega_n t}), \tag{3-5}$$

where N is the total number of different harmonic terms in the interaction Hamiltonian. Then the effective Hamiltonian follows the form

$$\hat{H}_{eff}(t) = \sum_{m,n=1}^{N}\frac{1}{\hbar\bar{\omega}_{mn}}[\hat{h}_{m}^{\dagger}, \hat{h}_{n}]exp(i(\omega_m - \omega_n)t), \tag{3-6}$$

where $\bar{\omega}_{mn}$ is the harmonic average of ω_m and ω_n,

$$\frac{1}{\bar{\omega}_{mn}} = (\frac{1}{\omega_m} + \frac{1}{\omega_n}). \tag{3-7}$$

Here, we reconsider the previous two-level atom-laser interaction $\hat{H}_{I}(t)$ in the context of effective theory. We set $\hat{h}_1 = \frac{\hbar\Omega}{2}|\uparrow\rangle\langle\downarrow|$ and $\omega_1 = \Delta$, then we can quickly get

$$\hat{H}_{eff}(t) = -\frac{\hbar\Omega^2}{4}(|\uparrow\rangle\langle\uparrow| - |\downarrow\rangle\langle\downarrow|). \tag{3-8}$$

This is the effective Hamiltonian for the detuned laser.

3.1.2 A three-level Λ-type system atom-laser interaction

Consider the case of three-level Λ-type system, we have two harmonic terms (apply two lasers with two detunings), where we assume the direct optical transition between $|\downarrow\rangle$ and $|\uparrow\rangle$ is not allowed. Similar to that of the two-level system, we can consider the three-level system as a combination of two different two-level systems $|\downarrow\rangle, |e\rangle$ and $|\uparrow\rangle, |e\rangle$, which share the excited state $|e\rangle$ shown in Fig. 3.2, hence the Hamiltonian of the total

system is the sum of the two two-level system, written as

$$\hat{H}_{\mathrm{I}}(t) = \frac{\hbar\Omega_1}{2} |e\rangle \langle\downarrow| \, \mathrm{e}^{-i\Delta_1 t} + \frac{\hbar\Omega_2}{2} |e\rangle \langle\uparrow| \, \mathrm{e}^{-i\Delta_2 t} + h.c., \tag{3-9}$$

where h.c. stands for the Hermitian conjugate part of the preceding terms. We apply the effective Hamiltonian theory by setting $\hat{h}_1 = \frac{\hbar\Omega_1}{2} |e\rangle \langle\downarrow|$ and $\omega_1 = \Delta_1$, $\hat{h}_2 = \frac{\hbar\Omega_1}{2} |e\rangle \langle\uparrow|$ and $\omega_2 = \Delta_2$. Substituting these terms into Eq. (3-6) and calculate the four commutators, we obtain the effective Hamiltonian given by
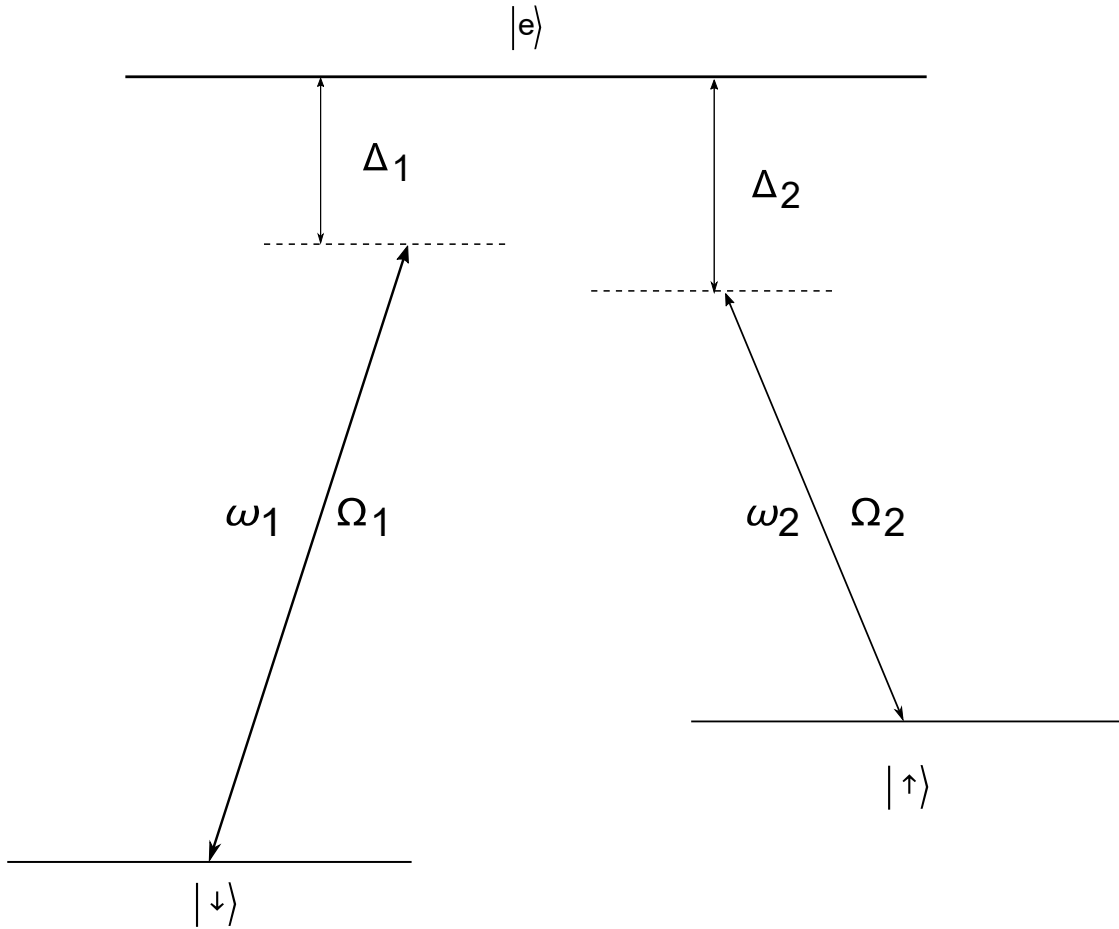
图 3.2 A three-level Λ-type system atom-laser interaction.

$$\hat{H}_{\mathrm{eff}}(t) = -\frac{\hbar\Omega_1^2}{4}(|e\rangle \langle e| - |\downarrow\rangle \langle\downarrow|) - \frac{\hbar\Omega_2^2}{4}(|e\rangle \langle e| - |\uparrow\rangle \langle\uparrow|)$$
$$+ \frac{\hbar\Omega_1\Omega_2}{4\bar{\Delta}}(|\downarrow\rangle \langle\uparrow|)exp(i(\Delta_1 - \Delta_2)t - |\uparrow\rangle \langle\downarrow| \, exp(-i(\Delta_1 - \Delta_2)t)). \tag{3-10}$$

Here $\frac{1}{\Delta} = \frac{1}{\Delta_1} + \frac{1}{\Delta_2}$. The first two terms are the AC Stark shifts that related to the two lasers, which drive the corresponding two-level system. The second pair of terms represent transitions between the $|\downarrow\rangle$ and $|\uparrow\rangle$, and it is the well known Raman transition, which play an center role in my experiments. In the Raman transition, the detuning $\Delta_{1,2}$ is much more larger than that of the coupling strength $\Omega_{1,2}$, thus, we do not have any excitation to the state $|e\rangle$. Therefore, the Eq. (3-10) can be reduced to the effective two-level system as

$$\hat{H}_{\text{eff}}(t) = -\frac{\hbar\Omega_1^2}{4}\hat{I} + \frac{\hbar\Omega}{2}(\sigma_- exp(i(\Delta_1 - \Delta_2)t - \sigma_+ exp(-i(\Delta_1 - \Delta_2)t)), \qquad (3-11)$$

where we have used the relation $|\downarrow\rangle\langle\downarrow| + |\uparrow\rangle\langle\uparrow| = \hat{I}$, $\hat{I}$ is the identity matrix of the two-level system and assume $\Omega_1 = \Omega_2$, $\Delta = \Delta_1 = \Delta_2$, $\Omega = \frac{\Omega_1\Omega_2}{\Delta}$.

1. In this moment, for the sake of understanding the AC Stark in the Raman type transition. Firstly, we consider the two pairs of two-level system separately ($|\downarrow\rangle$, $|e\rangle$,and $|\uparrow\rangle$, $|e\rangle$), but with two lasers with frequencies $\omega_{1,2}$, Rabi frequencies $\Omega_{1,2}$, are applied together all the time, then the AC Stark shift experienced by the state $|\downarrow\rangle$ is $\Delta_{\text{AC}}(|\downarrow\rangle) = -\frac{\hbar\Omega^2}{4\Delta} - \frac{\hbar\Omega^2}{4(\Delta+\omega_{\downarrow\uparrow})}$, similarly, the AC Stark shift experienced by the state $|\uparrow\rangle$ is $\Delta_{\text{AC}}(|\uparrow\rangle) = -\frac{\hbar\Omega^2}{4\Delta} - \frac{\hbar\Omega^2}{4(\Delta-\omega_{\downarrow\uparrow})}$. So the AC Stark difference between the two levels is

$$\begin{aligned}
\Delta_{\text{AC}} &= \Delta_{ac}(|\downarrow\rangle) - \Delta_{ac}(|\uparrow\rangle) && (3-12)\\
&= -\frac{\hbar\Omega^2}{4(\Delta + \omega_{\downarrow\uparrow})} + -\frac{\hbar\Omega^2}{4(\Delta - \omega_{\downarrow\uparrow})}\\
&= -\frac{\Omega^2}{4\Delta}[(1 - \frac{\omega_{\downarrow\uparrow}}{\Delta}) - (1 + \frac{\omega_{\downarrow\uparrow}}{\Delta})]\\
&= -\frac{\Omega^2}{2\Delta^2} * \omega_{\downarrow\uparrow}. && (3-13)
\end{aligned}$$

   Here, we have used the Taylor expansion under the assumption that $\omega_{\downarrow\uparrow}$ is much more smaller than the detuning Δ.

2. $\Delta_{\text{AC}} < 0$, means the states $|\downarrow\rangle$ and $|\uparrow\rangle$ get closer together while interacting with the beams.

3. $\Delta_{\text{AC}} \propto \frac{1}{\Delta^2}$, while the two photon Rabi frequency $\Omega \propto \frac{1}{\Delta}$. Thus, the ratio of the difference AC Stark shift to the Rabi frequency can be further reduced by increasing the detuning Δ.

We can remove the difference part by moving into a new rotating frame, where we adjust the laser beat-note frequency to account for the AC Stark shift. Now when we

consider the experimental situation when an ion is confined in a harmonic potential, in which can move freely in the x direction (it can extend to the three dimension easily), interacting with the equal intensity Raman laser pairs whose frequencies are ω_1 and ω_2, respectively. The internal degree of freedom of the ion can be treated as two system, while the external degree of freedom is described by the equally spaced quantum harmonic oscillator. Thus, we need to modify the Hamiltonian correspondingly with the position part $\Delta k_x \vec{x}(t)$ (Δk_x is the net wave-vector of the Raman laser beams along x-direction) as follows

$$\hat{H}_I(t) = \frac{\hbar\Omega}{2}\sigma_+ e^{i(\Delta k.\vec{x}(t)-\Delta t+\phi)} + h.c.. \tag{3-14}$$

Here Δ is the detuning between the Raman laser and the internal resonance of the ion, Δk_x is the component of the wave vector of the Raman laser along the x-direction and the operator $\Delta k_x \vec{x}(t)$ is given by

$$k_x \vec{x}(t) = \eta(\hat{a}e^{-i\omega_m t} + \hat{a}^\dagger e^{i\omega_m t}), \tag{3-15}$$

where $\hat{a}^\dagger$ and $\hat{a}$ are the creation and annihilation operators for the harmonic oscillator $\eta = \Delta k_x x_0 = \Delta k\sqrt{\frac{\hbar}{m\omega_m}}$, m is the mass of the ion, and ω_m is the trap frequency. In fact, the parameter η is very small, hence, we can make the Lamb-Dicke approximation that is $exp(ik_x t) \approx 1 + ik_x$. This allows us to make the identification of three harmonic terms in this Hamiltonian

$$\hat{H}_I(t) \approx \frac{\hbar\Omega}{2}\sigma_+(1 + i\hat{a}e^{-i\omega_m t} + i\hat{a}^\dagger e^{i\omega_m t})e^{-i\Delta t+i\phi} + h.c.. \tag{3-16}$$

This Hamiltonian is the starting point for the engineering of our system. We can precisely tune the frequency beat-note to implement the carrier Hamiltonian, the red sideband (RSB) Hamiltonian and the blue sideband (BSB) Hamiltonian.

1. When the frequency beat-note is equal to the hyperfine splitting $\omega_{\downarrow\uparrow}$, that is $\Delta = 0$ the Eq. (3-16) can be simplified to carrier Hamiltonian as(under the RWA, where we ignore the fast oscillating terms with frequency $\pm\omega_m$)

$$\hat{H}_{\text{Carrier}}(t) = \frac{\hbar\Omega}{2}(\sigma_+ e^{i\phi} + \sigma_- e^{-i\phi}). \tag{3-17}$$
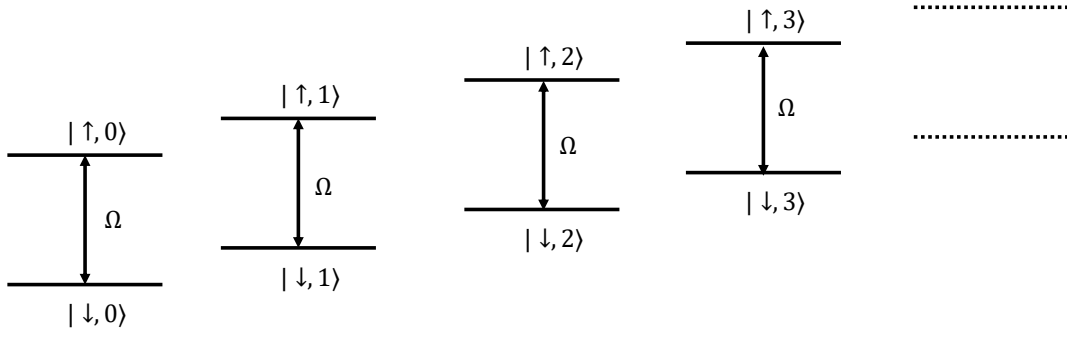
图 3.3 Carrier transition. Carrier transition couples the pair $|\downarrow, n\rangle, |\uparrow, n\rangle$ with constant Rabi frequency Ω.

For this case, we generate the resonant carrier transition between the state pair $|\downarrow, n\rangle, |\uparrow, n\rangle$ as shown in Fig. 3.3, with Rabi frequency Ω. The phase ϕ can be precisely controlled and serve as the direction of the rotating vector.
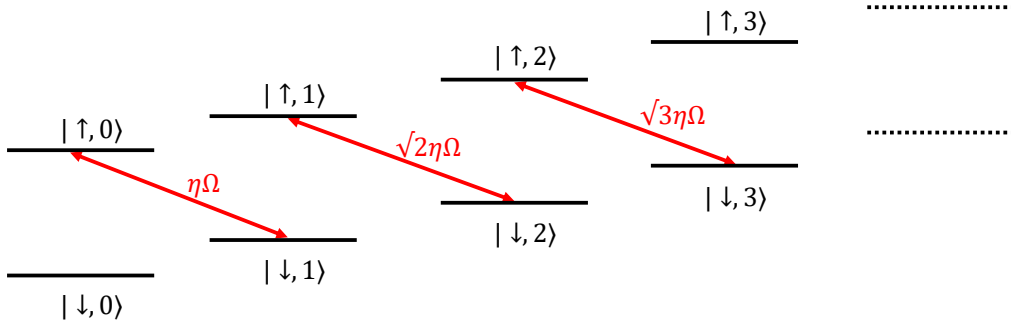
图 3.4 Red sideband transition. Red sideband couples the pair $|\downarrow, n+1\rangle, |\uparrow, n\rangle$ with Rabi frequency $\Omega_{n,n+1} = \sqrt{n+1}\Omega$.

2. When the frequency beat-note is equal to $\omega_{|\downarrow\uparrow\rangle} - \omega_m$, that is $\Delta = -\omega_m$ the Eq. (3-16) can be simplified to the RSB as(under the RWA where we ignore the fast oscillate terms with frequency $\pm\omega_m$)

$$\hat{H}_{RSB}(t) = i\frac{\hbar\eta\Omega}{2}(\hat{a}\sigma_+ e^{i\phi} - \hat{a}^\dagger\sigma_- e^{-i\phi}). \tag{3-18}$$

For this case, we generates the resonant red sideband transition between the state pair $|\downarrow, n+1\rangle, |\uparrow, n\rangle$ as shown in Fig. 3.4, with Rabi frequency $\Omega_{n,n+1} = \sqrt{n+1}\Omega$. We point out that for the state $|\downarrow, 0\rangle$, the Rabi sideband has no effect on it.

3. When the frequency beat-note is equal to $\omega_{|\downarrow\uparrow\rangle} + \omega_m$, that is $\Delta = \omega_m$ the Eq. (3-16) can be simplified to the BSB as(under the RWA where we ignore the fast oscillate
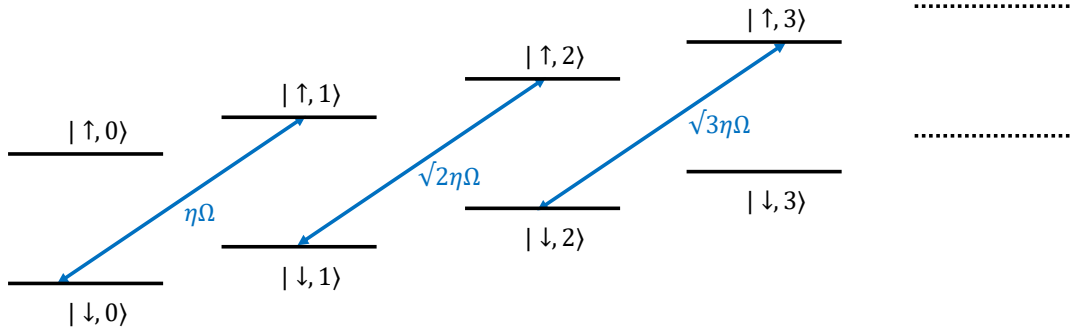
图 3.5 Blue sideband transition. Blue sideband couples the pair $|\downarrow, n\rangle, |\uparrow, n+1\rangle$ with Rabi frequency $\Omega_{n,n+1} = \sqrt{n+1}\Omega$.

terms with frequency $\pm\omega_m$

$$\hat{H}_{\text{BSB}}(t) = i\frac{\hbar\eta\Omega}{2}(\hat{a}^\dagger\sigma_+\mathrm{e}^{i\phi} - \hat{a}\sigma_-\mathrm{e}^{-i\phi}). \tag{3-19}$$

For this case, we generate the resonant blue sideband transition between the state pair $|\downarrow, n+1\rangle, |\uparrow, n\rangle$ as shown in Fig. 3.5, with Rabi frequency $\Omega_{n,n+1} = \sqrt{n+1}\Omega$.

4. In our work, we also use the internal state independent Hamiltonian for the engineer of the displacement operator and the squeeze operator. The displacement operator is described as Eq. (1-8), which involves the motional phonon degree of freedom, which only changes one phonon at a time. Thus, we can understand the Hamiltonian with the help of the excited state $|e\rangle$ in the transition as $|\alpha, n\rangle \leftrightarrow |e\rangle \leftrightarrow |\alpha, n+1\rangle$ shown in Fig. 3.6(a), in this manner, we have to change the Hamiltonian accordingly as

$$\hat{H}_{\text{I}}(t) \approx \quad \frac{\hbar\Omega_d}{2}|\alpha\rangle\langle\alpha|(1 + i\hat{a}\mathrm{e}^{-i\omega_m t} + i\hat{a}^\dagger\mathrm{e}^{i\omega_m t})\mathrm{e}^{-i\Delta t + i\phi}$$
$$+ \frac{\hbar\Omega_d}{2}|\alpha\rangle\langle\alpha|(1 - i\hat{a}\mathrm{e}^{-i\omega_m t} - i\hat{a}^\dagger\mathrm{e}^{i\omega_m t})\mathrm{e}^{-(-i\Delta t + i\phi)}. \tag{3-20}$$

Here $\Omega_d = \frac{\eta\Omega}{2}$ is the displacement Rabi frequency. Since only one of internal states $|\downarrow\rangle$ and state $|\uparrow\rangle$ is involved, the detuning Δ is simply the frequency beat-note difference between the two Raman lasers. For this case, when $\Delta = \pm\omega_m$, we derive the resonance displacement Hamiltonian as

$$\hat{H}_{\text{I}}(t) \approx \quad i\frac{\hbar\Omega_d}{2}|\alpha\rangle\langle\alpha|(\hat{a}\mathrm{e}^{i\phi} - \hat{a}^\dagger\mathrm{e}^{-i\phi}). \tag{3-21}$$

Here we take out constant part and state $|\alpha\rangle$ stands for state $|\downarrow\rangle$ or state $|\uparrow\rangle$. In the
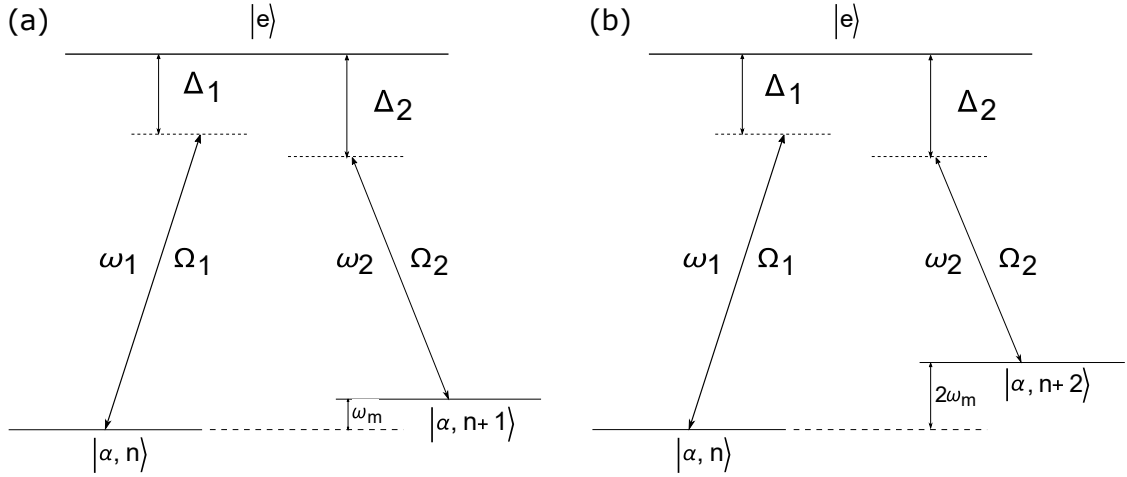
图 3.6　A three-level system for the displacement operator and squeeze operator. Panel (a) is the displacement operator where frequency beat-note between the two Raman lasers is one phonon difference ω_m. Panel (b) is the squeeze operator where frequency beat-note between the two Raman lasers is two-phonon difference $2\omega_m$.

experiment, we use this Hamiltonian to generate the coherent state.

5. For the squeeze operator, similar to the displacement operator, the main difference lies that it involves two phonons creation and annihilation simultaneously as shown in Fig. 3.6(b). When $\Delta = \pm 2\omega_m$ (consider the second order of the Taylor expression), we obtain the squeeze Hamiltonian as

$$\hat{H}_I(t) \approx \frac{\hbar \Omega_s}{2} |\alpha\rangle \langle \alpha| (\hat{a}^2 e^{i\phi} - \hat{a}^{\dagger 2} e^{-i\phi}). \tag{3-22}$$

Here $\Omega_s = \frac{\eta^2 \Omega}{2}$ is the squeeze Rabi strength, and state $|\alpha\rangle$ stands for state $|\downarrow\rangle$ or state $|\uparrow\rangle$. In the experiment, we generate the squeezed vacuum state.

3.2　Raman pulse laser and control system

In the previous section, we theoretically study the ion-laser interaction. In the following part, we will focus on the experimental part of engineering the ion-laser interaction. Experimentally, to manipulate the motional degree of freedom, we use the Mira picosecond laser to generate the pulse train. The repetition rate of the pulse train is 76.21 MHz and the maximum output power is about 230 *mW*. This power is large enough for a single ion experiment, and I use this Mira laser through my entire PhD carrier. Note that we bought a new Mira which more than twice higher output power from Coherent company. This new Mira is on the way to deal with the multi-ion experiments in the other optical

table.

The overview of the optical path for the Raman-laser system is shown in Fig. 3.7. In the optical path, we use two acousto-optic modulators (AOMs) to control each single Raman beam individually. We choose the +1 first sideband of the AOMs for the experiment. The intensities and frequencies of these sidebands are directly related to power and frequency of the modulation local oscillator. In the experiment, we fix AOM1's frequency to 213 MHz, while tuning the AOM2's frequency to engineer the carrier, RSB or BSB as experimental requirement. We particularly note the two pin-holes in the optical path serve as a reference of the ion. We carefully design the distance between the pin-whole and ion, such that the ion's images focus at this two pin-holes. The delay line is used to adjust the optical length of Raman 1 beam so that it can have the same optical length as that of Raman 2 beam. Since the delay line can only tune small range of distance, hence, we need to carefully design the schematic of the optical path in advance.

图 3.7　The optical path of the Raman laser system. We use the +1 first sideband of both AOMs as the control of single Raman laser. The $\frac{\lambda}{2}$ and $\frac{\lambda}{4}$ wave-plates are used to gain full control of the polarization of the Raman beams. The two pinholes are imaged to the ion, which is used for the alignment of Raman laser. The AOM2's path has considered the image relay, which images the AOM2 to ion. The intensity fluctuation is monitored through the output of PD. The delay line is to equalize the optical path of Raman 1 and Raman 2 beam.

图 3.8　Clebsch-Gordon coefficients between $^2S_{1/2}$ and $^2P_{1/2}$ of ^{171}Yb$^+$. Based on the CG coefficient, we design the polarizations for the two photon Raman transition.

3.2.1　Alignment of single Raman laser with the hyperfine Zeeman state

Usually, we begin the alignment of the Raman beam by focusing on one single beam. In our case, we choose the single Raman 1 beam or Single Raman with the help of the hyperfine Zeeman state Z_+. The Zeeman splitting is around 8 MHz, and the hyperfine splitting 12.6428 GHz. The optical frequency from the frequency comb is described as a series of delta functions spaced according to

$$f = f_0 + n * f_{\text{rep}}, \tag{3-23}$$

where f_0 is the frequency modulation that applied to the AOM, and f_{rep} is the repetition rate that determined by the mode-locked laser. Besides the frequency part, we also consider the transition strength between different levels according to the Clebsch–Gordan (CG) coefficients. Here, I list the relevant levels that related in our system shown in Fig. 3.8.

From Fig. 3.8, we clearly see there are two possible combinations to achieve the transition between the $|F = 0, m = 0\rangle$ and $|F = 1, m = 1\rangle$ of $^2S_{1/2}$, which requires the polarization of π and σ_+ or σ_- component. Hence, we apply the vertical B (perpendicular to the optical table) field with a small tilt angle.
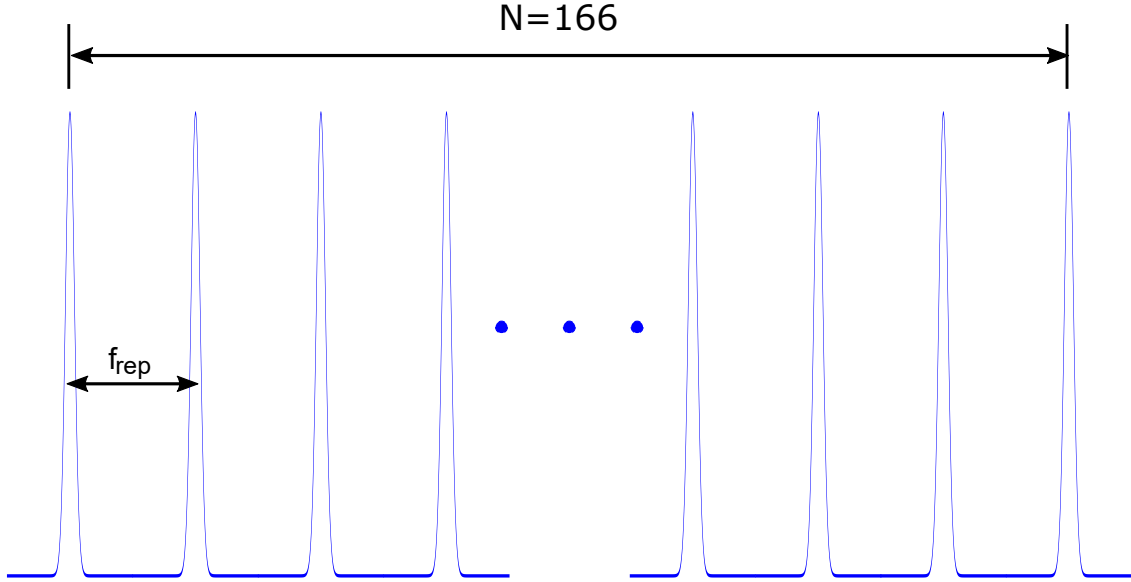
图 3.9　Beat-note from frequency comb of a single Raman beam. The beat note generated from the self-interference of the frequency comb satisfies $n * f_{rep} = \omega_{HF} + f_z$. The space between the two combs is the repetition rate of the pulse laser, which is around 76.21 MHz.
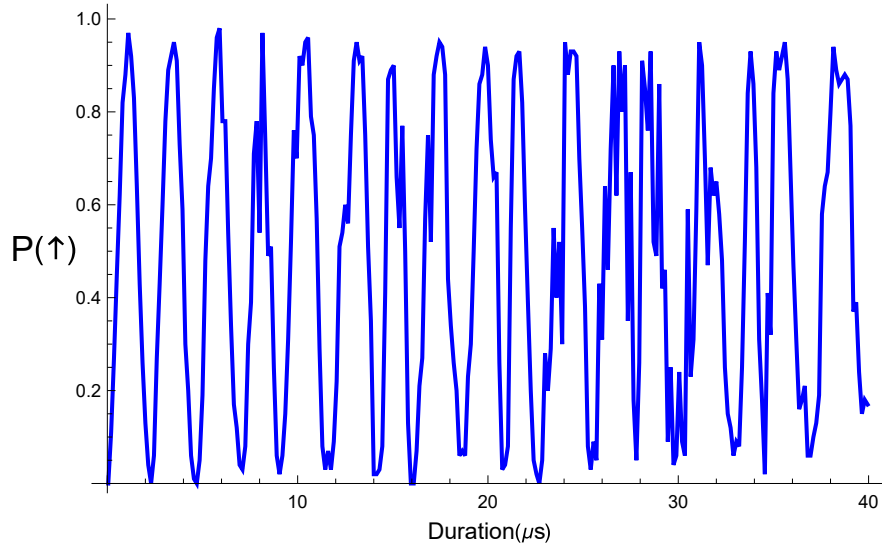
图 3.10　Rabi oscillation of single Raman beam on the Zeeman state Z_+.

The physic behind the transition driven by a single Raman beam is the beat-note

generated from the self-interference of the frequency comb that satisfies $\delta n * f_{\text{rep}} = f_{\text{HF}} + f_{\text{z}}$ shown in Fig. 3.9. Here f_{HF} is the hyperfine splitting, f_{z} is the Zeeman frequency. When it is resonant, we observe the Rabi oscillation as we scan the duration shown in Fig. 3.10. Once we optimize the Rabi oscillation strength by adjusting the laser alignment, we then move to the single Raman beam 2. At this moment, we only need to do the overlap with Raman beam 1. We repeat the same procedure on the Raman beam 1 until we achieve the optimal Rabi oscillation strength.
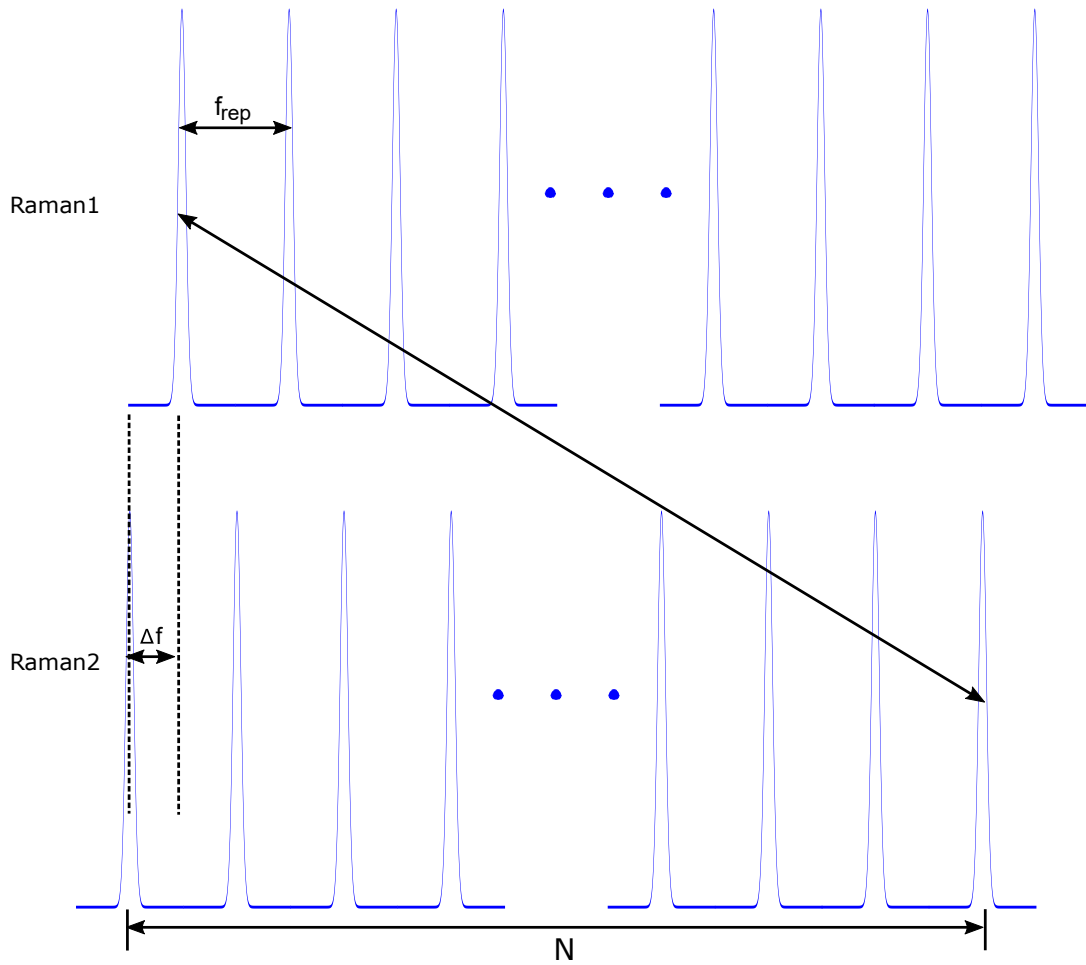
图 3.11　Beat-note of a pair of Raman beams. The frequency offset Δf is determined by the difference of the modulation frequency on the AOM1 and AOM2.

3.2.2　Manipulation of the $^{171}\text{Yb}^+$ clock state with two Raman lasers

To manipulate the coupling between the internal hyperfine clock state and its corresponding motional state, we need two Raman beams controlled individually with different

AOMs. In this configuration, we applied the horizontal B field(parallel to the Raman laser propagation), and the Raman lasers are with only σ_+ polarization by adjusting the $\lambda/2$ and $\lambda/4$ wave-plate accordingly. The frequency beat-note between the two Raman beams satisfies $f = \Delta f + N * f_{\text{rep}}$ shown in Fig. 3.11. Here, the Δf is the difference of the two AOM's modulation frequency, which is much smaller compared to f_{rep}. In our configuration with a repetition around 76.21 MHz, we draw this beat-note pattern as shown in Fig. 3.11. In the experiments, generally, we fixed the value of repetition rate, while change the modulation frequency of AOM2 to change the Δf, through this we can also observe the corresponding sideband transitions.

We scan the frequency of AOM2 and collect the fluorescence signal shown in Fig.3.12. Generally, it is easy to find the carrier peak, while hard to distinguish the sidebands. As we discussed in Chapter. 2, the trap frequency is proportional to the square root of RF drive power Ω_{rf} at the output of the helical resonator, this change can be seen in the shift of the sidebands in the spectroscopy. Note that we need to minimize the effect of Zeeman transition by changing the B field. The peaks are shown at the frequency $f_{\text{peak}} = f_{\text{carrier}} + i * \omega_{\text{x}} + j * \omega_{\text{y}}$, where i and j range from -2 to 2 with step 1, beyond this range, it is hard to observe due to the much weak coupling strength. Note here that to get all the relevant information of the peaks, we need to take Zeeman states and its motional sideband states, and also the micromotion sidebands into consideration.

After we carefully distinguish all the peaks in the spectroscopy, we know all the ingredients for the sideband cooling, that is the carrier f_{Car} frequency, red sideband frequencies (f_{RedX}, f_{RedY}). Here, we show the three main basic transitions, the carrier, RSB and BSB transition. In Fig. 3.13, we show the carrier peak, and its corresponding Rabi oscillation.

Generally, at the first glance, we may not know the exact π-pulse duration of the carrier (the duration that transferring $|\downarrow\rangle$ to $|\uparrow\rangle$ completely). Initially, we set a relatively large duration, then scan the frequency of AOM2 and get the on resonance frequency f_{car} through fitting, then we fix the frequency of AOM2, while scanning the duration of the carrier pulse, and observe the Rabi oscillation, through which we get the π-pulse time π_{car} of carrier by fitting. By iterating these steps, we get the precise f_{car} and π_{car}.

The BSB shown in Fig. 3.14 is almost the same as carrier, the main difference is its narrow peak width and slow Rabi oscillation. This is understandable as the coupling to the motional mode is of order η small than than of the carrier.
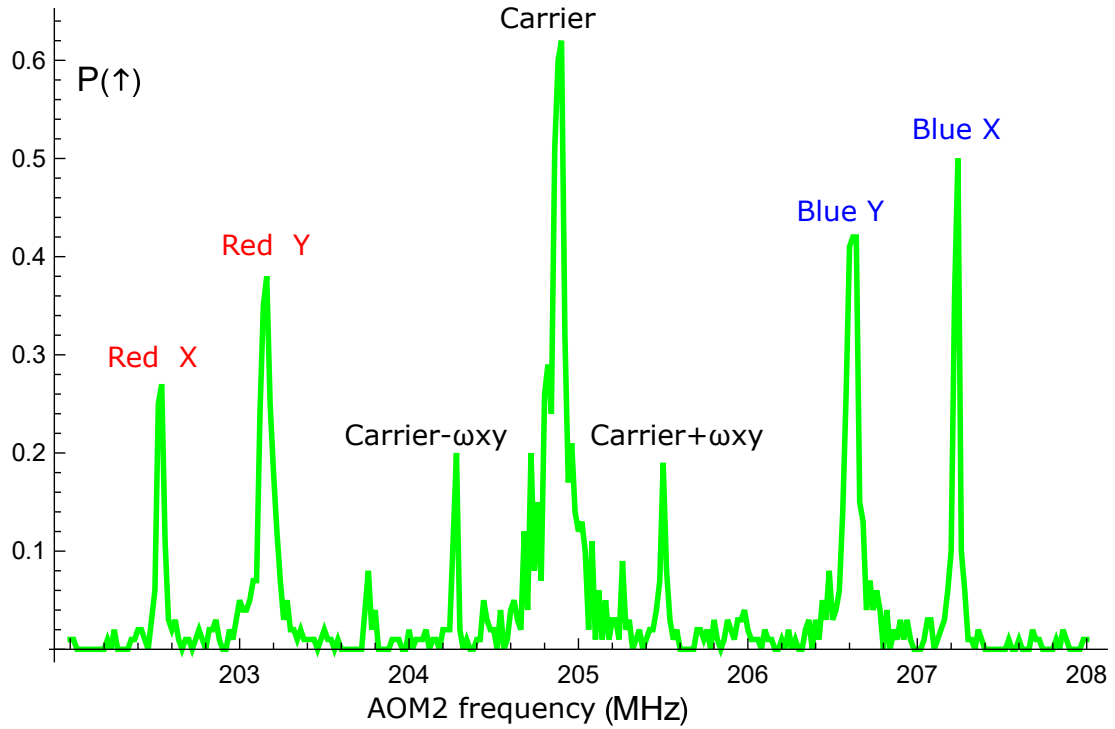
图 3.12   Spectroscopy of AOM2's frequency scan. When the frequency is resonant to the carrier or sidebands, which will drive to the state $|\uparrow\rangle$. The follows detection pulse then drive it to the excited state, which emits a lot of photons and show as the peak in the spectroscopy.
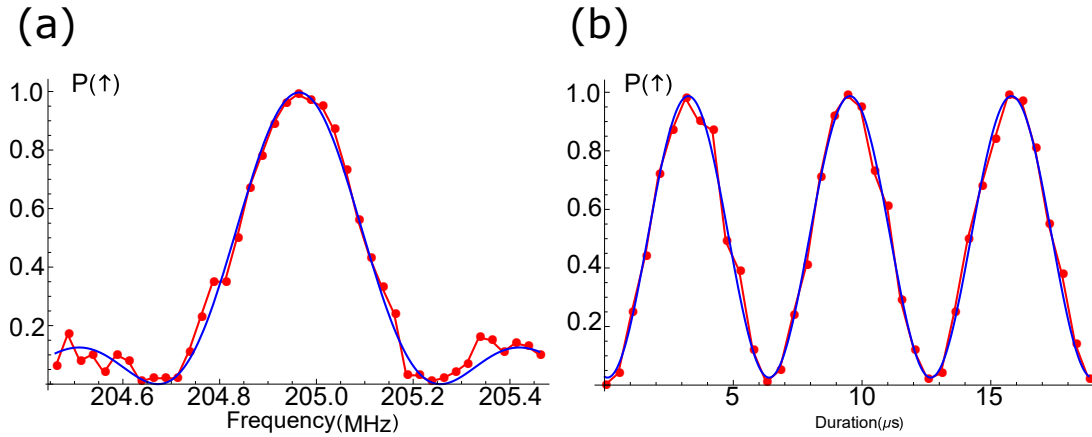
图 3.13   The frequency scan of carrier's peak and its Rabi oscillation.

The blue sideband is an important tool to extract the phonon number distribution, where it can map the phonon degree of freedom to the internal state, which can then be detected by the state-dependent fluorescence measurement. We use this method quite a lot in our experiments.

After sideband cooling, all the phonon populations are accumulated to the state $|\downarrow, 0\rangle$. Since the RSB will not drive the $|\downarrow, 0\rangle$, to find the resonance peak of the RSB, we should apply the carrier π pulse before the RSB pulse, the procedure to get the precise value of
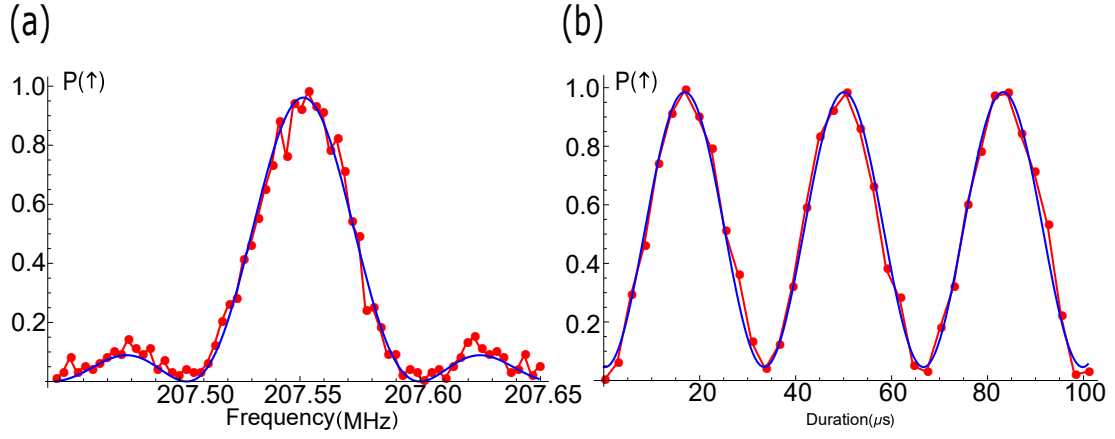
图 3.14　The frequency scan of of the peak of blue sideband and its Rabi oscillation.

f_{red} and π_{red} is the same. Here we show its peak and Rabi oscillation signal in Fig.3.15.
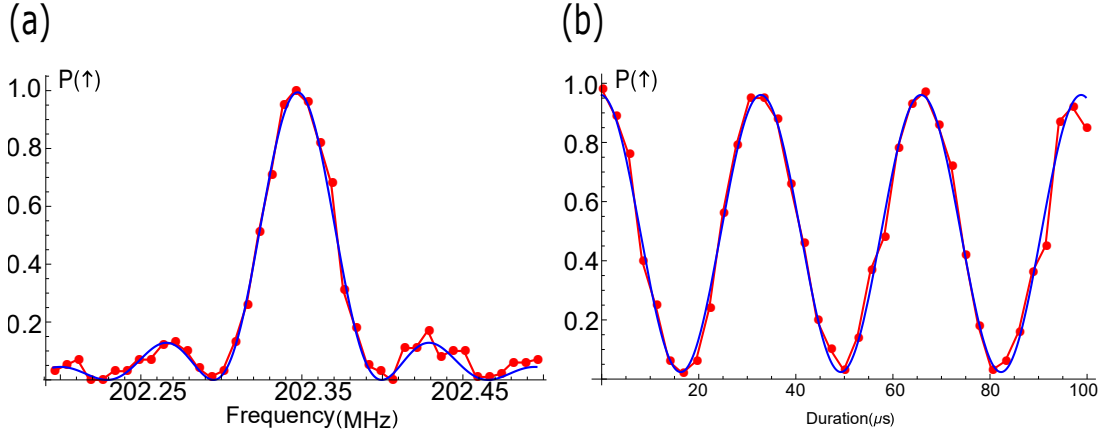
图 3.15　Scanning of the peak of red sideband and its Rabi oscillation.

We point out that we intentionally flip the data of Fig.3.15(a) for the sake of fitting, where it shows $|\downarrow\downarrow\rangle$. The red sideband is essential for the initialization of the state to the $|\downarrow, 0\rangle$, which require the sideband cooling.

3.2.3　Raman sideband cooling

Due to the Doppler cooling limit, the average phonon number is about 10, which is still very hot. The ion needs to be further cooled by mapping the motional degree of freedom to the spin and then removing the spin's entropy from the system through optical pumping technique, which we discussed previously. Fig. 3.16 shows the pulse sideband cooling scheme[6].

The ion in the $|\downarrow, n + 1\rangle$ will be driven to $|\uparrow, n\rangle$ through a resonant RSB π pulse, then followed by an optical pumping pulse, which drives the ion to the excited state, the state
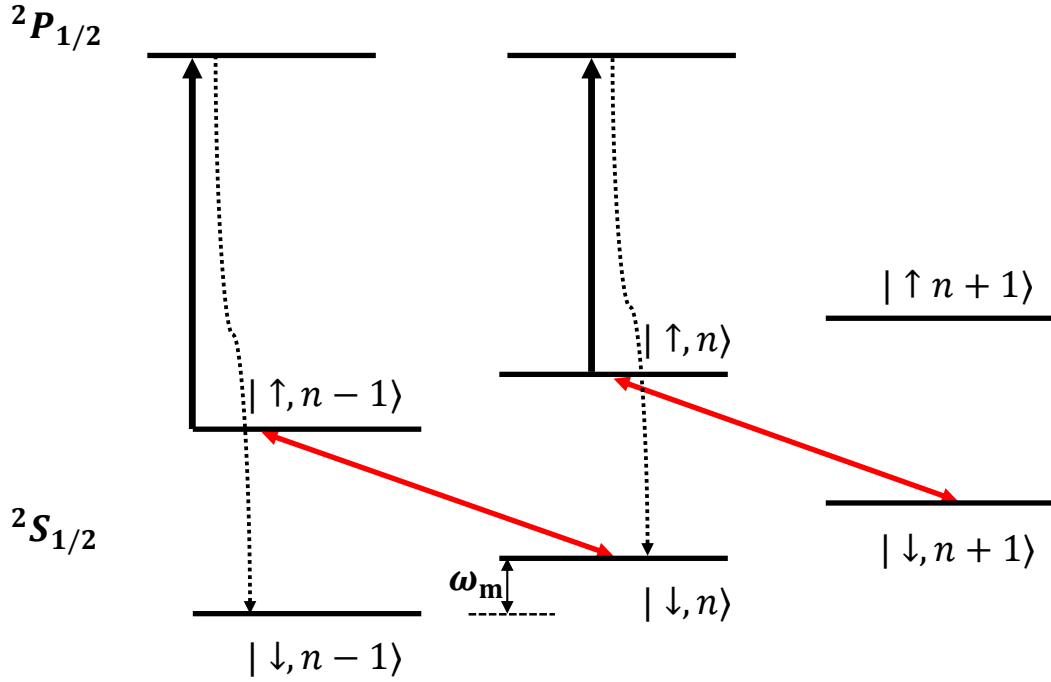
图 3.16 Scheme of Raman sideband cooling. The $|\downarrow, n+1\rangle$ state will be completely transferred to $|\uparrow, n\rangle$ by a RSB π pulse, then the optical pumping pulse drive the state to excited state, which quickly decay back to $|\downarrow, n\rangle$.

will soon decay back to the state $|\downarrow, n\rangle$, this forms a closed cycle. During one cycle, we remove the population from $|\downarrow, n+1\rangle$ to $|\downarrow, n\rangle$. By repeating this process, we finally move all the phonon populations to the ground state $|\downarrow, 0\rangle$, where the RSB pulse has no effect anymore. Note that we cool the mode X and mode Y before doing the experiment. It is better to cool them simultaneously rather than cooling one mode first and then cooling the other mode. During the cooling of the other mode, the mode that cooled will be heated from the environment. Since the cooling process requires longer time.

3.2.4 Optimization of the system performance

Before running any experiments, we optimize the system performance to reach a stable status. The unstable part of our system mainly include the fluctuation of Raman laser intensity and the drift of repetition rate, the unstable of trap power Ω_{rf} and the micromotion. I will discuss them in turn.

3.2.4.1 Stabilization of Raman laser intensity

The fluctuation of the power of the Raman laser will introduce noise into the system. We stabilize the intensity with the schematic shown in Fig. 3.17.
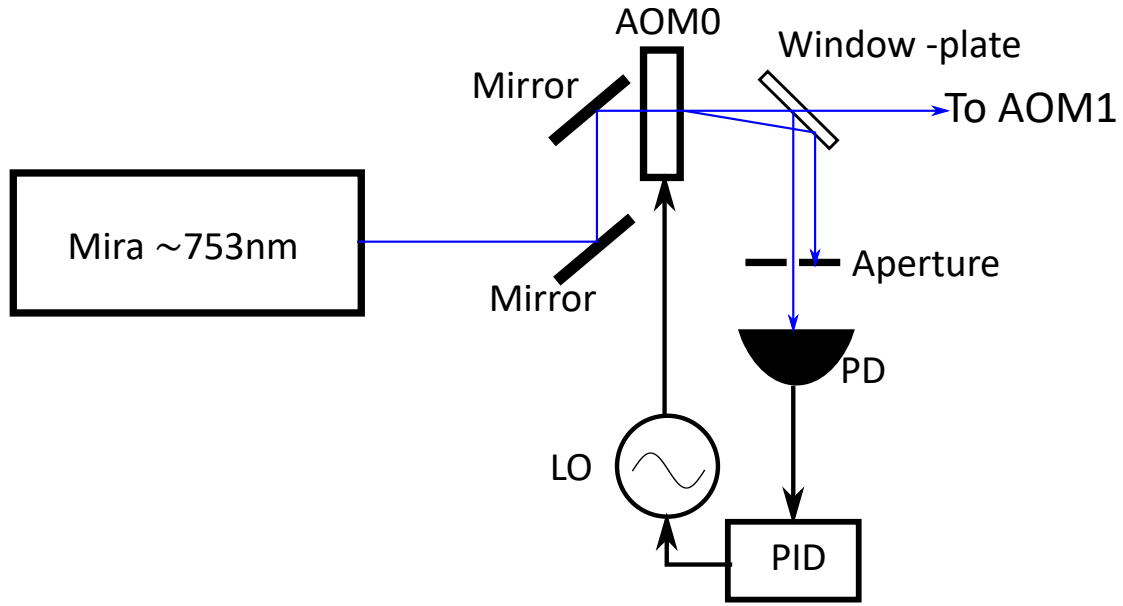
图 3.17　Schematic of the Raman intensity lock.

We use another AOM0 to sample parts of the power by its first order, we sample 1 % of the total power by the window plate (similar to a 1:99 BS) to the PD, which connects to the input of the proportional integral derivative (PID) controller, then feedback to the local RF source through the amplitude modulation. Since this drift is relatively slow, we do not need fast feedback.

3.2.4.2　Stabilization of Raman repetition rate

The repetition of the Raman laser, which is the key element to tune the beat-note, should also be stabilized. The schematic of the repetition rate is shown in Fig. 3.18. The basic idea[22] is expressed as follows, firstly, sample the higher order signal with a fast PD (ET-4000, from eot company), then we use a bandpass filter to take out the frequency around half of the hyperfine splitting ω_{HF}, then we amplify this signal and mix it with the local oscillator through the mixer. The output of the mixer is sent to a frequency double, which connects to a low pass filter and then connects to the PID as a input. The output of the PID will be applied to the piezoelectric transducer (PZT), which can slightly change the length of the cavity in the Mira. In the experiment, we bought a stepper motor actuator (TRA25PPD) and its controller SMC100 from the Newport company, which tunes the range of repetition more than 0.2 MHz. If the repetition is drift too much, we have to first move it back with this stepper motor. Note that there are mainly two reasons that we do not directly lock to the ω_{HF}. One is that we do not have such bandpass filter at such

frequency, the other is that the power at such high frequency is quite small.
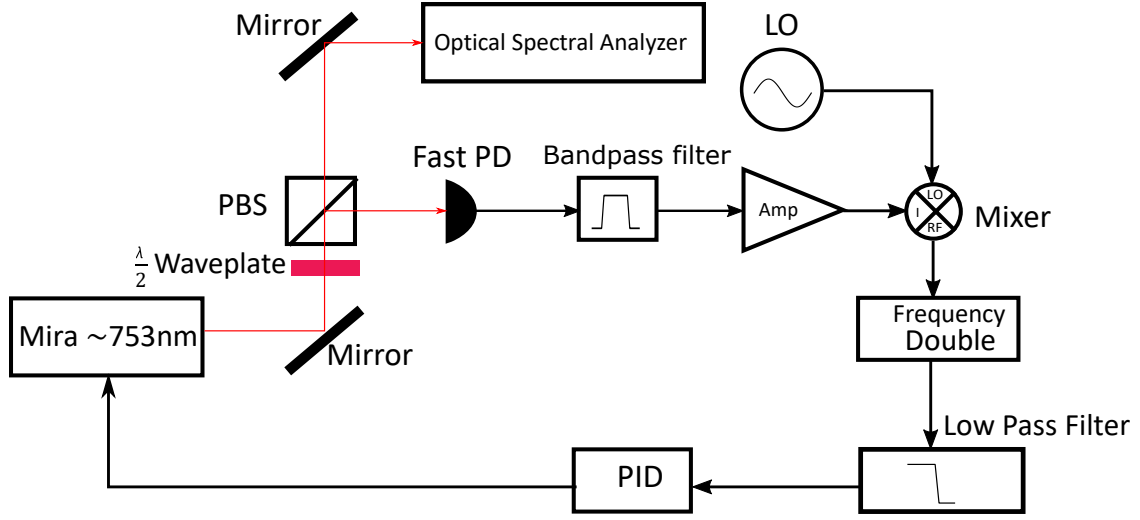
图 3.18　Schematic of the repetition rate lock. We sample the higher order of the Fast PD signal by a bandpass filter at frequency $n * f_{\text{rep}}$ around $\omega_{\text{HF}}/2$, then we use a mixer to get the difference between the sample signal $n * f_{\text{rep}}$ and the local oscillator (LO) source f_{LO}. The difference $|n * f_{\text{rep}} - f_{\text{LO}}|$ is sent to a frequency double, which followed by a low pass filter to choose the frequency at $2|n * f_{\text{rep}} - f_{\text{LO}}|$. The output of the frequency double is sent to the PID controller as a input, which produce the output to the PZT in the Mira laser.

3.2.4.3　Stabilization of trap power

The trap frequency $\omega_{\text{x,y}}$ is determined by the Eq. (2-12), where V_0 is proportional to the square root of the applied trap power. This is basically the only parameter that we can tune to change the trap frequency since Ω_{rf} is more or less fixed once we fixed the turn of the coil. The schematic of this intensity lock is shown as Fig. 3.19. Since the capacity of our trap is estimated about 2pF, so the capacity divider should be very small in order not to change the resonant helical frequency Ω_{rf}, and we sample the output of this capacity divider, which is about 1% of the total amplitude. This fast oscillation signal is then transformed to the DC voltage with the rectifier (fast response time around ns level), then we send this to the PID controller as input, which generate the output to the mixer. Here the mixer serves as the voltage controlled attenuator[23]. In this case, the feedback speed is around 1 μs, much compared to the amplitude modulation method that I use to mention the intensity fluctuation of the Raman laser (around 20 μs). After stabilizing the trap power, we enhance our motional coherence time around 5 times.
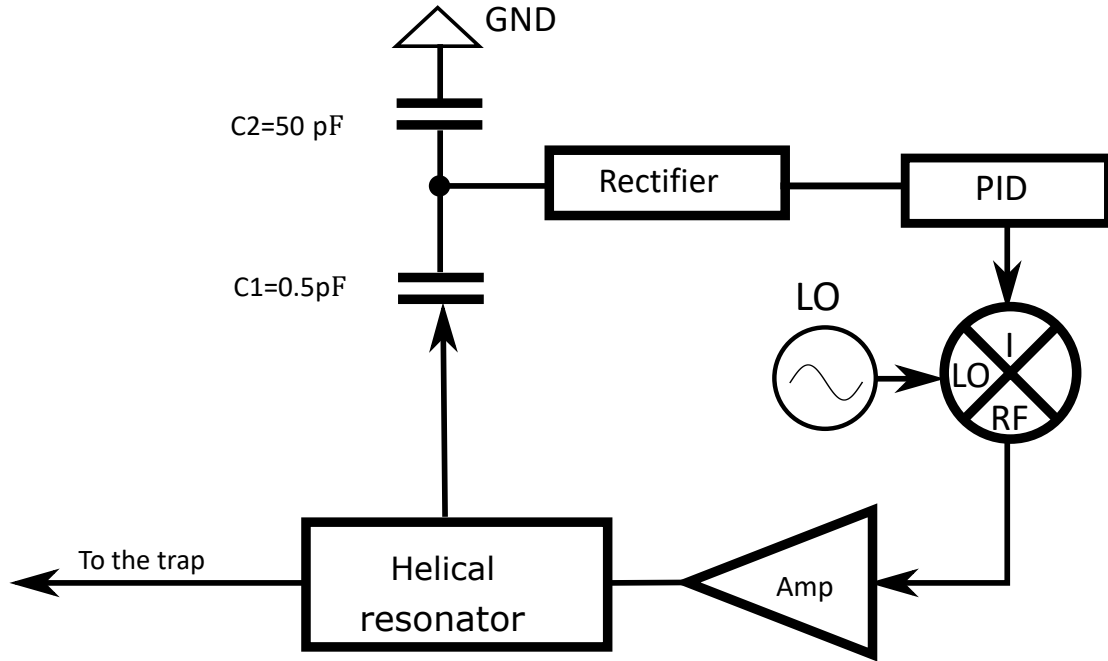
图 3.19 Schematic of intensity stabilization of the trap power. We use the fast response rectifier. The capacity divider sample 1/100 voltage of that to the trap and send it the PID controller, whose output goes to the mixer, which serves as voltage controller attenuator.

3.2.4.4 Compensation of micromotion

As discussed in Chapter 2, the micromotion will heavily reduce the ion's lifetime and make every thing worse. Thus, we need to minimize its effect before doing any serious experiments[24]. We use the trap power switch between the large power and the small power (7 dBm attenuator). I design this power switch on the basis of two switches (ZASW-2-50DR+) bought from the mini-circuit company. It is reasonable to assume the ion's position in large power is closer to the ideal position than that of small drive power. We mark this position in the CCD and switch to the small power, by looking at the ion's position we can adjust the DC voltage to move it to the marked position. Meanwhile, we alignment the beam to follow the ion. We iterate this step several times, and eventually we compensate the micromotion in $x - y$ plane quite well.

For the z direction, which is perpendicular to the optical table (perpendicular to the CCD), the position change in this direction cannot be seen by the CCD (but the brightness of ion is different if there is heavy micromotion in this direction). However, if there is any position difference in z direction between the large power and small power, this difference will show clearly in counts that collected by the PMT. By adjusting the DC voltage, we can reduce this difference in the counts. By iterating these two methods, we

shall arrive the same position and roughly same counts in the PMT. Note that we also experimentally minimize the effect via the Rabi oscillation of the micromotion sideband. If the micromotion is weak, we shall have small Rabi oscillation strength. For this micromotion compensation method, the target is to get the minimum Rabi oscillation strength by adjusting the DC voltages. Actually, the Rabi oscillation strength we get is only 1% of the carrier one under the same Raman intensity power, which is good enough to do the experiments.

3.3　The control system

To run a experiment, we pay much attention to the control system. As shown in Fig. 3.20, the key part is the sequencer which is implemented by the field programmable gate array(FPGA). This sequencer sends TTLs with predetermined duration to the RF switches, which control the modulations status of AOMs. If the modulation is on, then the AOM will have +1 sideband (we use only the first +1 sideband of AOM), which sent to the trap. If the modulation is off, then no beam passes. By controlling each laser's on and off individually, we implement the operations in sequence. The sequencer is controlled by the PC through the LabView and the Mathematica programming. The ion's scattering is collected by the PMT, which sent back to the FPGA as the input, the FPGA counts the number of the pulse during the detection pulse duration, and then sends the data to the LabView. The LabView shows the results dynamically.

To synchronize the pulse sequence, the FPGA uses the external 50 MHz square wave as the clock signal, which has a 10 MHz external reference from the Rb atomic clock. We note all the RF sources that used in the experiments are synchronized with the same Rb atomic clock. The PC communicates with FPGA through RS232 serial port. The PC can remote control the analog signal generator's frequency and amplitude via the Ethernet protocol by the Mathematica or LabView programming. The arbitrary waveform generator (AWG) generates waves with special form and duration according to the experimental requirement. Note that during the experiments, to manipulate the quantum state, we fix the frequency and amplitude of AOM1, while we only change that of AOM2's through AWG. Thus, we engineer all the Hamiltonian from this AWG as experiment requires.

The RF sources can be replaced by the high-quality direct-digital-synthesizer (DDS) source, which is of good quality in the context of phase noise. We bought the evaluation
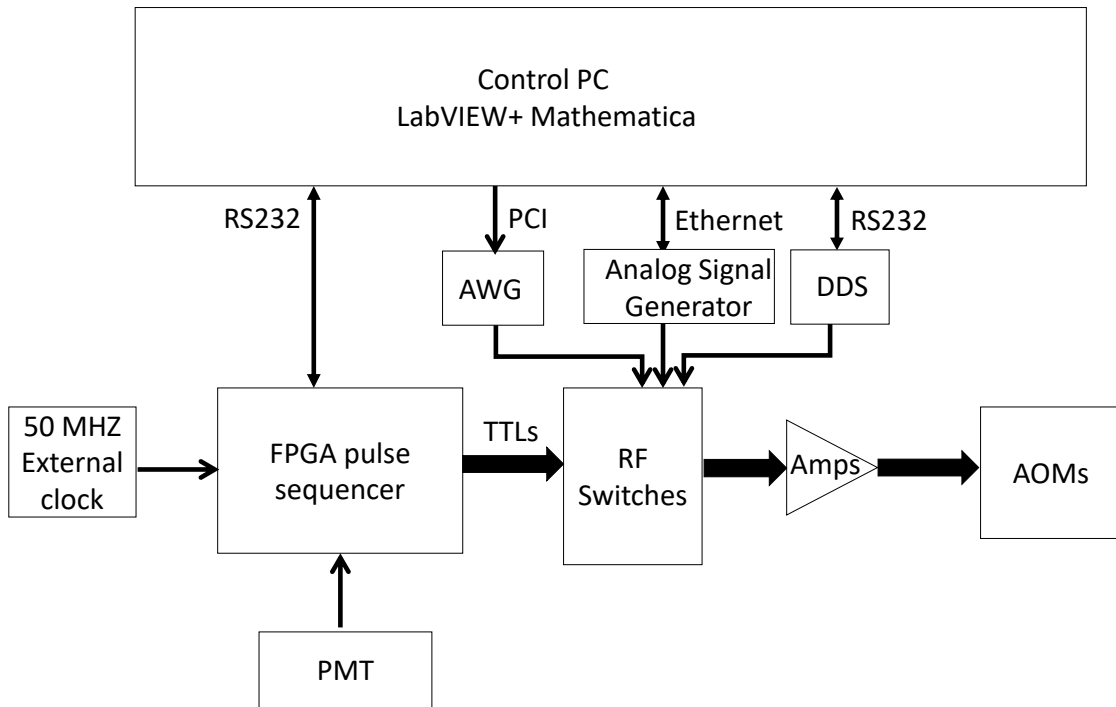
图 3.20　Overview of our control system. The key part of the control system is the sequencer which generates the TTLs to the switch on and off the RF signal that applied to the AOMs. The sequences are predetermined by the LabView in PC, which communicate with FPGA through RS232 serial port. All the parameters (amplitude, frequency) of RF sources are controlled by the PC through Ethernet protocol. The AWG is controlled through the PCI bus. All the RF sources and the AWG, 50 MHz external clock of the FPGA are synchronized with the same 10 MHz Rb atomic clock.

board of AD9912 and AD9910 from the ADI company, and I designed the power source for the circuit. I implemented the Verilog code for the control of the DDS through the FPGA. We send the parameters of the wave to FPGA through RS232 serial port. The FPGA can tune the DDS at a high speed around MHz. The AD9910 has eight profiles, which can initialize 8 wave parameters with different frequencies, amplitudes and phases. However, the AD9910 has only one output at a time, thus we select one of the 8 profiles by setting the address register value through external control TTLs signal. The advantage of AD9910 over AWG is that the pulse duration is not limited by the memory, which is extremely helpful for the long coherence time experiment[25]. The DDS could be widely used when we manipulate the multi-ion experiments. Though I developed these schematic and code for the DDS, I did not use this DDS for any of my experiments.

```
┌─────────────────┐
│  Doppler Cooling │
│      ~1ms        │
└─────────────────┘
        │
        ▼
┌─────────────────┐
│ Optical Pumping  │
│      ~3μs        │
└─────────────────┘
        │
        ▼
┌─────────────────┐
│ Sideband Cooling │
│     ~600μs       │
└─────────────────┘
        │
        ▼
┌─────────────────┐
│      State       │
│  Manipulation    │
│     < 1ms        │
└─────────────────┘
        │
        ▼
┌─────────────────┐
│   Fluorensence   │
│    Detection     │
│     ~60μs        │
└─────────────────┘
```
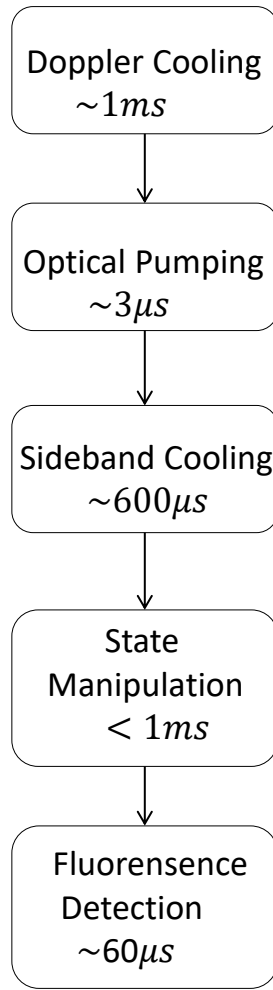
图 3.21　Procedures of a general experiment. The state manipulation is the essential part of the experiment, which is controlled by the AWG and dependent on the experiments request.

3.4 Experimental procedures and experimental results

After we illustrate the experimental control system, it would be quite straightforward to understand the experimental procedures. In Fig. 3.21, I draw a flowchart for a generally experimental procedure. We first Doppler cool the ion for about 1 ms, then we initialize the system to state $|\downarrow\rangle$ with optical pumping pulse (about 3 μs), follows by a sideband cooling pulse (around 600 μs) to cool the ion to the state $|\downarrow, 0\rangle$, which is the starting point for most of our experiments that involve phonon degree of freedom, then is the experimental operation to manipulate the state evolution (the pulse duration usually dependent on experiment request, this part usually requires our AWG), finally, state detection pulse with about 60 μs, during which we collect the photons emitted from the ion's scattering. Note here that the pulse duration is valid for a single ion.

3.4.1　Generation of coherent state

The generation of a coherent state could serve as an example of how we implement the state manipulation. When the beat-note frequency of Raman beams ($\omega_{R1} - \omega_{R2}$) is equal to the trap frequency ω_X (Here I only use X mode), the effective Hamiltonian in the interaction picture is described by

$$\hat{H}_D = \frac{i\hbar\eta\Omega_D}{2}(\hat{a}^\dagger e^{i\phi} - \hat{a}e^{-i\phi}), \tag{3-24}$$

where $\Omega_D = g_{R1}g_{R2}/\Delta_P$ is the vacuum Rabi frequency of the Raman transition from two laser beams, which are coupled to the transition $^2S_{1/2} \leftrightarrow ^2P_{1/2}$ with the Rabi frequencies of g_{R1}, g_{R2} and detuning Δ_P. The parameter ϕ is the relative phase of the two beams. The application of the Hamiltonian (3-24) performs the displacement operation $\hat{D}(\alpha) = e^{\alpha\hat{a}^\dagger - \alpha^*\hat{a}}$, where $\alpha = i\eta\Omega_D t/2$.

The displacement operation is nearly-equal performed for both qubit states $\{|\downarrow\rangle, |\uparrow\rangle\}$ due to the large detuning $\Delta_P \approx -(2\pi)12.9$ THz. The difference in the strength Ω_D between $|\downarrow\rangle$ and $|\uparrow\rangle$ can be written as $\frac{g^2}{2\Delta_P} - \frac{g^2}{2(\Delta_P+\omega_{HF})} \approx \frac{g^2}{2\Delta_P}\frac{\omega_{HF}}{\Delta_P} = \Omega_D\frac{\omega_{HF}}{\Delta_P}$, where $g = g_{R1} = g_{R2}$. Therefore, the strength difference should be less than $\frac{\omega_{HF}}{\Delta_P} \approx 10^{-3}$, which is not detectable in our current method.

We first apply the state independent pulse for a proper duration, then we apply the resonant blue sideband pulse for a fixed duration, finally we detect it. While we scan the blue sideband duration, we can get the Rabi oscillation signal as shown in Fig. 3.22(a). We get the phonon distribution as shown in Fig. 3.22(b) under the assumption that the state is coherent state.

We repeat the same procedures as previous and measure a series of state-dependent force pulse duration. We fit the Rabi oscillation signal and obtain the amplitude of the coherent state. We summarize the results in Fig. 3.23, the results indicate that the amplitude linearly increases with the pulse duration.

3.4.2　Generation of squeezed vacuum state

The generation of squeezed vacuum state is similar to that of the coherent state, the difference is that we need to tune the frequency beat-note of two Raman lasers to be $2\omega_X$. Thus, the Hamiltonian is reduced to Eq. (3-22). We show an experimental result for the squeezed vacuum state with $|\zeta| = 0.86 \pm 0.22$ in Fig. 3.24. Panel (a) shows the Rabi
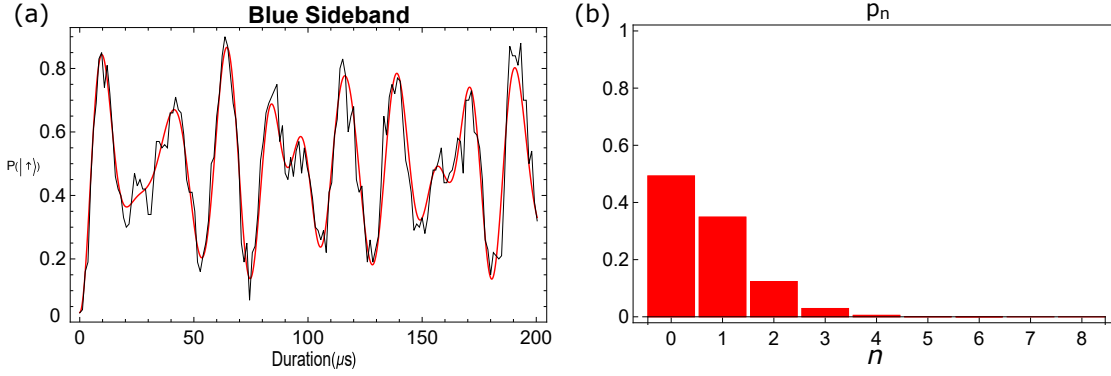
图 3.22　The Rabi oscillation of the coherent state with amplitude $|\alpha| = 0.84 \pm 0.037$. Panel (a) The Rabi oscillation is observed by applying a series of the resonance blue sideband pulse on the coherent state. Panel (b) is the corresponding phonon number distribution obtained by fitting under the assumption that it is a coherent state
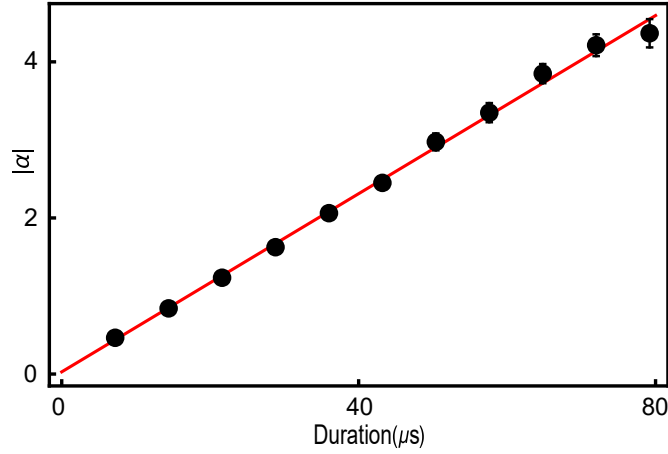
图 3.23　The displacement amplitude with the pulse duration. The amplitude of the coherent state linearly increases as duration increases.

oscillation signal, and panel (b) shows the phonon population distributed in even number states.

3.4.3　Generation of Schrödinger cat state

The most interesting thing in the quantum mechanic is to generate a Schrödinger cat state. In trapped ion community, researchers have used state-dependent force to generate it. Here, I reproduce the experimental results.

For this experiment, the state manipulation is merely the state dependent force. The state dependent force requires us to apply the BSB and RSB simultaneously with the same detuning but with opposite sign. The experimental scheme described in Fig. 3.25, where $\delta_b = -\delta_r$ and $\Omega_b = \Omega_r$.
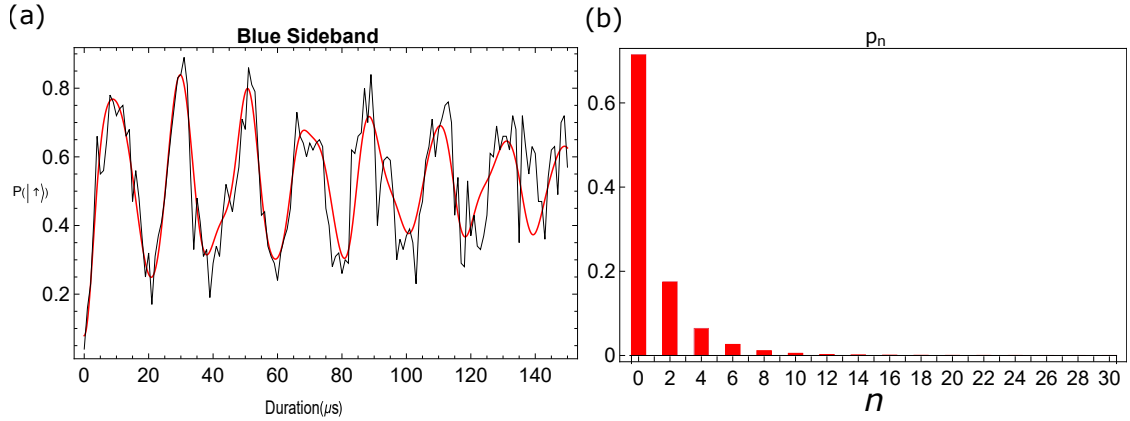
图 3.24 Squeezed vacuum state with $|\zeta| = 0.86 \pm 0.22$. The squeezed vacuum state is produced by applying the state independent squeeze operation, and the Rabi oscillation is observed by applying a series of the resonance blue sideband pulses.
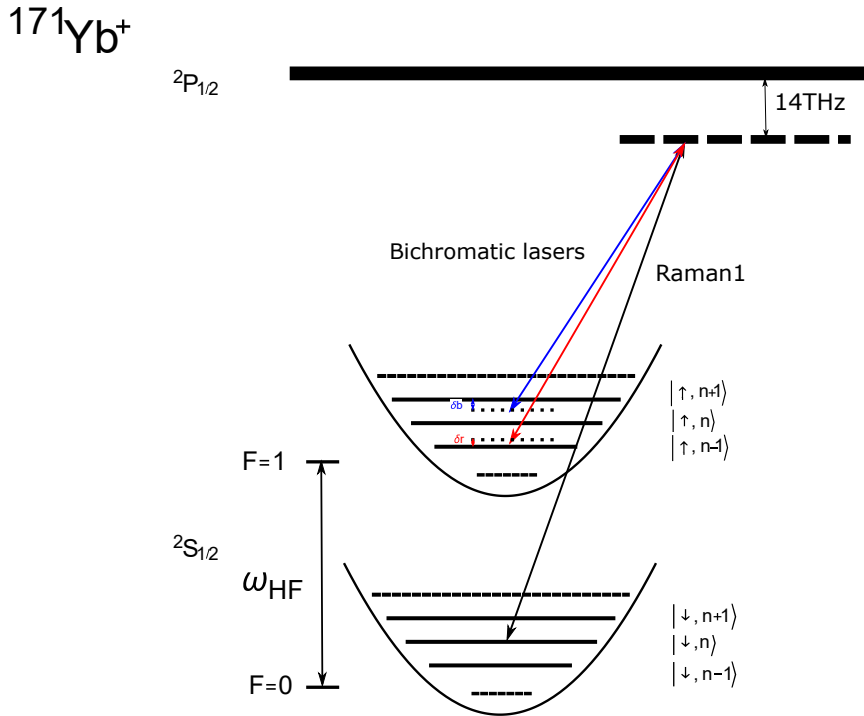
图 3.25 Experimental scheme to implement the state dependent force. The blue sideband and red sideband are applied simultaneously with equal Rabi frequency $\Omega = \Omega_b = \Omega_r$, and the detuning satisfied $\delta_b = -\delta_r$.

In the experiment, we notice that the unequal AC Stark shifts for the BSB and RSB even when they have the same Rabi frequency ($\Omega_b = \Omega_r$). In other words, when we apply these two beams together, they actually produce extra AC Stark shift (they can not cancel each other). We show the experimental AC Stark shift for both BSB and RSB in Fig. 3.26. Here, we do not take the AC Stark signs into consideration, but we note that blue and
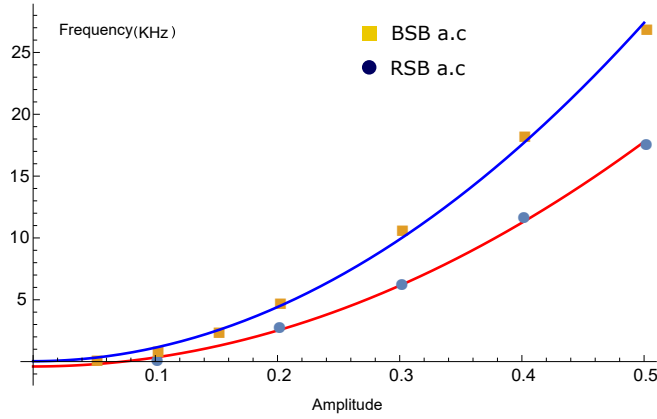
图 3.26 Imbalanced AC Stark shift of blue and red sideband. The horizontal is the amplitude of the AWG output, it ranges from 0 to 1, and the vertical axis is the absolute value of AC Stark.

red are with different signs. In Fig. 3.26, we clearly observe the blue sideband transition brings larger AC Stark shift than that of the red sideband. Experimentally, the AC Stark can be compensated by another far detuned pulse or compensated this part by adding or subtracting the extra AC Stark shift[26].

When we compensate the AC Stark shift well, we are able to see the results as shown in Fig. 3.27(a), where we set the $\delta_b = -\delta r = -(2\pi)10\,\text{kHz}$, in the ideal case without any decoherence, the ion should rotate back to the original at time $t = \frac{2\pi}{\delta_{|b,r|}}$. Actually, this evolution reproduces the Schrödinger cat state follows $\frac{1}{\sqrt{2}}(|\downarrow, \alpha(t)\rangle + |\uparrow, -\alpha(t)\rangle)$ with $\alpha(t) = \frac{g}{|\delta_b - \delta_r|}(1 - e^{i|\delta_b - \delta_r|t})$[27]. At $t = 0$, the two part are overlap in the original position, as time moves on, the two parts rotate in different directions, the two parts reach the maximum distance in phase space at $t = \frac{\pi}{\delta_{|b,r|}}$ as shown in Fig. 3.27(b), at later time it begin to revival, finally at $t = \frac{2\pi}{\delta_{|b,r|}}$ they merge together as shown in Fig. 3.27(c). Ideally, it come back to the original position, however, due to the heating and motional dephasing, its contrast reduced. For the case of $\delta_b = -\delta r = 0$, we clearly observe at time stamp e that the two parts totally separate as shown in Fig. 3.27(d). Since the displacement amplitude increases linearly with time, the two parts will continue to separate further and further, until they have no interference at all as shown in Fig. 3.27(e). This is demonstrated by the population of spin $P(\uparrow)$ stabilized at 0.5.

3.5　Imperfections of the system

Though we try our best to optimize the system here and there, unavoidable decoherence is still left there [28]. Here, I will present two main natural reservoirs, the heating reservoir and the dephasing reservoir, which interact with our phonon mode.
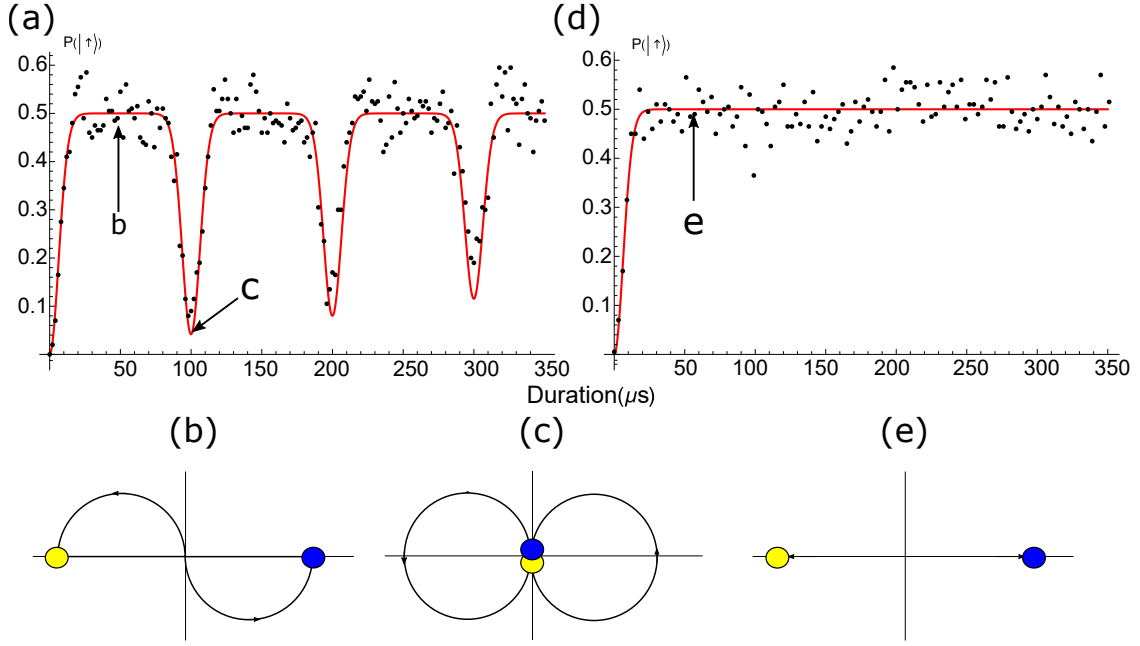
图 3.27　Schrödinger cat state generated from the state dependent force. Panel (a) with parameters $\delta_b = -\delta r = -(2\pi)10\,\text{kHz}$, the state follows the evolution $\frac{1}{\sqrt{2}}(|\downarrow, \alpha(t)\rangle + |\uparrow, -\alpha(t)\rangle)$ with $\alpha(t) = \frac{g}{|\delta_b - \delta_r|}(1 - e^{i|\delta_b - \delta_r|t})$. Panels (b-c) gives the sense for the state evolution when $\delta_b = -\delta r = -(2\pi)10\,\text{kHz}$. Panel (d) shows the situation when $\delta_b = \delta r = 0$, we observe here the two parts go far away and finally without any interference between the phonon state, panel (e) shows the two trajectories have no interference after time stamp e.

3.5.1　Heating rate measurement

The stray electrical field in the trap serves as the heating reservoir, which keeps kicking the ion and thermalizes the ion's phonon mode. Assume n_th is the average phonon number of the environment when it is equivalent with the system, it then follows the master equation[12]

$$
\begin{aligned}
\dot{\rho}(t) = &-\frac{\gamma}{2}n_\text{th}\left(\hat{a}\hat{a}^\dagger\hat{\rho}(t) - 2\hat{a}^\dagger\hat{\rho}(t)\hat{a} + \hat{\rho}(t)\hat{a}\hat{a}^\dagger\right) \\
&-\frac{\gamma}{2}(n_\text{th} + 1)\left(\hat{a}^\dagger\hat{a}\hat{\rho}(t) - 2\hat{a}\hat{\rho}(t)\hat{a}^\dagger + \hat{\rho}(t)\hat{a}^\dagger\hat{a}\right).
\end{aligned}
\tag{3-25}
$$

Here γ is the coupling strength between the ion motion and the thermal reservoir, n_th is the average phonon number when the system is in equilibrium with the environment. In our model, the effective temperature of the thermal reservoir is infinite, which makes n_th extremely large and thus we have $\gamma n_\text{th} \approx \gamma(n_{\text{th}+1})$. It is natural to define the heating rate as γn_th, which is measured as 3 quanta s^{-1} in our system. However, the heating rate is worse
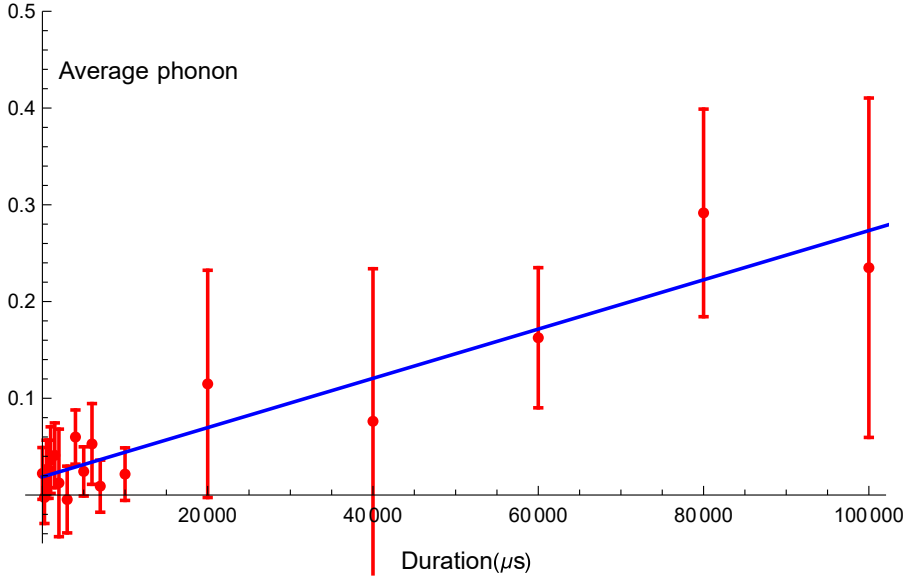
图 3.28　The heating rate of the phonon mode of our blade trap. We measure the heating rate by measuring the average phonon of the system that interacts with the environment heat bath for a proper time after the sideband cooling. The heating rate is estimated to be $\gamma n_{\text{th}} \approx 3$ phonon/s.

around 70 quanta s^{-1} when I run the experiment simulation of quantum Rabi model. We do not have a clear explanation of it. It probably due to the pollution of the surface of the blade from the oven.

3.5.2　Motional coherence measurement

The motional dephasing reservoir comes from the drift of trap frequency ω_{m}, which is dominated by the fluctuation of driving power of the trap.

$$\dot{\hat{\rho}}(t) = -\Gamma \left(\hat{\rho}(t)\hat{a}^\dagger \hat{a}\hat{a}^\dagger \hat{a} - 2\hat{a}^\dagger \hat{a}\hat{\rho}(t)\hat{a}^\dagger \hat{a} + \hat{a}^\dagger \hat{a}\hat{a}^\dagger \hat{a}\hat{\rho}(t) \right). \tag{3-26}$$

Here Γ is the dephasing parameter. We measure the coherence time τ through the Ramsey-type experiments of the superposition motional states $(|0\rangle + |1\rangle)|\uparrow\rangle$, which is $1/\Gamma$. The Ramsey type measurement is performed as follows: First, we apply a carrier $\frac{\pi}{2}$ pulse, the state evolves from $|\downarrow, 0\rangle$ to $\frac{1}{\sqrt{2}}(|\downarrow, 0\rangle + |\uparrow, 0\rangle)$, then we apply a BSB π pulse, which end with the state $\frac{1}{\sqrt{2}}(|\uparrow, 0\rangle + |\uparrow, 1\rangle)$, then we delay for a time ΔT, follows that we reverse the process by applying the BSB π pulse and the carrier $\frac{\pi}{2}$ pulse. We extract the contrast and plot it show in Fig. 3.29. We fit the data with formula $A * Exp(-t/\tau)$ and obtain τ around 2.5 ms. Note that before the stabilization of the driving power, τ is only about 500 μs.
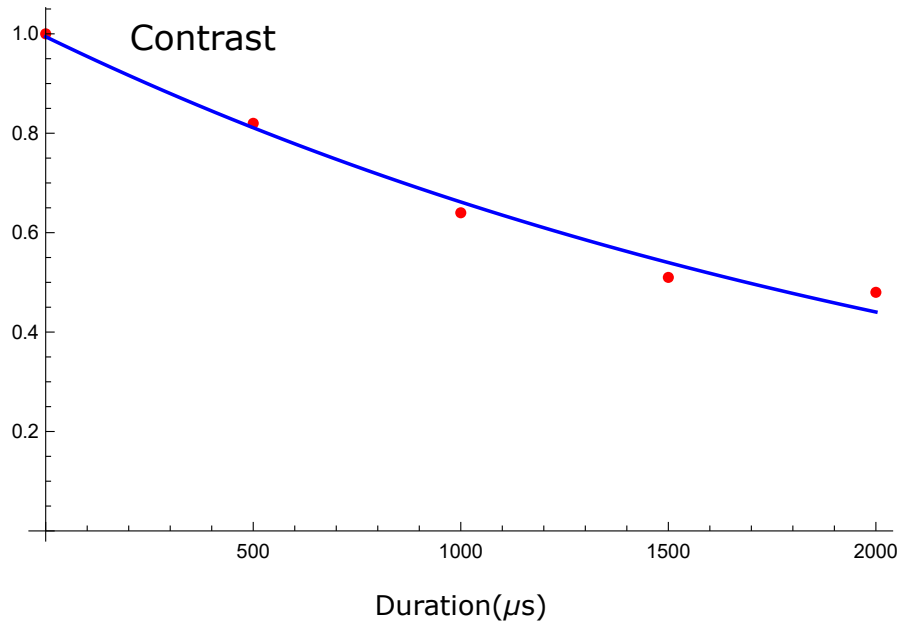
图 3.29 Ramsey-type measurement of the superposition state $(|0\rangle + |1\rangle)\,|\uparrow\rangle$. We extract the contrast that decay to $1/e$ as the coherence time τ with the fitting function $A * Exp(-t/\tau)$.

第4章　Reconstruction of the Jaynes-Cummings field state

4.1　Introduction

Reconstructing the state of a quantum system through measurements reveals all the statistical properties of the system. Thus schemes to reconstruct a quantum state are useful, for example, to ensure the quantum state generated and to test the fidelity of quantum operations. The quantum state is equivalently represented by its density matrices or quasiprobability functions in phase space[29]. Among the quasiprobability functions, the Wigner function has been used mainly for the study of non-classicality of the state, which is manifested by negativities[30]. The Q-function has been used to study the essence of the dynamics of a quantum-state evolution in phase space[11,31–39]. Recently, there have been many developments in reconstructing the state of a quantum field in various physical systems including photonic systems[40,41], atomic systems[42], molecular systems[43], trapped ion systems[44–47], cavity-QED[48] and circuit-QED systems[49,50], which are mostly related to the reconstruction of Wigner functions by the parity measurements of the states.

The Q-function requires only the measurement of the vacuum component of the field, which looks relatively easy to implement. The reconstruction of the Q-function also does not require a heavy numerical process as the probability of the state being in the vacuum is the value of the Q-function in each point of phase space. However, the measurement of the vacuum state is not straightforward. In a cavity, as an example, the existence of a photon can be detected by an atomic state through an atom-photon interaction like Jaynes-Cummings model (JCM)[3]. If the cavity has no photons, an atom initially prepared in its ground state will remain there forever. However, by merely measuring the atom in its ground state we cannot say that the cavity is empty because the Rabi oscillations periodically bring the atom back to the ground state even with many photons in the cavity. The oscillation frequency depends on how many photons are present in the cavity. The authors in Refs.[11,36,37] demonstrated a scheme of vacuum measurement that works for their particular cavity-QED system. For the circuit-QED system[39], a measurement of the vacuum component and the Q-function reconstruction was demonstrated based on the system-specific strong-nonlinear coupling between the cavity mode and the artificial atom. Recently a generic scheme of the vacuum measurement was proposed for the cavity-QED system with the standard JCM coupling[51].

While it is desirable to find the Q-function and the Wigner function based on one set of measurement, this has not been achieved due to the measurement inefficiencies of the vacuum state. Here, we report a generic and efficient detection of vacuum with $98.5(\pm0.3)\%$ efficiency for the phononic states in the vibrational mode of a harmonic trap, which is realized by the adiabatic passage schemes[52–54] based on counter-diabatic methods[55–57]. The demonstrated adiabatic passages have been significantly improved in order to measure the vacuum component of a reasonably large phonon state up to $\langle n \rangle \sim 25$ phonons. Typically, in trapped ion systems, phonon number distributions are measured by the Fourier transformation of the phonon-number dependent Rabi oscillations[58–60]. For this, a long observation time is necessary. Our scheme does not require such a long observation time, but at each measurement, we obtain a binary result; the vacuum or the complementary states. We simply need to repeat the measurement sequence for the probabilities of the vacuum state, which by nature of the measurement excludes the negativity problem of the Q-function shown in Ref.[39]. We efficiently measure the vacuum probabilities in phase space to observe the dynamics of the JCM field. The measured Q-function is highly accurate, which enables us to reconstruct the density matrix and the Wigner function by its deconvolution. We show a good agreement of our quasiprobabilities with the theoretical predictions.

The JCM is one of the most fundamental interaction models in quantum mechanics[3], where a single two-level atom resonantly interacts with a single-mode field. The JCM has enabled theoretical and experimental investigations of the basic properties of quantum electrodynamics such as Rabi oscillations of the energy transfer between the two subsystems and collapses and revivals of the oscillations[61]. More recently, the model has been widely studied for its rich properties of quantum control, coherent superposition and entanglement which are closely related to the current development of quantum technology. In order to see the nonclassical effects due to quantum interaction, the JCM is often studied with the state initially prepared in a coherent field and the atom in its energy eigenstate. It has been shown that the field and the atom are entangled[31] as soon as the interaction starts, but at a certain time they are nearly disentangled to bring the field into a superposition of two coherent states of a π phase difference[32,33]. Earlier, Eiselt and Risken[34,35] showed that the Gaussian probability distribution of the initial coherent state in phase space breathe at the initial points of interaction, reflecting the Rabi oscillations. Then the Gaussian peak bifurcates to travel around a circle in opposite direction in phase
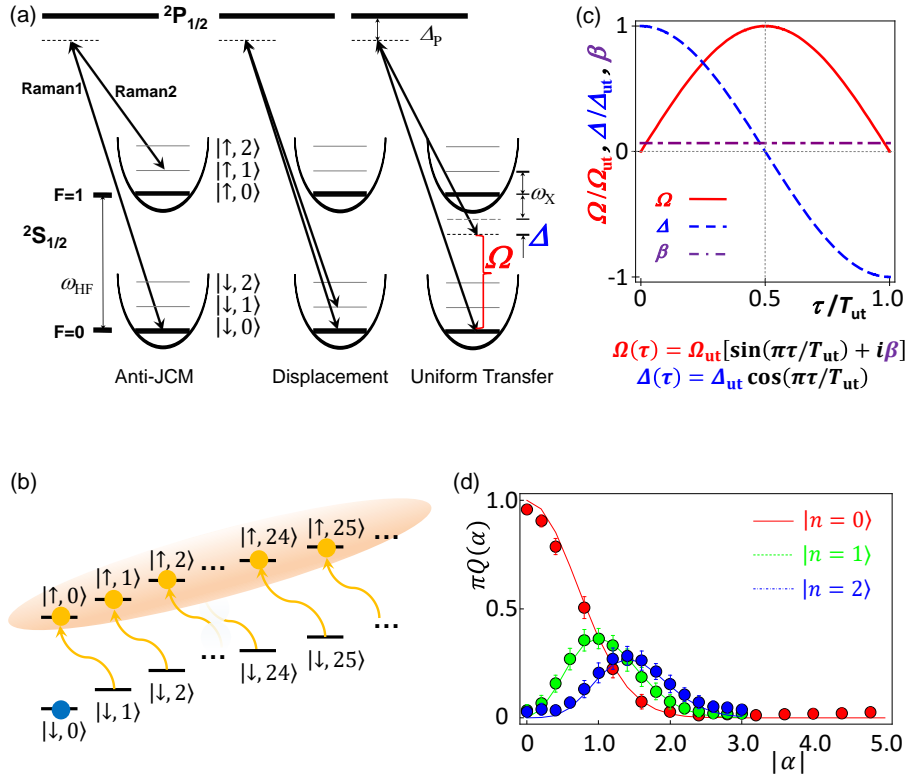
图 4.1　Raman laser schemes and the vacuum measurement. (a) The Hilbert space of the system is comprised of the direct product of qubit states $\{|\downarrow\rangle, |\uparrow\rangle\}$ and phonon number states $\{|n = 0\rangle, |1\rangle, |2\rangle, ...\}$. Raman laser beams, which have σ_- polarization and are detuned by $\Delta_p \approx$ 12.9 THz from the $P_{1/2}$ manifold, perform anti-JCM, displacement operation and the vacuum measurement by adjusting their beating frequencies. (b) The vacuum component is measured by transferring the population of $|\downarrow, n\rangle$ to that of $|\uparrow, n-1\rangle$ for any value of n at the same duration of pulse. The atom remaining in no fluorescence state $|\downarrow\rangle$ indicates the phononic state being in $|0\rangle$. (c) The uniform transfer for any phononic state $|n\rangle$ to $|n-1\rangle$ is accomplished by the scheme of shortcuts to the adiabaticity, where $\Omega_{ut} = (2\pi)22.7$ kHz, $\beta = 0.075$, $\Delta_{ut} = 1.9\Omega_{ut}$ and the total duration $T_{ut} = 198.2\mu s$. (d) Q-function of the phononic Fock state $n = 0, 1, 2$ depending on the amount of displacement $|\alpha|$. The points with error bars are the experimental results while the dashed lines are by the theory. The error bars are obtained by the standard deviation of the quantum projection noise with 100 repetitions.

space. The bifurcation is a consequence of quantum nature of interaction and was experimentally probed through the measurement of field phase distribution[36,37]. However, the full reconstruction of the dynamics of the JCM field has not been experimentally demonstrated.

We realize the JCM or anti-JCM by applying a pair of counter-propagating Raman beams that have the frequency differences of $(\omega_{R1} - \omega_{R2}) = \omega_{HF} \mp \omega_X$, respectively, as shown in Fig. 4.1(a). In the interaction picture, the Raman laser interactions can be

described by the following JCM and anti-JCM Hamiltonians

$$\hat{H}_{\mathrm{JC}}(\phi) = \frac{\hbar\eta\Omega}{2}\left(\hat{a}\hat{\sigma}_+ e^{i\phi} + \hat{a}^\dagger\hat{\sigma}_- e^{-i\phi}\right),$$

$$\hat{H}_{\mathrm{aJC}}(\phi) = \frac{\hbar\eta\Omega}{2}\left(\hat{a}^\dagger\hat{\sigma}_+ e^{i\phi} + \hat{a}\hat{\sigma}_- e^{-i\phi}\right). \tag{4-1}$$

Here, $\hat{a}^\dagger$ and $\hat{a}$ are the phonon creation and annihilation operators, $\hat{\sigma}_+ (\hat{\sigma}_-) = |{\uparrow}\rangle\langle{\downarrow}| (|{\downarrow}\rangle\langle{\uparrow}|)$ the spin-raising (lowering) operator, Ω the vacuum Rabi frequency of (anti-)JCM and $\eta = \Delta k\sqrt{\hbar/m\omega_{\mathrm{X}}}$ the Lamb-Dicke parameter with Δk the net wave-vector of the Raman laser beams, m the mass of the $^{171}\mathrm{Yb}^+$ ion and ϕ the phase difference of the Raman laser beams. The JCM and anti-JCM dynamics share more or less the same behavior. For technical reasons, we perform experiments for the anti-JCM interaction.

4.2　Efficient vacuum measurement

The essence of the vacuum-component measurement is in the realization of the uniform population transfer of $|{\downarrow}, n\rangle \rightarrow |{\uparrow}, n-1\rangle$ for any n as shown in Fig. 4.1(b). After the uniform transfer, all the phonon states except the vacuum component $|n = 0\rangle$ are in the bright electronic state $|{\uparrow}\rangle$, which emits photons during the standard fluorescence detection sequence. Therefore, the atom being in the dark electronic state $|{\downarrow}\rangle$ after the uniform transfer indicates the phonon state in the vacuum. By measuring the vacuum probability of the state after displacing it by α, we can directly measure the Q-function $Q(\alpha)$. The Q-function allows to study the core of the dynamics of a quantum state in phase space and has well been a preferred choice of study theoretically[31–35] and experimentally[11,36–39]. The definition of the Q-function is $Q(\alpha) = \frac{1}{\pi}\langle 0|\hat{D}^\dagger(\alpha)\hat{\rho}\hat{D}(\alpha)|0\rangle$, where $\hat{D}(\alpha)$ is the displacement operator[62]; the value of the Q-function is merely the weight of the vacuum component of a given state once it is displaced in phase space.

In general, the frequency of the Rabi oscillations between $|{\downarrow}, n\rangle$ and $|{\uparrow}, n-1\rangle$ has $\sqrt{n}$ dependency due to the nature of JCM coupling. To accomplish the uniform transfer, we basically apply an adiabatic passage, but in much shorter time than what is required for the adiabatic evolution; the so-called shortcuts to adiabaticity[53–57]. Here, as shown in Fig. 4.1(c), the detuning $\Delta \equiv (\omega_{\mathrm{R1}} - \omega_{\mathrm{R2}}) - (\omega_{\mathrm{HF}} - \omega_{\mathrm{X}})$ and the amplitude Ω of Raman laser beams are swept by $\Delta(t) = \Delta_{\mathrm{ut}}\cos(\pi t/T_{\mathrm{ut}})$ and $\Omega(t) = \Omega_{\mathrm{ut}}[\sin(\pi t/T_{\mathrm{ut}}) + i\beta]$, where $i\beta$ is the counter-diabatic field that is applied at a constant amplitude with a 90 degree out of phase with the driving field to suppress excitations during the fast evolution[53–57].

Note the idea behind this uniform red sideband is transition-less driving. When the driving speed is not infinitesimal, despite the energy eigen-Hamiltonian we get more terms. The diagonal terms will contribute to the famous Berry phase, while the non-diagonal terms will introduce extra non-adiabatic transitions. To suppress this excitation, we can add an auxiliary field called the counter-diabatic Hamiltonian with an opposite sign with the non-diagonal terms to cancel them out in the σ_y direction, which is shown in the formula with sign i. The derivation of this counter-diabatic Hamiltonian has used the reverse engineering[56]. In reality, when we slow the speed, its influence is also reduced, therefore in experiments we give a average value β to optimal the whole process.

As in this experiment, we employ the uniform red sideband transition, which can move all the phonon from $|\downarrow, n = 1\rangle$ to $|\downarrow, n = nmax\rangle$ to the spin up simultaneously. By measuring the spin up state's total population $p_\uparrow(total)$, and we thus get $p(0) = 1 - p_\uparrow(total)$ directly. Note in experiment when we vary the amplitude, we have to compensate the AC stark shift, which mainly comes from the off-resonant coupling of the carrier transition. In this experiments, $\Delta Car = \frac{\Omega_0^2}{2\omega_x\eta^2} \sim 21$ kHz, where $\Omega_0 \sim 22$KHz, the Lamb Dicke parameter $\eta = 0.089$. The AC stark shift is written as $\frac{|\Omega(t)|^2}{2\Delta}$, and the real red sideband frequency can be written as $\omega_{rsb}^{real} = \omega_{rsb}^{mea} + \frac{|\Omega(t)|^2}{2\Delta}$. We apply the time dependent pulse, whose waveform written as follows,

$$\Omega_0[\sin(\frac{\pi t}{T})\cos[\int_0^t (\omega_{rsb}^{real} + \Delta(t'))dt] - \beta\sin[\int_0^t (\omega_{rsb}^{real} + \Delta(t')), dt]], \qquad (4\text{-}2)$$

where

$$
\begin{aligned}
\int_0^t (\omega_{rsb}^{real} + \Delta(t'))dt &= \int_0^t (\omega_{rsb}^{mea} + \frac{|\Omega(t)|^2}{2\Delta} + \Delta(t'))dt \\
&= \omega_{rsb}^{mea}t + \Delta_0\frac{T}{\pi}\sin(\frac{\pi t}{T}) + \frac{\Omega_0^2}{2\Delta_r}\int_0^t (\frac{1}{2} - \frac{\cos(\frac{2\pi t}{T})}{2} + \beta^2)dt \\
&= \omega_{rsb}^{mea}t + \Delta_0\frac{T}{\pi}\sin(\frac{\pi t}{T}) + \frac{\Omega_0^2}{4\Delta_r}[(1 + 2\beta^2)t - \frac{T}{2\pi}\sin(\frac{2\pi t}{T})]. \qquad (4\text{-}3)
\end{aligned}
$$

We evaluate the reliability of the uniform transfer by performing the Q-function measurements for the phonon number states $|n = 0, 1, 2\rangle$ as shown in Fig. 4.1(d). Here, we prepare the phonon number states $|n = 0, 1, 2\rangle$ and displace them along one direction in phase space. We note that we do not observe serious imperfection over the quantum projection noise.

4.3　Trace of the internal states

Before measuring the field state, we trace over the internal (qubit) degree of freedom by the standard optical pumping technique, which transfers the population of $|\uparrow\rangle$ state to $|\downarrow\rangle$ state through the scattering of a few photons. A phonon number state is changed by a factor of $\sqrt{n_{ph}}\left(1-e^{-\eta^{2\Delta n}}\right)$ by n_{ph} photon scattering, where Δn is the phonon number difference. In our experimental condition, the probability of phonon number change by one is around three percentage through 10-photon scattering.

We experimentally study the modification of the phonon number distribution by optical pumping sequence as follows. First, we prepare a coherent state in $|\downarrow\rangle$ and measure the phonon number distribution by observing the oscillations of $P(|\uparrow\rangle)(t)$ after applying the blue-sideband transition. Then we prepare the same coherent state in $|\uparrow\rangle$ and apply the optical pumping to bring it to $|\downarrow\rangle$ state, and measure the phonon number distributions. Besides, we also employ the vacuum measurement method to study this effects. For both cases, We do not observe a significant change in the phonon number distribution Fig. 4.2
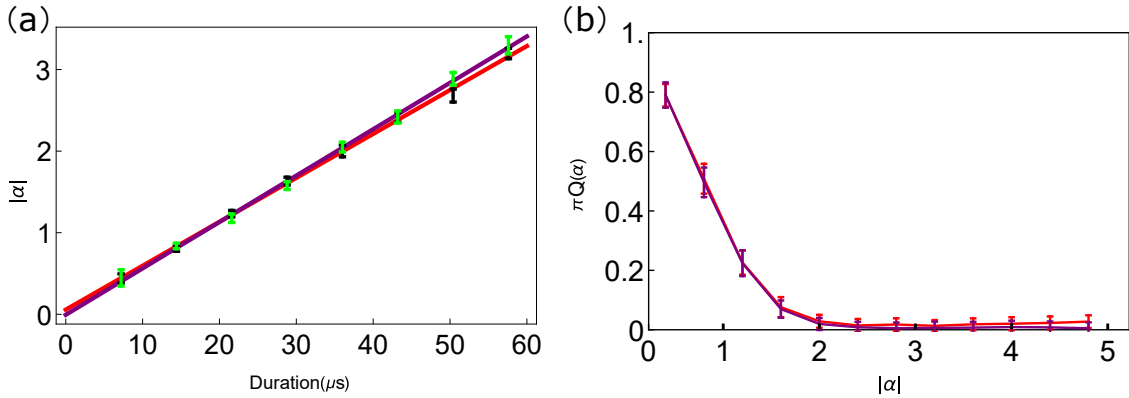
图 4.2　Test the influence of optical pumping sequence to the phonon number distribution. (a) The coherent states prepared in $|\downarrow\rangle$ state (red circles) are compared with those prepared in $|\uparrow\rangle$ state by an optical pumping pulse (blue circles). (b) The vacuum part of the coherent states prepared in $|\downarrow\rangle$ state (red circles) are compared with those prepared in $|\uparrow\rangle$ state by an optical pumping pulse (blue circles). Here we have used the vacuum measurement method. For both cases, the amount of the displacement $|\alpha|$ is measured by coherent-state fitting to the phonon number distribution.

4.4 JCM dynamics

It was found that the atom and the field in the JCM or anti-JCM are nearly disentangled during the course of interaction if the atom is initially prepared in a superposition of $|\uparrow\rangle$ and $|\downarrow\rangle$ and the field is initially in the coherent state $|\alpha\rangle$ of its amplitude α with $|\alpha| \gg 1$. Let us consider the initial state of the atom $|\Psi_A^\pm\rangle = (|\uparrow\rangle \mp i |\downarrow\rangle)/\sqrt{2}$. By the interaction (4-1), the atom-field state evolves to $|\Psi_{A-P}^\pm(t)\rangle = |\Psi_P^\pm(t)\rangle \otimes |\Psi_A^\pm(t)\rangle$ [63], where

$$|\Psi_A^\pm(t)\rangle = \left(e^{\pm i\pi t/t_{\text{rev}}} |\downarrow\rangle \mp i |\uparrow\rangle\right)/\sqrt{2}, \tag{4-4}$$

$$|\Psi_P^\pm(t)\rangle = \exp\left(\mp it\frac{\eta\Omega\sqrt{\hat{n}}}{2}\right)|\alpha e^{\pm i\pi t/t_{\text{rev}}}\rangle. \tag{4-5}$$

From this, it is clear that if the atom is prepared in its ground state $|\downarrow\rangle$ $\left[= \left(|\Psi_A^-\rangle - |\Psi_A^+\rangle\right)/\sqrt{2}i\right]$, the atom-phonon state will be in the superposition of $|\Psi_{A-P}^\pm(t)\rangle$. The phonon state will rotate in phase space, where $t_{\text{rev}} = \frac{4\pi|\alpha|}{\eta\Omega}$ is the corresponding revival time.

In the experiment, we prepare a coherent state of $\beta = 1.62(0.05)$ with the internal state $|\downarrow\rangle$ by displacing the $|n = 0\rangle$ state after the standard Raman-sideband ground-state cooling as we mentioned in Chapter 3. Then we apply Raman laser beams for the anti-JCM interaction and observe the dynamics of the atom and the field. For the internal state of the atom, we measure the probability of being in the $|\uparrow\rangle$ state, $P(|\uparrow\rangle)$ by the standard fluorescence detection scheme. For the field, we choose five different interaction times $t = (0, \frac{1}{4}, \frac{1}{2}, \frac{3}{4}, 1) t_{\text{rev}}$ in the anti-JCM. After the interaction time t, we displace the state by α and trace over the internal degree of freedom by the standard optical pumping sequence, which does not produce any noticeable change of the phonon distribution. Then we measure the vacuum component to reconstruct $Q(\alpha)$.

Figs. 4.3(b) and (c) show the experimental and theoretical time evolution of the initial coherent state under the anti-JCM interaction. The theoretical results are obtained by the numerical simulation of the master equation of anti-JCM Hamiltonian including experimental imperfections [53]. At $t = 0$, $P(|\uparrow\rangle) = 0$ and $Q(\alpha)$ is Gaussian, which represents the coherent state. At time $t = t_{\text{rev}}/4$, while the Rabi oscillations begin to collapse, the Gaussian peak splits into two, which can be understood by the separation of two atom-phonon states $|\Psi_{A-P}^\pm\rangle$. The two components of the atom-phonon entangled state evolve in the opposite phases as shown in Eqs. (4-4) and (4-5). At the half revival time $t = t_{\text{rev}}/2$, the two atomic states in Eq. (4-4) become identical except the global phase,
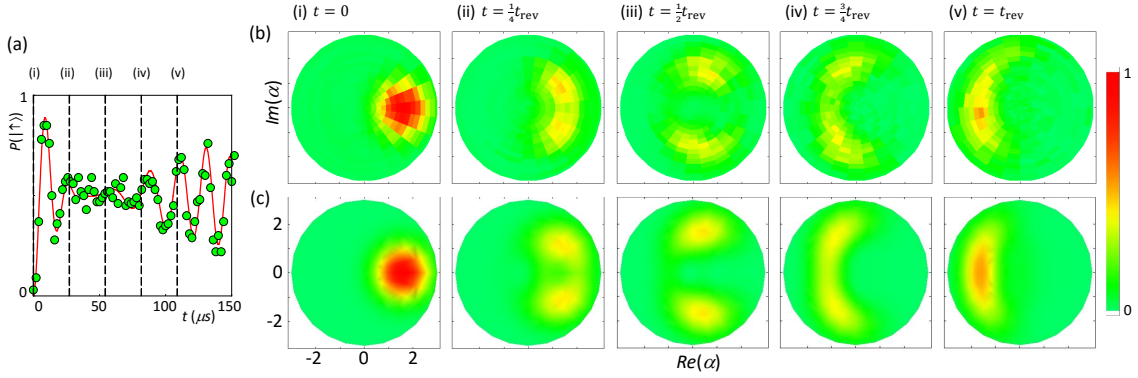
图 4.3 The time evolution of the Q-function for an initial coherent state under anti-JCM interaction. (a) Collapse and revival of the Rabi oscillation signal, (b) experimentally measured and (c) numerically calculated Q-functions of the phonon field with the initial coherent state $|\beta = 1.62(0.05)\rangle$ depending on the duration of anti-JCM interaction. (a) $P(|\uparrow\rangle)$ is the probability of detecting the atom in $|\uparrow\rangle$. The points are obtained after 100 repetitions. The solid line is from fitting the data with $\sum_{n=0} \frac{1}{2}\left[1 - e^{-\gamma t} \cos\left(\sqrt{n+1}\eta\Omega t\right)\right]$, where γ is the empirical decay constant. At (b) and (c), the time for each snapshot of the Q-functions are labeled as (i)-(v) in the unit of the revival time t_{rev}, where $t_{\text{rev}} = \frac{4\pi|\alpha|}{\eta\Omega} = 108.8$ μs. In (b), each Q-function is obtained from 100 repetitions of the vacuum measurements after 384 different displacements, where the amplitude and the phase of displacement $|\alpha|e^{i\varphi}$ are scanned from 0 to 3.0 with the step size of 0.2 and from 0 to 2π with the 24 steps, respectively.

which results in disentanglement of the atomic state from the phonon state (see also Fig. 4.7). In the Q-function, the phonon state shows two clearly separated peaks that are located at the opposite phases in phase space. This can be understood as the superposition of two coherent states[63]. Further evolution of the phonon state is shown in Figs. 4.3(iv) and (v). At the revival time $t = t_{\text{rev}}$, the two phonon peaks merge at the opposite position of the initial coherent state, which causes the revival of the Rabi oscillations. Due to the quadratic phase term in Eq. (4-5), the amplitude of the Rabi oscillations is reduced.

Here we show that the relation between Rabi contrast, purity and atomic coherence as shown in Fig. 4.4. At the revival time $t_{\text{rev}} = \frac{4\pi|\alpha|}{\eta\Omega} = 108.8$ μs, the contrast of the Rabi oscillations does not seem to be maximum, as the largest contrast occurs around 130 μs. It is mainly caused by the relatively small initial coherent state $|\beta\rangle = 1.62(0.05)$, which has small frequencies of Rabi oscillations and the contrast cannot reveal the information of purity or coherence of the qubit states. According to our numerical simulation, however, the maximum purity or the largest atomic coherence (the off-diagonal part of the atomic density matrix) occurs near the revival time, 108.8 μs not around 130 μs.
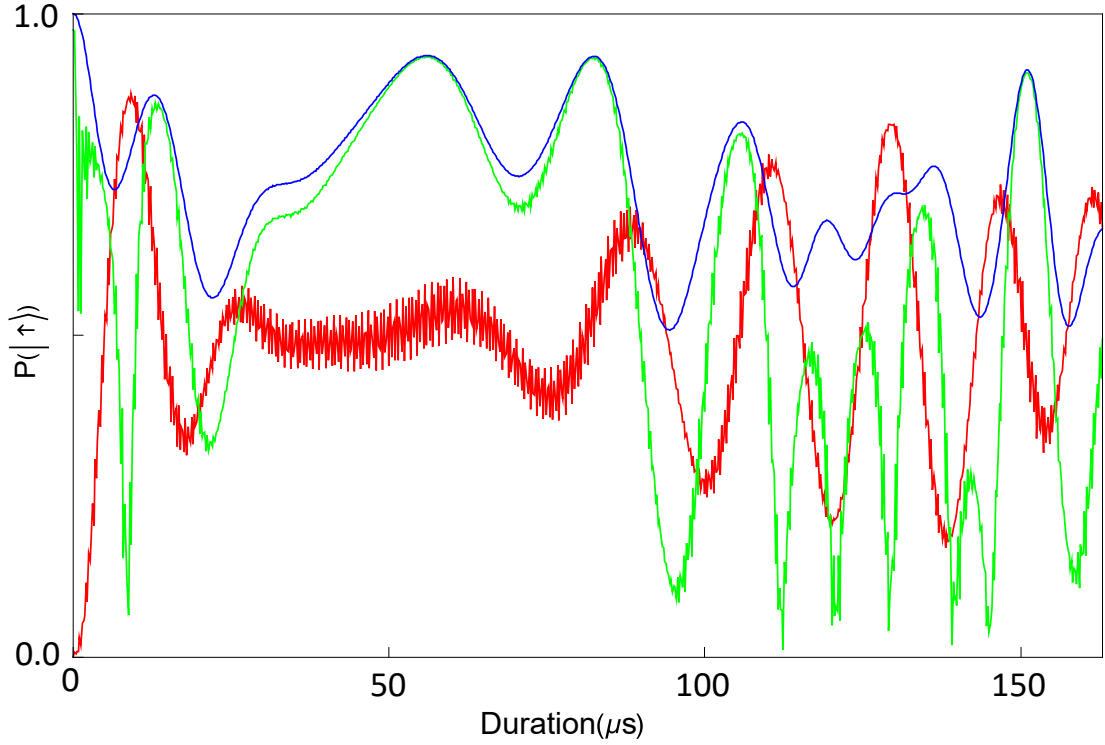
图 4.4   The relation between Rabi contrast, purity and atomic coherence. The red curve is the Rabi oscillation signal, the blue one is the the purity of the phononic state and the green one is the atomic coherence, the absolute value of the off-diagonal elements of the atomic density matrix after tracing over the phononic field state. All curves are obtained by the numerical calculations without the dissipation terms.

4.5   Coherence test: Time reverse process

In order to confirm the whole dynamics keeping coherence, we perform the time reversal operation, which forces the phonon state evolved under the anti-JCM interaction to retrace its past trajectory in the opposite direction by the generalized echo scheme[64]. For the echo method, we introduce a π phase shift in the second half of the anti-JCM interaction, $i.e.$, $\mathrm{e}^{-i\frac{t}{2\hbar}H_{\mathrm{aJC}}(\pi)} = \mathrm{e}^{+i\frac{t}{2\hbar}H_{\mathrm{aJC}}}$. The process is called time-reversal as in Ref.[65]. We apply the reverse process at the half revival time $t = t_{\mathrm{rev}}/2$ and observe that the state is brought back to the initial coherent state at the time $t = t_{\mathrm{rev}}$ with the fidelity of 0.914(4) through the Q-function measurement shown in Fig. 4.5. Since keeping the coherence of the interaction is at the heart of the time reversal, our result of time reversal clearly confirms that the process occurs in quantum regime.

We also study another way of reversing the anti-JCM by applying the JCM as shown in Fig. 4.6.[66]. These two have the similar results.
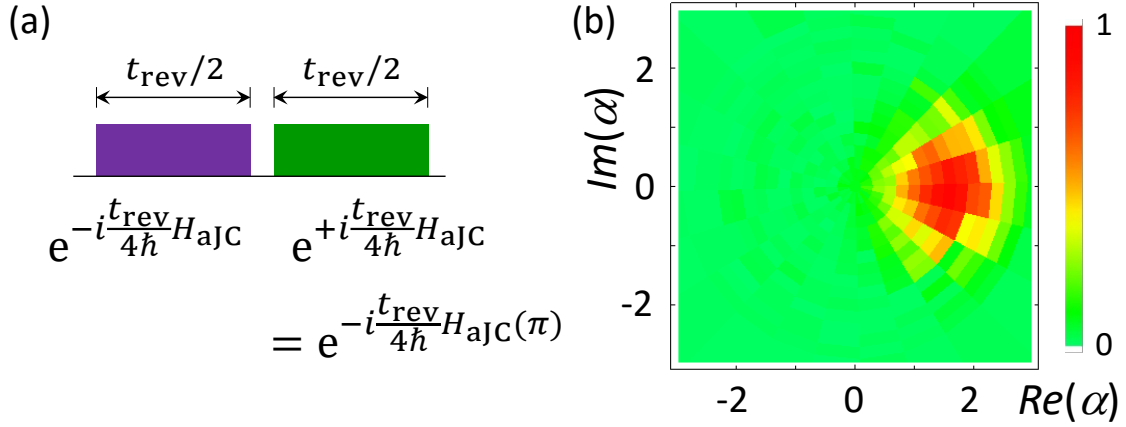
图 4.5 (a) Generalized echo-sequence time reversal of anti-JCM evolution for the interaction time $t = t_{\text{rev}}/2$. The $\phi = \pi$ phase of the anti-JCM Hamiltonian produces the negative sign; $H_{\text{aJC}}(\pi) = -H_{\text{aJC}}(0)$, which performs the time reversal operation. (b) The measured Q-function of the phononic state after time reversal operation of (a). The total number of measurements for the Q-function reconstruction is same as that in Fig. 4.3.

4.6 Direct reconstruction of density matrix from the Q-function

In addition to the time-reversal process, we demonstrate the coherence property by detecting non-classicality generated during the evolution, in particular, interferences of the composite states of the two peaks in phase space. For this purpose, we reconstruct the Wigner function from our measured Q-function.

The relation between the Q-function and the density matrix is describe as

$$
\begin{aligned}
Q(\alpha) & = \frac{1}{\pi} \langle \alpha | \rho | \alpha \rangle \\
& = \frac{1}{\pi} \sum_{n=0}^{n_{\max}} \sum_{m=0}^{n_{\max}} \langle \alpha | n \rangle \langle n | \rho | m \rangle \langle m | \alpha \rangle \\
& = \frac{e^{-|\alpha|^2} \alpha^m (\alpha^*)^n}{\pi \sqrt{m! n!}} \sum_{n=0}^{n_{\max}} \sum_{m=0}^{n_{\max}} \rho_{n,m},
\end{aligned} \tag{4-6}
$$

where $n_{\max}$ is the maximum phonon number that we include for the reconstruction. With the sufficient number of measured values of Q-function over $n_{\max} \times n_{\max}$, we can inverse the multiple equations of Eq. (4-6) and reconstruct the density matrix elements. Mainly due to the quantum projection noise in the measurements, however, the direct inverse of the equations may result in unphysical results including the negativity of the diagonal components in the density matrix. In order to avoid the problem, we apply a method of convex optimization of least square function with constraints. Here we first define a
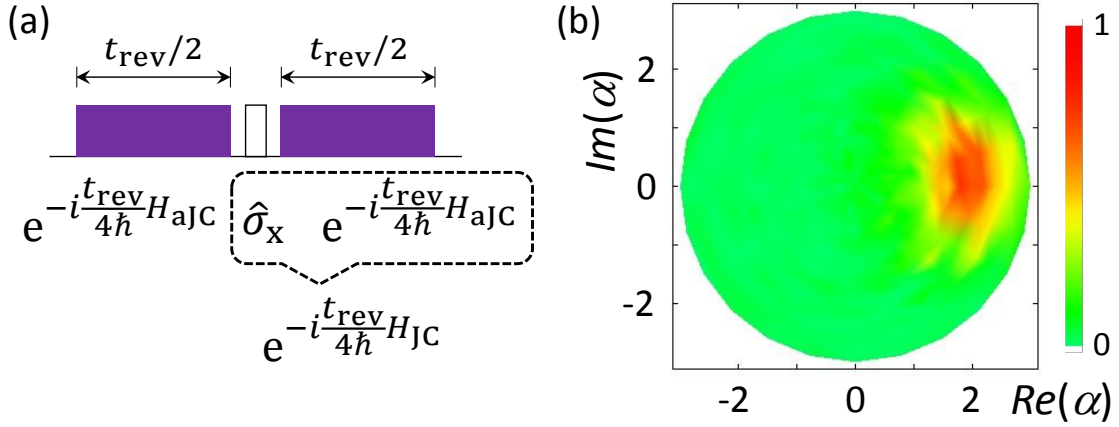
图 4.6　Time reversal of anti-JCM by JCM. (a) JCM sequence for the time reversal of anti-JCM evolution for the interaction time $t = t_{\text{rev}}/2$. The JCM coupling is realized by a σ_{x} pulse and the anti-JCM coupling. The phase $\frac{\pi}{2}$ of the second anti-JCM pulse is chosen to maximize the fidelity of the reverse operation. (b) Measured Q-function of the phononic state after the reversal operation. We realize the JCM interaction by applying the π-carrier pulse σ_{x} and anti-JCM pulse, which can be understood as $\text{e}^{-i\frac{t}{2\hbar}H_{\text{aJC}}}\sigma_{\text{x}} = \sigma_{\text{x}}\text{e}^{-i\frac{t}{2\hbar}H_{\text{JC}}}$. In experiment, we do not apply the additional σ_{x} pulse for convenience, since we trace out the internal degree of freedom. We note that the JCM reverse method provides relatively lower fidelity of the final state than that of the echo scheme since the JCM reverse works better as the initial coherent state becomes larger.

function F as follows.

$$F = \sum_{i=0}^{i_{\max}} |Q^{\text{exp}}(\alpha) - Q^{\text{rec}}(\alpha)|^2, \tag{4-7}$$

$$= \sum_{i=0}^{i_{\max}} \left| Q^{\text{exp}}(\alpha) - \frac{e^{-|\alpha|^2}\alpha^m(\alpha^*)^n}{\pi\sqrt{m!n!}} \sum_{n=0}^{n_{\max}} \sum_{m=0}^{n_{\max}} \rho_{n,m} \right|^2 \tag{4-8}$$

where $Q^{\text{exp}}(\alpha)$ and $Q^{\text{rec}}(\alpha)$ are the experimentally measured and the numerically reconstructed Q-functions, respectively, at α in phase space. Then we minimize the function F with the constraints of density matrix, which should be positive semi-definite of trace 1.

We first find the density matrix by deconvoluting the Q-function by the convex-optimization and reconstruct the Wigner function from the density matrix. Fig. 4.7(a), which is reconstructed from the experimental data of the Q-function measurement, clearly manifests interference patterns of the composite states at the half revival time and negativities in other interaction times. The experimental reconstruction of the Wigner function of Fig. 4.7(a) is in good agreement with the direct theoretical reconstruction of the Wigner function shown in Fig. 4.7(b). We also obtain the purities $\text{Tr}\left(\rho^2\right)$ of the states from the

66

experimentally reconstructed density matrix. At $t = t_{rev}/2$, the purity is $0.82(0.05)$, which indicates the phonon state is not entirely pure, possibly because of its entanglement with the internal state. Theoretical studies[32] suggest that the purity reaches ideally at unity as the size of initial coherent state increases.

4.7 Conclusion

We have shown a highly efficient scheme to detect the vacuum which is used to reconstruct the dynamics of the JCM field for the first time. In our experimental demonstration, the size of the initial coherent state $|\beta\rangle$ could be increased by improving our ion trap system in which way the approximated analytical theory can be better compared with experimental data. The main current limitation comes from the unreliable displacement operation for a large scale above $\alpha \approx 4.8$, which is caused by the heating of the phonon mode. The reduction of an order of magnitude in the heating rate would allow us to reach an order of magnitude large phonon number state. Our developed technique of Q-function measurement can be performed in a single detection and used to probe many other dynamics of the phonon field. Our approach is generic and would also be applied to other physical platforms including opto-mechanics and cavity QED system.
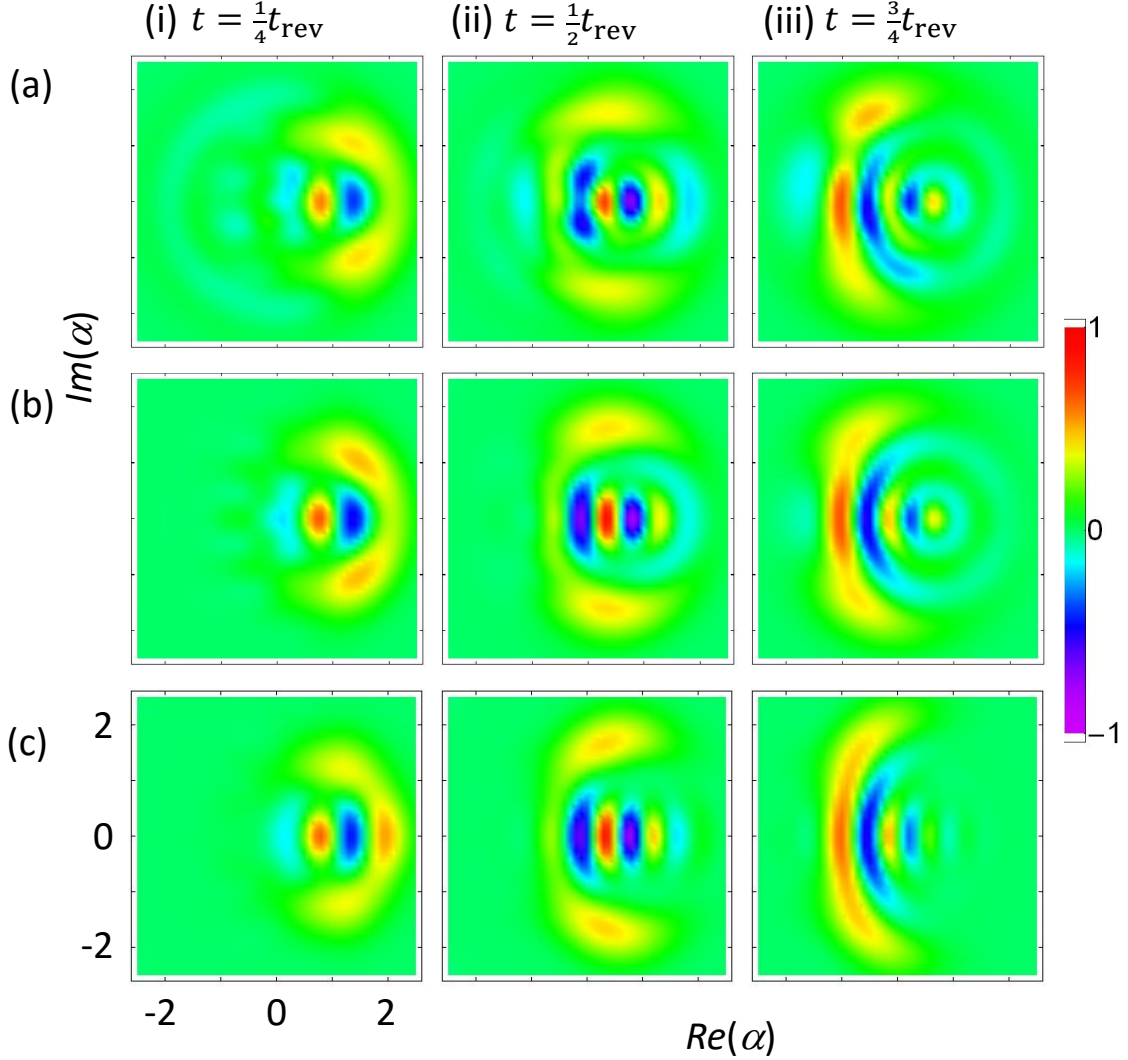
图 4.7 The Wigner function reconstruction from the Q-function at various times of the anti-JCM evolution, $t = \frac{1}{4}, \frac{1}{2}, \frac{3}{4} t_{\text{rev}}$. The negativities of the Wigner functions indicate the emergence of nonclassical state during the dynamic evolution. (a) The Wigner functions are reconstructed from the density matrix obtained by deconvoluting the experimentally measured values of the Q-functions shown in Fig. 4.3(b). The density matrices are reconstructed by deconvoluting the Q-functions with the convex-optimization. We note that we use the data $|\alpha| \leq 1$ for the optimum fidelity and it is necessary to use proper initial guess of the density matrix for the convergence of the deconvolution. (b) The Wigner functions are directly obtained by the numerical calculation of the anti-JCM dynamics.

第5章　Quantum simulation of the quantum Rabi model

5.1　Introduction

The interaction between light and matter is one of the most fundamental and ubiquitous physical processes. The semi-classical Rabi model was proposed in 1936 to analyze the effect of a varying, weak magnetic field on an oriented atom possessing nuclear spin[2]. It describes the dipolar interaction between a classical monochromatic field and a two-level system, successfully explaining the challenging experimental data in Ref.[67]. When the field is promoted to a quantum description, resulting in the simplest fully-quantum model of light-matter interaction, it is called the quantum Rabi model (QRM). Typically, the coupling strength in a light-matter system is much lower than the field frequency. In this scenario, the QRM can be simplified to the Jaynes-Cummings model (JCM) under the rotating-wave approximation (RWA)[3]. The JCM is an analytically solvable model that has been studied in cavity quantum electrodynamics(CQED)[11,68,69], atomic physics[70], quantum dots[71], circuit quantum electrodynamics (cQED)[72,73] and trapped ions[58–60,74], among other quantum platforms. Recent experimental achievements have shown the accessibility to the ultrastrong coupling (USC) regime[75] or even to the deep strong coupling (DSC) regime[76,77], where the coupling strength is comparable to or larger than the mode frequency. In these strong-coupling regimes, the RWA breaks down, rendering the JCM as a restricted description of the system, and requiring the use of the full QRM to correctly describe the emerging physical phenomena[78]. It is noteworthy to mention that, in such regimes, exotic dynamical properties of light-matter interaction[79] and potential applications to quantum information technologies[80] have been predicted and proposed.

The Hamiltonian associated with the QRM can be expressed as ($\hbar = 1$)

$$\hat{H}_{QRM} = \frac{\omega_0}{2}\hat{\sigma}_z + \omega_m\hat{a}^\dagger\hat{a} + g(\hat{\sigma}_+ + \hat{\sigma}_-)(\hat{a} + \hat{a}^\dagger), \tag{5-1}$$

where $\hat{a}^\dagger(\hat{a})$ is the creation (annihilation) operator in the Fock space of a bosonic mode with frequency ω_m, and $\hat{\sigma}_+ (\hat{\sigma}_-) = |\uparrow\rangle\langle\downarrow| (|\downarrow\rangle\langle\uparrow|)$ and $\hat{\sigma}_z = |\uparrow\rangle\langle\uparrow| - |\downarrow\rangle\langle\downarrow|$ are the raising (lowering) and the Pauli z-basis operators, respectively, of a two-level system, an effective spin with energy splitting ω_0, and g is the coupling strength. Three major coupling regimes are defined depending on the ratio between the coupling strength g and the field mode

frequency ω_m, namely, the weak coupling or Jaynes-Cummings regime, with $g/\omega_m \ll 0.1$, the USC regime with $0.1 \lesssim g/\omega_m$, and the DSC regime with $1 \lesssim g/\omega_m$. In the Jaynes-Cummings regime, co-rotating terms $\hat{a}\hat{\sigma}_+$ and $\hat{a}^\dagger\hat{\sigma}_-$ dominate in Hamiltonian (5-1). In other words, the RWA is valid and the QRM reduces to the JCM, of which the whole Hilbert space consists of a series of independent two-fold subspaces $\{|\uparrow,n\rangle, |\downarrow,n+1\rangle\}$, where n is the quantum number of Fock state $|n\rangle$. In the USC/DSC regimes, however, the counter-rotating terms $\hat{a}\hat{\sigma}_-$ and $\hat{a}^\dagger\hat{\sigma}_+$ cannot be neglected. These two terms connect different two-fold subspaces, break the simple structure of the JCM and do not preserve the number of excitations. These excitation-nonconserving terms make it difficult to find an analytical solution of the QRM, which was found only recently[81]. Although the total excitation number is not conserved, it has been pointed out that the parity operator $\hat{\Pi} = \sigma_z e^{-i\pi\hat{a}^\dagger\hat{a}}$, with eigenvalues ± 1, is still a conserved quantity. The Fock space can be divided in two parts, each spanned by states of a given parity. The notion of parity chain was introduced in[79] to address the set of states $|\downarrow(\uparrow),n\rangle$ with the same parity ordered in ascending n. It is known that wave packets in the Fock space evolve within the same parity chains when in the USC/DSC regimes[79]. Recently, it has also been predicted that the ground states of the QRM in the USC/DSC regimes reveals the conservation of parity and the entanglement between spin and mode with large excitation numbers[82–85].

In the last years, experimental efforts have been made to reach the DSC regime[76,77], which stimulates the study of exotic physics of the QRM in the USC/DSC regimes. The phenomenon of photon number wave packets bouncing back and forth along the parity chains[79] has been observed in a classical simulator of a photonic waveguide system[86] and in analogue and digital quantum simulations in cQED systems[87,88]. However, the study of the ground state in DSC regime is still an open challenge[82].

In this work, we report the analog quantum simulation of the quantum Rabi model with a single trapped ion for all relevant coupling regimes. Among the results, we generate and observe the ground state of the QRM in the DSC regime in a trapped-ion quantum simulator for the first time. We demonstrate the full controllability and tunability of the QRM in a single trapped-ion system as proposed in Ref.[82], which enable us to generate the exotic ground state in the DSC regime by the adiabatic transfer from the simple ground state of the JCM. Moreover, we apply the capability of the ground state preparation to experimentally measure the energy spectrum of the QRM Hamiltonian (4-1). The total Hamiltonian of the system is composed of the uncoupled Hamiltonian and

the ion-laser interaction. The uncoupled Hamiltonian describing such a system is given by $\hat{H}_0 = \frac{\omega_{HF}}{2}\hat{\sigma}_z + \omega_X \hat{a}^\dagger \hat{a}$. When a pair of counterpropagating Raman laser beams is driven onto the ion, the ion-laser interaction is described by

$$\hat{H}_{\text{ion-laser}} = \hbar\Omega_{b,r} \cos\left(k_{b,r}\hat{x} - \omega_{b,r}t + \phi_{b,r}\right) \hat{\sigma}_x. \tag{5-2}$$

Here, $\Omega_{b,r}$ is the Rabi strength proportional to the product of both laser field amplitudes for blue-sideband or red-sideband transitions, $\Delta k_{b,r}$ is the net wave vector component of the Raman laser beams on the direction of the motion of the ion $\hat{x} = x_0(\hat{a} + \hat{a}^\dagger)$ is the position operator of the ion, with ground-state wave-packet width $x_0 = \sqrt{\hbar/2M\omega_X}$, where M is the mass of the ^{171}Yb$^+$ ion, and $\omega_{b,r}$ and $\phi_{b,r}$ are the differences of frequencies and phases of the Raman laser beams, respectively[74].
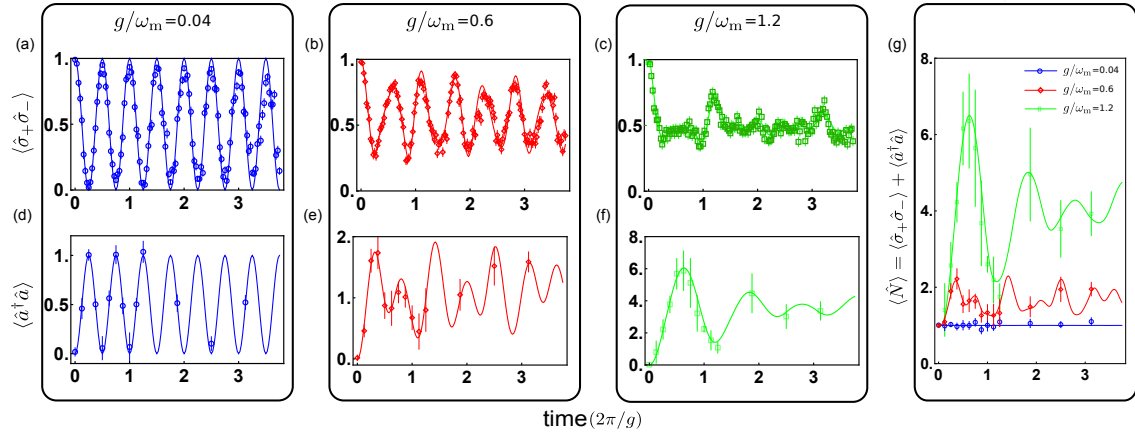
图 5.1　Spin and phonon dynamics under the QRM for different coupling regimes. (a, b, c) correspond to the population of the excited state of the two-level system for the coupling ratios $g/\omega_m = 0.04, 0.6,$ and 1.2, respectively. (d, e, f) correspond to the evolution of the average number of phonons for the same coupling ratios. Finally, (g) shows the evolution of the total number of excitations for the three cases considered above. In all panels, theoretical predictions are plotted with continuous lines, while dots and their associated error bars represent the experimental data. The lower number of points in the plots of $\langle a^\dagger a \rangle$ is because their measurement process (described in Methods C) is more time consuming.

Under suitable optical and vibronic RWAs, and also in the Lamb-Dicke regime, the ion-laser interaction can be turned into a(n) (anti-)Jaynes-Cummings interaction by tuning the laser frequency close to the red(blue)-sideband as $\omega_r = \omega_{HF} - \omega_X - \delta_r$ ($\omega_b = \omega_{HF} + \omega_X - \delta_b$), with a small detuning $\delta_{r(b)} \ll \omega_X$ in the most general case. Red-sideband and blue-sideband interactions are described in the interaction picture with

respect to the uncoupled Hamiltonian $\hat{H}_0 = \frac{\omega_{\text{HF}}}{2}\hat{\sigma}_z + \omega_{\text{X}}\hat{a}^\dagger\hat{a}$ by the Hamiltonians[53,74]

$$
\begin{aligned}
\hat{H}_{\text{red}}(t) &= \frac{\eta\Omega_{\text{r}}}{2}\left(\hat{a}\hat{\sigma}_+ e^{i\delta_r t} + \hat{a}^\dagger\hat{\sigma}_- e^{-i\delta_r t}\right), \\
\hat{H}_{\text{blue}}(t) &= \frac{\eta\Omega_{\text{b}}}{2}\left(\hat{a}^\dagger\hat{\sigma}_+ e^{i\delta_b t} + \hat{a}\hat{\sigma}_- e^{-i\delta_b t}\right).
\end{aligned}
\tag{5-3}
$$

Here, $\eta = \Delta k_{\text{b,r}} x_0$ is the Lamb-Dicke parameter.

When both red and blue sideband interactions are simultaneously applied with equal strength, such that $\Omega = \Omega_{\text{r}} = \Omega_{\text{b}}$, one can write the total Hamiltonian in the interaction picture as

$$
\hat{H}_{\text{br}}(t) = \frac{\eta\Omega}{2}\hat{\sigma}_+\left(\hat{a}e^{i\delta_r t} + \hat{a}^\dagger e^{i\delta_b t}\right) + \text{H.c.}.
\tag{5-4}
$$

Equation (5-4) corresponds to the interaction picture Hamiltonian with respect to the uncoupled Hamiltonian $\hat{H}_0' = \frac{\delta_b + \delta_r}{4}\hat{\sigma}_z + \frac{\delta_b - \delta_r}{2}\hat{a}^\dagger\hat{a}$ for the following effective Hamiltonian,

$$
\begin{aligned}
\hat{H}_{\text{eff}} &= \frac{(\delta_{\text{b}} + \delta_{\text{r}})}{4}\hat{\sigma}_z + \frac{(\delta_{\text{b}} - \delta_{\text{r}})}{2}\hat{a}^\dagger\hat{a} \\
&+ \frac{\eta\Omega}{2}(\hat{\sigma}_+ + \hat{\sigma}_-)(\hat{a} + \hat{a}^\dagger),
\end{aligned}
\tag{5-5}
$$

where the parameters of the simulated QRM can be associated with the experimental ones as $\omega_0 = \frac{\delta_b + \delta_r}{2}$, $\omega_{\text{m}} = \frac{\delta_b - \delta_r}{2}$ and $g = \frac{\eta\Omega}{2}$. Thus, such an experimental setup serves as a quantum simulator of the QRM, where one can simulate a wide range of coupling regimes by suitably tuning the laser intensities and detunings to match the desired ratio g/ω_{m}. It is important to point out that the observables of interest $\{\hat{a}^\dagger\hat{a}, \hat{\sigma}_z, |n\rangle\langle n|\}$, commute with all the adopted interaction-picture transformations, which are always with respect to a Hamiltonian of the form $\alpha\hat{a}^\dagger\hat{a} + \beta\hat{\sigma}_z$, such that their expectation values will remain unaltered in the laboratory reference frame[82].

Coupling regimes and breakdown of the RWA

For the experiment, we fix the coupling strength to $g = (2\pi)12.5$ kHz, and the detuning of the red sideband to $\delta_{\text{r}} = 0$, leaving δ_{b} as a tunable parameter. In this manner we will be simulating a resonant QRM where the ratio g/ω_{m} will be determined by the selected detuning δ_{b}. We experimentally explore three paradigmatic coupling regimes,

namely the Jaynes-Cummings, the USC and the DSC regimes, accordingly selecting the values of the detuning for the blue sideband as $\delta_b = 2\omega_m = (2\pi)\{625, 83.4, 41.6\}$ kHz, which correspond to the ratios $g/\omega_m = \{0.04, 0.6, 1.2\}$, respectively.

The experiment is carried out as follows. First, we perform standard Doppler and sideband cooling, which prepares the system in the state $|\downarrow, n = 0\rangle$ [6], and then, we transfer the system to the initial state $|\uparrow, n = 0\rangle$ by applying a carrier π pulse. After that, we turn on the red-sideband and blue-sideband transitions, with suitably chosen intensities and detunings, to implement the QRM Hamiltonian in the desired regime. We observe the dynamics of the QRM by measuring the average excitations of the spin $\langle \hat{\sigma}_+\hat{\sigma}_-\rangle$ and the phononic degrees of freedom $\langle \hat{a}^\dagger \hat{a}\rangle$ at specific evolution times t. We measure the average excitation of the spin $\langle \hat{\sigma}_+\hat{\sigma}_-\rangle$ by spin-dependent fluorescence detection, where only spin-$|\uparrow\rangle$ state scatters photons. We obtain the average excitation of phonons $\langle \hat{a}^\dagger \hat{a}\rangle$ from the measured phonon number distribution, which is deduced from fitting the blue-sideband signal to Eq. (5-8) in Methods C.

In Figs. 5.1(a) and (d), the measurements for the simulation of the Jaynes-Cummings regime are plotted. Rabi oscillations, with a complete collapse and posterior revival of the excitation probability of the two-level system are clearly observed. In the same manner, the average number of phonons in the bosonic mode oscillates between 0 and 1, consistent with the notion that the wavefunction of the system should live in the space spanned by the corresponding JCM doublet $\{|0, \uparrow\rangle, |1, \downarrow\rangle\}$, as expected for such a regime. Figures 5.1(b) and (e) show the evolution of the same initial state in the USC regime for the coupling ratio $g/\omega_m = 0.6$. In this case, collapses and revivals of the excitation probability are not complete and the average number of phonons exceeds 1, indicating that the dynamics does not anymore happen exclusively in the JCM doublet. This departure from the JCM physics is associated with the breakdown of the RWA due to the large coupling ratio. In the DSC regime, plotted in Figs. 5.1(c) and (f) for the coupling ratio $g/\omega_m = 1.2$, the effects of the RWA breakdown are even clearer, where not even oscillations can be identified and where the average number of phonons grows above 6 for the plotted example. We also show in Fig. 5.1(g) the evolution of the total excitation number $\langle \hat{N} \rangle = \langle |\uparrow\rangle \langle \uparrow| \rangle + \langle \hat{n} \rangle$, which is a conserved quantity when the RWA is valid, but has a dynamical behavior as soon as the RWA breaks down.
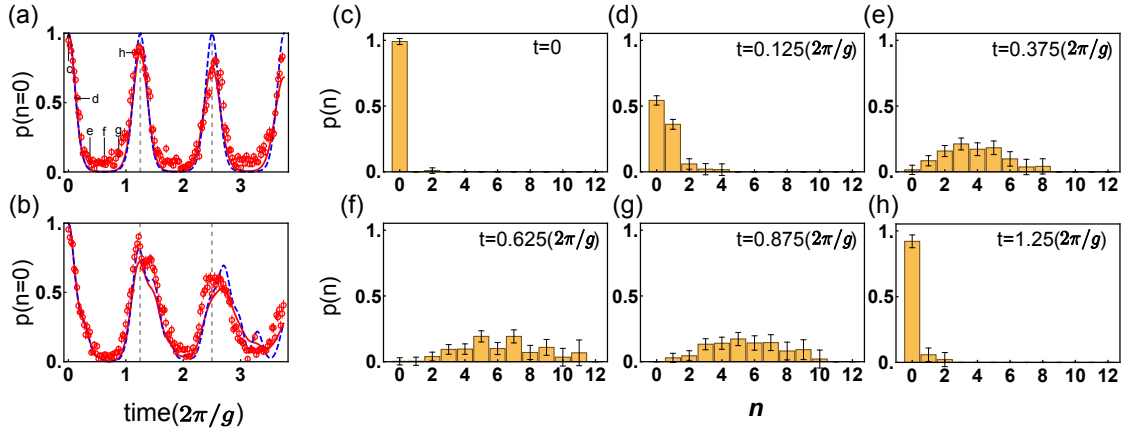
图 5.2 Phonon-number wave packets bouncing back and forth in the DSC regime. In (a) and (b) we plot the population of state $|n = 0\rangle$, after tracing out the spin, as the system evolves under the QRM in the DSC regime. In particular, (a) shows the degenerate case, $\omega_0 = 0$, and (b) the non-degenerate case, with $\omega_0 = 0.8g$. For both cases, the coupling ratio is fixed to $g/\omega_m = 1.25$. Dashed and solid lines represent theoretical calculations with and without decoherence of the motional mode, respectively. The vertical dashed lines indicate the motional revival times $k\frac{2\pi}{\omega_m}$, where $k = 1, 2, \ldots$. The data points with error bars correspond to the experimental results. We obtain the zero-phonon population following the method in Ref.[74] after tracing out the spin. (c-h) show the phonon number distribution sampled at several instants during one period $T = \frac{2\pi}{\omega_m} = 100\,\mu s$ of the QRM Hamiltonian for the degenerate case. The phonon distribution is obtained by fitting the standard blue-sideband signals to Eq. (5-8) after tracing out the spin (see Methods C). At the first revival time, the phonon state is back to the initial state as predicated by the QRM. The imperfections can be attributed to decoherence of the motional degrees of freedom.

5.2 DSC regime and phonon wavepackets

We focus now on the DSC regime and explore two scenarios, namely the degenerate case with $\omega_0 = 0$ and the non-degenerate case with $\omega_0 \neq 0$. In contrast to the weak coupling regime (JCM regime) of the natural light-matter interaction, in the USC/DSC regime the spin-field interaction can survive even when the spin is degenerate. Therefore, we expect to observe quantum dynamics due to the strong coupling effect. We note that the degenerate case has been investigated thoroughly for the production of Schrödinger's cat states [27,44,47,91,91–93] and the calibration of two-qubit Mølmer-Sørensen gates [94–99] in trapped ion systems. Although the spin-dependent force is a well-developed technique for the trapped ion community, it has never been viewed as the simulation of a special case of the QRM. For this experiment, we fixed the coupling strength to $g = (2\pi)12.5$ kHz, and vary δ_r and δ_b, while keeping always a ratio $g/\omega_m = 1.25$. For the degenerate case, we use detunings $\delta_b = -\delta_r = (2\pi)10$ kHz, while for the non-degenerate case we use $\delta_r = 0$

and $\delta_{\mathrm{b}} = (2\pi)20$ kHz, which corresponds to $\omega_0 = 0.8g$. For the initial state, we choose the ground state of the JC model $|\downarrow, 0\rangle$, which should have no dynamical properties when the coupling strength g/ω_{m} is small enough. In Fig. 5.2, we show that the situation is different when considering the DSC regime. First of all, in panels (a) and (b), we show the evolution of the population of Fock state $|0\rangle$, after tracing out the spin degree of freedom. For the degenerate case, we can clearly observe that this population collapses to zero and that it is stabilized at zero except every one period of the mode frequency, $k\frac{2\pi}{\omega_{\mathrm{m}}}$, k being an integer, where a full revival of the population is detected. On the other hand, the non-degenerate case shows long-time degradation of these revivals, as it was predicted in Ref.[79].

Additionally, we sample several points during one period $T = \frac{2\pi}{\omega_{\mathrm{m}}} = 100\mu s$ of the evolution of the degenerate case and measure its phonon distribution, as shown in panels (c-h). At time zero, the population is concentrated on Fock state $|0\rangle$, and as time elapses higher Fock states are populated. In fact, the quantum dynamics is exactly solvable and the time-dependent state evolves as $\frac{1}{\sqrt{2}}(|\downarrow, \alpha(t)\rangle + |\uparrow, -\alpha(t)\rangle)$ with $\alpha(t) = \frac{g}{2\omega_{\mathrm{m}}}(1 - \mathrm{e}^{i2\omega_{\mathrm{m}}t})$[27]. The evolution resembles a wavepacket that travels along a chain of Fock states up to a maximum determined by $\sim 4(g/\omega_{\mathrm{m}})^2$ and then comes back to the initial states at one period of the mode frequency. This phenomenon was theoretically predicted in Ref.[79] as characteristic of the DSC regime, and it is referred to as the bouncing back and forth of phonon-number wave packets. We note that similar reconstruction of the state can be found in Ref.[27] in the context of spin-dependent force. It has been also pointed out that the simulation of the Dirac equation can be interpreted as the simulation of the QRM in the DSC regime with infinite ratio by setting $\omega_{\mathrm{m}} = 0$[82,100–102].

5.3 Adiabatic ground-state preparation

As mentioned in the previous section, the ground state of the QRM in the Jaynes-Cummings regime ($g \ll \omega_{\mathrm{m}}$) is given by the state $|\downarrow, 0\rangle$, while the ground state of the QRM in the DSC regime is a nontrivial state where spin and field are entangled, and which to the best of our knowledge has never been implemented in a physical quantum platform.

In our experiment, we generate the ground state of the QRM in the DSC regime by starting in the ground state of the Jaynes-Cummings regime, the state $|\downarrow, 0\rangle$, and adiabatically increasing the coupling ratio g/ω_{m} towards the DSC regime. To achieve

this, one could choose to either increase $g = \eta\Omega/2$, which can be done by rising the laser intensity, or decrease $\omega_{\mathrm{m}} = (\delta_{\mathrm{b}} - \delta_{\mathrm{r}})/2$. Because it is experimentally more feasible to manipulate the detuning of the Raman lasers than their power, we choose the latter in our experiment. For that, we fix coupling strength g to be $(2\pi)12.5$ kHz and $\delta_{\mathrm{r}} = 0$, leaving δ_{b} as the only tunable parameter, which we manipulate with an exponential time dependence of the form $\delta_{\mathrm{b}}(t) = (\delta_{\mathrm{Max}} - \delta_{\mathrm{Tar}})e^{-\frac{t}{\tau}} + \delta_{\mathrm{Tar}}$. Here, we set $\delta_{\mathrm{Max}} = (2\pi)0.2$ MHz, while δ_{Tar} is determined by the ratio g/ω_{m} we want to reach, and $\tau = \frac{t_{\mathrm{Tar}}}{10}$, $t_{\mathrm{Tar}} = 300$ μs being the total duration of the adiabatic process. The adiabaticity of our scheme is guaranteed by the numerical computation of the fidelity between the instantaneous ground state of the Hamiltonian and the adiabatically evolved state, which is shown in Fig. 5.3a. Here, the fidelity is defined as $\mathrm{Tr}\sqrt{\sqrt{\rho_{\mathrm{id}}(t)}\rho(t)\sqrt{\rho_{\mathrm{id}}(t)}}$[89], where ρ_{id} is the ideal instantaneous ground state obtained from direct diagonalization, and ρ is the state resulting from the numerical calculation of the time evolution. We note that the fidelity of the $|\downarrow, 0\rangle$ state to the ideal ground state in the case of $g/\omega_{\mathrm{m}} = 0.125$ is of 99.8%. With sideband cooling, we are able to prepare the $|\downarrow, 0\rangle$ state with a fidelity of around 99.7%. Therefore, the total infidelity of our prepared ground state with respect to the ideal one is of around 0.5% , which is much smaller than the detection capability in our system.

In panel (b) of Fig. 5.3, we show the spin evolution during the adiabatic process for the time interval (0-t_{Tar}). The plot corresponds to the case $g/\omega_{\mathrm{m}} = 1.2$, with the cases for other ratios showing similar behavior. At time t_{Tar}, the system is expected to be in the ground state of the QRM for the selected coupling regime. In panels (d) to (f), we plot the outcome of the phonon distributions correlated with the spin at t_{Tar} for coupling ratios $g/\omega_{\mathrm{m}} = 1.2$, 1.5 and 2.0, respectively (see Methods C). To measure the phonon-number distribution correlated with state $|\downarrow\rangle$ of the spin, we first perform a spin-dependent fluorescence detection and select the case of no fluorescence, which corresponds to the spin being projected to $|\downarrow\rangle$ state. Then we drive the blue-sideband transition, monitor the population of $|\uparrow\rangle$ state and fit the signal to the function in Eq. (5-8) as described in Methods C. This provides the conditional phonon-number distribution normalized to the probability of being in the spin state $|\downarrow\rangle$. To measure the phonon-number distribution correlated with the spin state $|\uparrow\rangle$, we first flip the spin and then follow the same procedure as that for the case of state $|\downarrow\rangle$.

From panels (d) to (f) in Fig. 5.3, we clearly observe that larger phonon-number states are populated in the prepared ground states as the ratio g/ω_{m} increases. We also observe

that the populations are distributed mostly along the same parity chain, which is expected from the Z_2 symmetry of the QRM[79]. We quantify the parity conservation by measuring the expectation value of the parity operator $\hat{\Pi} = \sigma_z e^{-i\pi \hat{a}^\dagger \hat{a}}$, which has eigenvalues ± 1. The measured parities for the states of Figs. 5.3 (d-f) are 0.74(0.08), 0.70(0.08) and 0.52(0.13), respectively, showing that the prepared ground states in the DSC regime mostly dwell in the same parity chain. As the coupling ratio increases, the measured parity deviates from the ideal parity value +1 due to imperfections in the adiabatic process and the motional heating arising from the occupation of large Fock states. Note here the motional heating rate is proportional to the phonon number, as more phonons involved, it introduce severe decoherence. We experimental study this heating carefully in one of our paper[53].

To verify the quantum coherence maintained within the preparation of the ground state, we reverse the adiabatic process in an attempt to recover the initial ground state $|\downarrow, 0\rangle$. In panel (b), we can observe how the spin returns to state $|\downarrow\rangle$. As a complementary proof, we plot the purity of the spin state. To this aim, we trace out the phononic degrees of freedom and measure the density matrix $\hat{\rho}_{spin}$ associated with the spin degree of freedom[89], from which we calculate the purity, defined as $\text{Tr}(\hat{\rho}_{spin}^2)$, during the whole process. The degradation of the purity during the preparation of the ground state of the QRM in the DSC regime confirms that the adiabatically prepared ground state is indeed an entangled state, and the subsequent revival of the purity when the adiabatic process is inverted proves that we are able to recover the initial state and therefore that the whole process preserves quantum coherence.

By measuring the probability of recovering the initial state $|\downarrow, 0\rangle$ after the ground state preparation and reverse process at time t_{Rev}, we estimate a lower bound of the purity of the prepared ground state. The revival probabilities are 0.89(0.024), 0.87(0.027) and 0.79(0.03) for the three ratios $g/\omega_{\text{m}} = 1.2, 1.5$ and 2.0, which give the lower bounds 0.79(0.042), 0.75(0.047) and 0.62(0.047), respectively. As shown in Fig. 5.3c, the reduced-spin purities, taking values 0.545(0.006), 0.514(0.003) and 0.505(0.002), are significantly smaller than the lower bounds of the total system, which prove the existence of entanglement within the prepared ground state at t_{Tar} (See Methods D).

5.4 Energy Spectrum

The ground-state preparation can be extended to study the low-lying energy spectrum of the QRM by coherent spectroscopy[103]. In particular, we have measured the energy

spectrum in the region $g/\omega_m \in [0, 1]$. A Z_2 parity exists in the QRM model, which divides the Hilbert space in two, namely a subspace of parity $+1$ and other of parity -1[79]. Here, we focus on the energy splittings between the ground state and the first three excited states of opposite parity to the ground state[79]. For that, we have used a relatively weak modulated field as a probe on top of the simulation of the QRM, with the system initially in the ground state of the corresponding regime. We sweep the frequency of the probe pulse until we detect a transition, and we associate the frequency of the probe to the energy difference of the transition. To generate transitions between states of opposite parity, we use the probe pulse of the form

$$\hat{H}_{\text{mod}} = \hat{H}_{\text{QRM}} + g_p \sin(2\pi\nu_p t)(\hat{\sigma}_+ + \hat{\sigma}_-), \tag{5-6}$$

where $g_p(\ll g)$ is the strength of the modulation field, and ν_p is swept to find the resonant frequencies. In the region $g/\omega_m = 0.1$ to 0.3, g_p/g is 0.02, while the pulse duration is 350 μs. For the ratios $g/\omega_m = 0.4$ to 1.0, the ratio g_p/g is 0.01, with a pulse duration of 450 μs. Population transfer is clearly seen when ν_p is resonant with the energy splittings as shown in Fig. 5.4.

5.5 Methods

Methods A: Calibration of the detuning of the blue and red sideband transitions

For the simulation of the case $g/\omega_m = 0.04$, we set $\delta_r = 0$, while δ_b takes a much larger value than its corresponding coupling strength. To achieve that configuration, we obtain the resonance frequency of the red-sideband transition with the detuning of the blue-sideband transition fixed at $\delta_b = (2\pi)625$ kHz. For the USC/DSC regime, the coupling strength is comparable to the effective mode frequency, such that we need to carefully deal with the ac-Stark shift introduced by an off-resonant excitation of the carrier transition. We measure the ac-Stark shift with a Ramsey experiment and calibrate the shift in the bichromatic pulse within 1 kHz of accuracy. We further improve the frequency precision within a 0.15 kHz range by setting the same detuning $\delta = (2\pi)10$ kHz with different signs for each beam, similarly to the scheme in Refs.[98,104].

Methods B: Numerical Simulations

For the numerical simulations, we compute the time evolution of the system according to a Lindblad master equation that accounts for experimental imperfections resulting in heating and dephasing of the motional modes[53],

$$
\begin{aligned}
\dot{\rho}(t) = &- i \left[\hat{H}, \rho(t) \right] \\
&- \Gamma \left(\rho(t)\hat{a}^\dagger \hat{a}\hat{a}^\dagger \hat{a} - 2\hat{a}^\dagger \hat{a}\rho(t)\hat{a}^\dagger \hat{a} + \hat{a}^\dagger \hat{a}\hat{a}^\dagger \hat{a}\rho(t) \right) \\
&- \frac{\gamma}{2} n_{\text{th}} \left(\hat{a}\hat{a}^\dagger \rho(t) - 2\hat{a}^\dagger \rho(t)\hat{a} + \rho(t)\hat{a}\hat{a}^\dagger \right) \\
&- \frac{\gamma}{2} (n_{\text{th}} + 1) \left(\hat{a}^\dagger \hat{a}\rho(t) - 2\hat{a}\rho(t)\hat{a}^\dagger + \rho(t)\hat{a}^\dagger \hat{a} \right).
\end{aligned}
\tag{5-7}
$$

Here, Γ is the dephasing parameter, which we set to be $\Gamma = \frac{1}{\tau}$, with $\tau = 2.5$ ms, γ is the coupling strength between the ion motion and the thermal reservoir, and n_{th} is the average phonon number when the system is in equilibrium with the environment. In our model, the effective temperature of the thermal reservoir is infinite, which makes n_{th} extremely large and $\gamma n_{\text{th}} \approx \gamma(n_{\text{th}} + 1)$. It is natural to define the heating rate as γn_{th}, which is measured as 70 quanta s^{-1} in our system. The Hamiltonian employed in our simulations includes experimental parameters specific to our setup and takes the form of Eq. (5-5).

Methods C: Phonon number state population distribution

In Fig. 5.2 and Fig. 5.3, we obtain the phonon number distribution. This is performed by driving a resonant blue-sideband transition $|\downarrow, n\rangle \leftrightarrow |\uparrow, n + 1\rangle$ followed by a spin projective measurement and fitting the obtained spin-excitation evolution with the formula[53,58,93]

$$
P_{|\uparrow\rangle}(t) = \frac{1}{2} \sum_n p(n)[1 - e^{-\gamma t} \cos(\sqrt{n + 1}\eta\Omega t)],
\tag{5-8}
$$

where $p(n)$ is the phonon number state population, γ is an empirical decay constant, and t is the pulse duration of the blue sideband. From the phonon distribution, we can then directly calculate the average phonon number that we plotted in Fig. 5.1(d-g). Notice that the more populated the motional Hilbert space the more data points are needed to fit Eq. (5-8), as more $p(n)$ take part in the equation. As a consequence of this, the error bars for the expectation value of the phonon number in Fig. 5.1(d-g), are greater for larger coupling regimes, where higher phonon numbers are involved in the dynamics.

Methods D: Verification of entanglement for the ground-state of the quantum Rabi model

In the main text, we use $\mathrm{Tr}\left[\hat{\rho}_{\mathrm{spin}}^2\right] - P_{\mathrm{Rev}}^2 < 0$ to verify the existence of entanglement between the spin and the phonon degrees of freedom. This can be understood as follows. First, we introduce the purity-based entanglement witness[105,106] $\mathcal{W}$ for the target state $\hat{\rho}_{\mathrm{Tar}}$ at time t_{Tar}, which is defined as

$$\mathcal{W}\left[\hat{\rho}_{\mathrm{Tar}}\right] \equiv \mathrm{Tr}\left[\hat{\rho}_{\mathrm{spin}}^2\right] - \mathrm{Tr}\left[\hat{\rho}_{\mathrm{Tar}}^2\right]. \tag{5-9}$$

It can be proven that $\mathcal{W}\left[\hat{\rho}\right] \geq 0$ for any separable state. Thus, $\mathcal{W}\left[\hat{\rho}\right] < 0$ serves as a sufficient condition for the inseparability of $\hat{\rho}$. However, the purity of the whole system $\mathrm{Tr}\left[\hat{\rho}_{\mathrm{Tar}}^2\right]$ requires the reconstruction of the total density matrix $\hat{\rho}_{\mathrm{Tar}}$ at time t_{Tar}, which is quite demanding in our current experimental setup. Instead, after adiabatically preparing the ground state of the system, we reverse the adiabatic process, which disentangles the prepared ground state, and then measure the component $P_{\mathrm{Rev}} \equiv \mathrm{Tr}[|\downarrow, 0\rangle\langle\downarrow, 0|\hat{\rho}_{\mathrm{Rev}}]$ of the spectral decomposition of the obtained final state at time t_{Rev}, which corresponds to the probability of recovering the initial state. It's straightforward to see that $P_{\mathrm{Rev}}^2 \leq \mathrm{Tr}\left[\hat{\rho}_{\mathrm{Rev}}^2\right]$. In general, unitary evolutions conserve the purity of a system, while the non-unitary contributions to the evolution that may arise during the process, mainly from random fluctuations in frequencies and intensities of lasers or the dephasing and heating of the motional modes, can only decrease the purity of the system, an effect that cannot be canceled by the reversed adiabatic process. Therefore, it is reasonable to assume that after the whole process in this experiment the purity of the system is not increased. Under such an assumption the following inequality can be stablished

$$\mathrm{Tr}\left[\hat{\rho}_{\mathrm{Tar}}^2\right] \geq \mathrm{Tr}\left[\hat{\rho}_{\mathrm{Rev}}^2\right] \geq P_{\mathrm{Rev}}^2. \tag{5-10}$$

In other words, P_{Rev}^2 serves as a lower bound for $\mathrm{Tr}\left[\hat{\rho}_{\mathrm{Tar}}^2\right]$. Putting Eqs. (5-9) and (5-10) together, we have

$$\mathcal{W}\left[\hat{\rho}_{\mathrm{Tar}}\right] \leq \mathrm{Tr}\left[\hat{\rho}_{\mathrm{spin}}^2\right] - P_{\mathrm{Rev}}^2. \tag{5-11}$$

Methods E: Calibration of laser intensities

In the experiments, we calibrate the imbalance between Ω_b and Ω_r within at most $\epsilon = 3\%$, which is described by $\Omega_b = (1 \pm \epsilon)\Omega_r$. This imbalance could modify the target QRM Hamiltonian as $\hat{H}_{QRM,im}$

$$
\begin{aligned}
\hat{H}_{QRM,im} = \; & \frac{\omega_0}{2}\hat{\sigma}_z + \omega_m\hat{a}^\dagger\hat{a} + g(1 + \frac{\epsilon}{2})(\hat{\sigma}_+ + \hat{\sigma}_-)(\hat{a} + \hat{a}^\dagger) \\
& + \frac{\epsilon}{2}(\hat{\sigma}_+ - \hat{\sigma}_-)(\hat{a} - \hat{a}^\dagger).
\end{aligned}
\tag{5-12}
$$

We observe that the effect of such an imperfection is reflected in the coupling strength g that changes to $g_\epsilon = g(1 + \frac{\epsilon}{2})$ and in the extra term $\frac{\epsilon}{2}(\hat{\sigma}_+ - \hat{\sigma}_-)(\hat{a} - \hat{a}^\dagger)$. In Fig. 5.5, we perform numerical calculations to evaluate the effect of these terms and conclude that the main deviations from the ideal case arise from the change in coupling strength.The plotted numerical results correspond to the cases discussed in Fig. 5.1 with an imperfection of $\epsilon = \pm3\%$. No significant deviation is observed from the perfectly calibrated case. Here by no significant we mean that the deviations are not larger than the already considered experimental error bars.

5.6　Conclusion

We have implemented the quantum simulation of all relevant coupling regimes of the QRM in a single trapped ion, obtaining direct evidence of the breakdown of the RWA. In the DSC regime, we observe the phonon number wave-packets bounce back and forth as well as collapses and revivals of the initial state, confirming previous theoretical predictions. The adiabatic preparation of the ground state of the QRM in the DSC regime was produced for the first time in a quantum platform, and its reconstruction has enabled us to demonstrate the entanglement present in its ground state. As a direct application of this adiabatic method, we have been able to measure the energy splittings between states of different parity and recreate the energy spectrum of the QRM in the USC regime. In conclusion, our work presents a detailed experimental exploration of the QRM in a wide range of physical regimes. From a theoretical point of view, our work justifies further research in light-matter coupling regimes that are, a priori, not found in nature, as we are providing a platform where all these regimes can be physically implemented. Our experimental methods can be directly extended to the study of the phase transition in the QRM[107–109] or to the simulation of the Dicke model[110–112] by considering the presence
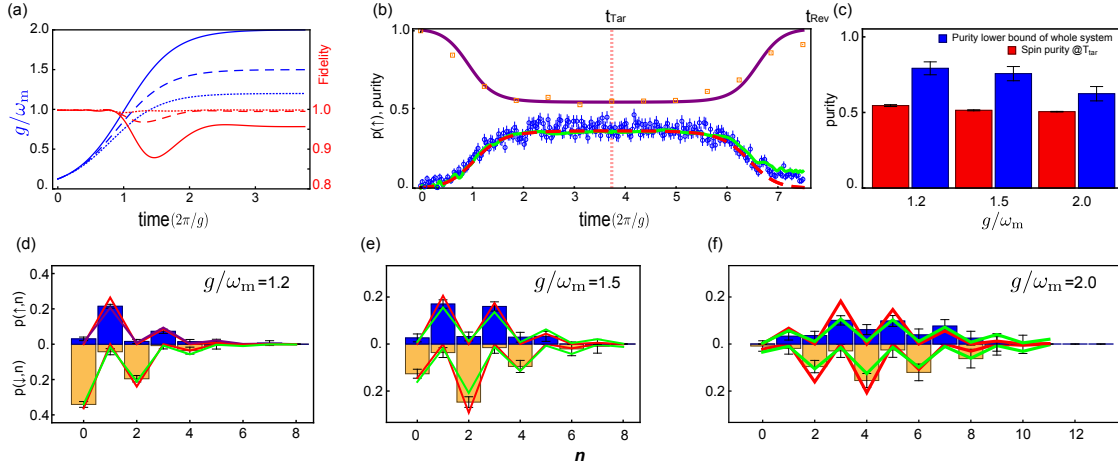
of more ions.

图 5.3   Adiabatic ground state preparation of the QRM in the DSC regime. In panel (a), we show the adiabatic scheme for the preparation of the ground state of the QRM at the DSC ratios $g/\omega_{\mathrm{m}} = 1.2, 1.5$, and 2.0, as starting from the initial JC ratio $g/\omega_{\mathrm{m}} = 0.125$. The fidelities between the instantaneous ground state and the numerically evolved state quantify the adiabaticity of our process. In panel (b), we show the evolution of the excitation probability and the purity of spin state during the adiabatic ground state preparation ($0 \leq t \leq t_{\mathrm{Tar}}$) and during the reverse process ($t_{\mathrm{Tar}} \leq t \leq t_{\mathrm{Rev}}$). The plot corresponds to the preparation of the ground state at the ratio $g/\omega_{\mathrm{m}} = 1.2$. The red dashed line and the green solid line are obtained by direct diagonalization of the QRM Hamiltonian and numerical simulation of the adiabatic process, respectively, including heating and dephasing of the motional mode, which are expected experimental imperfections. The blue circles with error bars correspond to the experimental results. The purple line represents the numerically computed purity of the spin, defined as $\mathrm{Tr}(\hat{\rho}_{\mathrm{spin}}^2)$, where $\hat{\rho}_{\mathrm{spin}}$ is the reduced density matrix of the spin after tracing out the motional degree of freedom. The orange squares are the corresponding experimental results, computed from the spin-tomography [89,90]. Panels (d) to (f) show the phonon-number distributions correlated with $|\downarrow\rangle$ (lower panel) and $|\uparrow\rangle$ (upper panel), which are obtained by fitting the standard blue-sideband signals after the spin-projective measurement for $g/\omega_{\mathrm{m}} = 1.2, 1.5$, and 2.0, respectively. The red solid line and the green solid line are obtained by direct diagonalization of the QRM Hamiltonian and numerical simulation of the adiabatic process, respectively, including heating and dephasing of the motional mode, which are expected experimental imperfections. Finally, panel (c) shows the purity of the spin and estimated lower bounds for the purity of the whole system, for each tested coupling ratio. The purity of the spin is obtained from the measured reduced density matrix, which was done by spin-tomography. The lower bounds of the purities of the whole system are estimated by measuring the probability of being in $|\downarrow, 0\rangle$ after the reverse process at t_{Rev}. Note that we get the numerical simulation results in (b-f) by solving the Lindblad master equation (see Methods B).
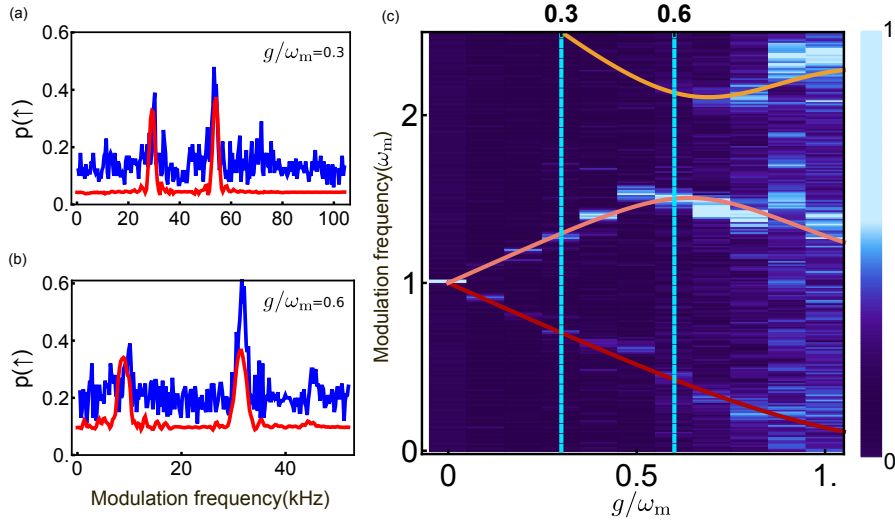
图 5.4   Spectrum of the QRM. Panels (a) and (b) show, respectively for the regimes $g/\omega_\mathrm{m} = 0.3$ and 0.6, the population of the excited state of the spin as a function of the modulation frequency of the probe driving. The red curve corresponds to numerical simulation results, while the blue curve shows the experimental data. Panel (c) shows the energy spectrum with the modulation frequency of the probe drive in the vertical axis rescaled by ω_m. Note that the energy of the ground state (not plotted) is taken to be zero for all cases. The three continuous curves on top of the plot show the numerically computed energy spectrum of the states with parity opposite to the ground state.
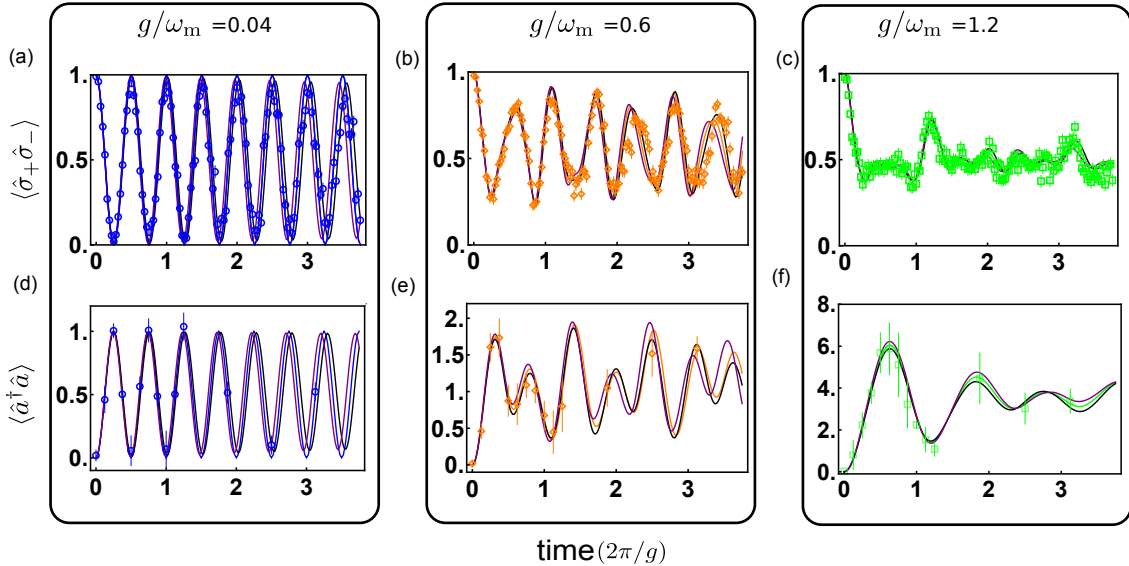
图 5.5   Spin and phonon dynamics under the QRM for different coupling regimes with the imbalance between Ω_b and Ω_r. The black and the purple curves correspond to the results of numerical simulations with $\Omega_\mathrm{b} = (1 - \epsilon)\Omega_\mathrm{r}$ and $\Omega_\mathrm{b} = (1 + \epsilon)\Omega_\mathrm{r}$, respectively, setting $\epsilon = 3\%$, for the cases shown Fig. 5.1.

第6章　Summary and outlook

During the Ph.D. carrier, I have studied the quantum optics, which is the foundation to understand the ion-laser interaction. While for the experimental part, I divide the time into two parts. The previous two years, I mainly focus on the four rods trap, in which I conduct the experiments of studying the JCM model in phase space with Q function. In this work, I develop the efficient vacuum measurement method, which is the key ingredients for the construction of Q function. Meanwhile, I have realized the direct reconstruction from the Q function to its density matrix with the least square method.

Later, after we move the Lab from CQI to MMW building, I mainly spend the time together with Dr. An, who has been a postdoc now at Oxford University. He designs the blade trap, while we assemble and test together. We meet many expected and unexpected problems during the process of testing blade trap until we finally reach a status that can run our experiment. Meanwhile, I am the first one in our group to study the DDS. I design the circuit to provide the DC voltage for the DDS source and write the Verilog code to control the DDS through FPGA. In the future, the DDS could be embedded in the FPGA board to implement fast control and easy configuration.

After we finish the testing of the blade trap, I conduct the first experiments: simulation of the quantum Rabi model. In this work, we prepare the ground state of QRM in deep-strong coupling regime for the first time and observe the property of entanglement and conservation of parity value. Due to the limit motional coherence time, with the hint of my supervisor, I come up with the idea of changing the detuning of the laser exponentially. This method reduces the adiabatic preparation time quite a lot.

In our setup, there could be the following two experiments to run in the near future.

The first project is to simulate the beam splitting(BS) operator[113]. In the experiment, this operation has been used to study Hong-Ou-Mandel interference[114]. Here, we may employ the BS operation to check the fidelity measurements between the two motional modes. The two modes of the ion could serve as the two input port of the BS. When two modes have the same input state, ideally, the fidelity should be 1. In this experiment, we could prepare different input states in two modes, or we fix one of the input states in one mode, while changes the other mode's state. We check the fidelity by measuring the parity of one of the mode.

The second project could extend our study to the super-radiant quantum phase transition of QRM. In this work, we may realize the Rabi model in the limit of a large ratio of the effective atomic transition frequency to the oscillator frequency. We shall show that there exists equilibrium and non-equilibrium universal functions of the Rabi model by finding a proper rescaling of the system parameters and observables[107,108].

In the long run, the most important thing is to scale up the number of ions that we can manipulate and buy a new pulse laser with large enough output power. The blade trap is a promising platform to do the scalable quantum computation and quantum simulation. The micromotion along the axial direction should take into consideration seriously in order to confine a ion chain stably along the axis. The control system of single ion addressing should also develop and the multi-channel PMT system may involve in the future.

参考文献

[1] Glauber R. Coherent and Incoherent States of the Radiation Field[J]. Phys. Rev, 1963, 131(6): 2766.

[2] Rabi I. On the process of space quantization[J]. Phys. Rev., 1936, 49(4): 324.

[3] Jaynes E, Cummings F. Comparison of quantum and semiclassical radiation theories with application to the beam maser[J]. Pro. IEEE, 1963, 51(1): 89–109.

[4] Haroche S. Controlling Photons in a Box and Exploring the Quantum to Classical Boundary[J]. Rev. Mod. Phys., 2013, 85(1083).

[5] Wineland D. Superposition, entanglement, and raising Schrdinger's cat[J]. Rev. Mod. Phys., 2013, 85(1103).

[6] Monroe C, Meekhof D, King B, et al. Resolved-sideband Raman cooling of a bound atom to the 3D zero-point energy[J]. Phys. Rev. Lett., 1995, 75(22): 4011.

[7] Cirac J, Zoller P. Quantum Computations with Cold Trapped Ions[J]. Phys. Rev. Lett., 1995, 74(4091).

[8] Lloyd S. Universal Quantum Simulators[J]. Science, 1996, 273(5278): 1073–1078.

[9] Lanyon B, Roos C. Universal digital quantum simulation with trapped ions.[J]. Science, 2011, 334(6052): 57–61.

[10] Blatt R, Roos C. Quantum simulations with trapped ions[J]. Nat. Phy., 2012, 8(4): 277–284.

[11] Raimond J M, Haroche S. Exploring the Quantum: Atoms, Cavities, and Photons[M]. [S.l.]: Oxford Uni. Press, Oxford, 2006: 151–161

[12] Scully M. Quantum optics[M]. [S.l.]: Cambridge Uni. press, 1997

[13] Paul W. Electromagnetic Traps for Charged and Neutral Particles[J]. Rev. Mod. Phys., 1990, 29(7): 739–748.

[14] Dehmelt H. Radio frequency Spectroscopy of Stored Ions I : Storage[J]. Adv. At. Mol. Phys., 1967, 3: 53–72.

[15] Brown L, Gabrielse G. Geonium Theory: Physics of a Single Electron or Ion in a Penning Trap [J]. Rev. Mod. Phys., 1986, 58(1): 233–311.

[16] Siverns J, Simkins L, Weidt S, et al. On the application of radio frequency voltages to ion traps via helical resonators[J]. Appl. Phys. B, 2012, 107(4): 921–934.

[17] An S. Quantum control in the trapped ion system[D]. Beijing: Tsinghua University, 2017.

[18] Macalpine W, Schildknecht R. Coaxial Resonators with Helical Inner Conductor[J]. Proc. Inst. Radio Eng., 1959, 47(12): 2099–2105.

[19] Berkeland D, Boshier M. Destabilization of dark states and optical spectroscopy in Zeeman − degenerate atomic systems[J]. Phys. Rev. A, 2002, 65(3): 427–443.

[20] Lee M, Jarratt M, Marciniak C, et al. Frequency stabilization of a 369 nm diode laser by nonlinear spectroscopy of ytterbium ions in a discharge[J]. OPT EXPRESS, 2014, 22(6): 7210–7221.

[21] James D, Jerke J. Effective Hamiltonian Theory and its Applications in Quantum Information [J]. Canadian Journal of Physics, 2011, 85(6): 625.

[22] Islam R, Campbell W, Choi T, et al. Beat note stabilization of mode-locked lasers for quantum information processing[J]. Opt Lett, 2014, 39(11): 3238–3241.

[23] Johnson K, Wongcampos J, Restelli A, et al. Active stabilization of ion trap radio frequency potentials[J]. Rev. Sci. Instrum., 2016, 87(5): 525.

[24] Berkeland D, Miller J, Bergquist J, et al. Minimization of ion micromotion in a Paul trap[J]. J. Appl. Phys., 1998, 83(10): 5025–5033.

[25] Ye W, Mark U, J.H. Z, et al. Single-qubit quantum memory exceeding ten-minute coherence time[J]. Nat. Phot., 2017, 11.

[26] Häffner H, Gulde S, Riebe M, et al. Precision measurement and compensation of optical stark shifts for an ion-trap quantum processor.[J]. Phys. Rev. Lett., 2003, 90(14): 143602.

[27] Poschinger A, U.and Walther, Singer K, Schmidt-Kaler F. Observing the phase space trajectory of an entangled matter wave packet[J]. Phys. Rev. Lett., 2010, 105(26): 263602.

[28] Wineland D J, Monroe C, Itano W M, et al. Experimental Issues in Coherent Quantum − State Manipulation of Trapped Atomic Ions[J]. J. Res. Natl. Inst. Stand. Technol., 1998, 103(3): 259–328.

[29] Cahill K E, Glauber R J. Density Operators and Quasiprobability Distributions[J]. Phys. Rev. Lett., 1969, 177: 1882.

[30] Kenfack A, Zyczkowski K. Negativity of the Wigner function as an indicator of non-classicality [J]. J. Opt. B: Quantum Semiclass. Opt., 2004, 6: 396–404.

[31] Phoenix S, Knight P. Fluctuations and entropy in models of quantum optical resonance[J]. Ann. Phys., 1988, 186(2): 381–407.

[32] Gea-Banacloche J. Collapse and revival of the state vector in the Jaynes − Cummings model: An example of state preparation by a quantum apparatus[J]. Phys. Rev. Lett., 1990, 65: 3385–3388.

[33] Gea-Banacloche J. Atom-and field-state evolution in the Jaynes − Cummings model for large initial fields[J]. Phys. Rev. A, 1991, 44(9): 5913.

[34] Eiselt J, Risken H. Calculation of quasiprobabilities for the damped Jaynes − Cummings model [J]. Opt. Comm., 1989, 72(6): 351–355.

[35] Eiselt J, Risken H. Quasiprobability distributions for the Jaynes − Cummings model with cavity damping[J]. Phys. Rev. A, 1991, 43(1): 346.

[36] Auffeves A, Maioli P, Meunier T, et al. Entanglement of a mesoscopic field with an atom induced by photon graininess in a cavity[J]. Phys. Rev. Lett, 2003, 91(23): 230405.

[37] Raimond J M, Meunier T, Bertet P, et al. Probing a quantum field in a photon box[J]. J. Phys. B: At. Mol. Opt. Phys., 2005, 38: S535–S550.

[38] Greiner M, Mandel O, Hänsch T, et al. Collapse and revival of the matter wave field of a Bose − Einstein condensate[J]. Nature, 2002, 419(6902): 51–54.

[39] Kirchmair G, Vlastakis B, Leghtas Z, et al. Observation of quantum state collapse and revival due to the single-photon Kerr effect[J]. Nature, 2013, 495: 205–209.

[40] Smithey D T, Beck M, Raymer M G, et al. Measurement of the Wigner distribution and the density matrix of a light mode using optical homodyne tomography: Application to squeezed states and the vacuum[J]. Phys. Rev. Lett., 1993, 70: 1244–1247.

[41] Lvovsky A, Raymer M. Continuous-variable optical quantum-state tomography[J]. Rev. Mod. Phys., 2009, 81: 299–332.

[42] Kurtsiefer C, Pfau T, Mlynek J. Measurement of the Wigner function of an ensemble of helium atoms[J]. Nature, 1997, 386: 150–153.

[43] Dunn T, Walmsley I, Mukamel S. Experimental determination of the quantum-mechanical state of a molecular vibrational mode using fluorescence tomography[J]. Phys. Rev. Lett., 1995, 74: 884–887.

[44] Monroe C, Meekhof D, King B, et al. A Schrdinger cat superposition state of an atom[J]. Science, 1996, 272(5265): 1131.

[45] Leibfried D, Meekhof D, King B, et al. Experimental determination of the motional quantum state of a trapped atom[J]. Phys. Rev. Lett., 1996, 77(21): 4281.

[46] Kienzler D, Flühmann C, Negnevitsky V, et al. Observation of quantum interference between separated mechanical oscillator wavepackets[J]. Phys. Rev. Lett., 2016, 116: 140402.

[47] Ding S Q, Maslennikov G, Hablützel R, et al. Quantum parametric oscillator with trapped ions [J]. Phys. Rev. Lett., 2017, 119(15): 150404.

[48] Deleglise S, Dotsenko I, Sayrin C, et al. Reconstruction of non-classical cavity field states with snapshots of their decoherence[J]. Nature, 2008, 455(7212): 510–514.

[49] Hofheinz M, Wang H, Ansmann M, et al. Synthesizing arbitrary quantum states in a superconducting resonator[J]. Nature, 2009, 459: 545–549.

[50] Vlastakis B, Kirchmair G, Leghtas Z, et al. Deterministically encoding quantum information using 100-photon Schrdinger cat states[J]. Science, 2013, 342(6158): 607–610.

[51] Oi D K L, Potoček V, Jeffers J. Nondemolition Measurement of the Vacuum State or its Complement[J]. Phys. Rev. Lett., 2013, 110: 210504.

[52] Gebert F, Wan Y, Wolf F, et al. Detection of motional ground state population of a trapped ion using delayed pulses[J]. New J. Phys., 2016, 18: 013037.

[53] An S M, Zhang J N, Um M, et al. Experimental test of the quantum Jarzynski equality with a trapped-ion system[J]. Nat. Phys., 2015, 11(2): 193.

[54] U. M, Zhang J, L. D, et al. Phonon arithmetic in a trapped ion system[J]. Nat. Commun., 2016, 7: 11410.

[55] Demirplak M, Rice S. Adiabatic population transfer with control fields[J]. The J. Phys. Chem. A, 2003, 107(46): 9937–9945.

[56] Berry M. Transitionless quantum driving[J]. J. Phys. A: Math. Theor., 2009, 42(36): 365303.

[57] Zhang J, Zhang J, Zhang X, et al. Realization of geometric landau-zener-stückelberg interferometry[J]. Phys. Rev. A, 2014, 89(1): 013608.

[58] Meekhof D, Monroe C, King B, et al. Generation of nonclassical motional states of a trapped atom[J]. Phys. Rev. Lett., 1996, 76(11): 1796.

[59] Leibfried D, Blatt R, Monroe C, et al. Quantum dynamics of single trapped ions[J]. Rev. Mod. Phys., 2003, 75(1): 281.

[60] Häffner C, H.and Roos, Blatt R. Quantum computing with trapped ions[J]. Phys. Rep., 2008, 469(4): 155–203.

[61] Eberly J, Narozhny N, Sanchez-Mondragon J. Periodic spontaneous collapse and revival in a simple quantum model[J]. Phys. Rev. Lett., 1980, 44(20): 1323.

[62] Barnett S, Radmore P. Methods in theoretical quantum optics[M]. [S.l.]: Oxford Uni. Press, 1997

[63] Bužek V, Moya-Cessa H, Knight P, et al. Schrödinger-cat states in the resonant Jaynes－Cummings model: Collapse and revival of oscillations of the photon-number distribution[J]. Phys. Rev. A, 1992, 45(11): 8190.

[64] Morigi E, G.and Solano, Englert B G, Walther H. Measuring irreversible dynamics of a quantum harmonic oscillator[J]. Phys. Rev. A, 2002, 65(4): 040102.

[65] Meunier T, Gleyzes S, Maioli P, et al. Rabi oscillations revival induced by time reversal: A test of mesoscopic quantum coherence[J]. Phys. Rev. Lett., 2005, 94(1): 010401.

[66] Rodriguez-Lara B, Moya-Cessa H, Klimov A. Combining Jaynes－Cummings and anti－Jaynes－Cummings dynamics in a trapped-ion system driven by a laser[J]. Phys. Rev. A, 2005, 71(2): 023811.

[67] Frisch R, Segre E. Über die Einstellung der Richtungsquantelung. II[J]. Zeits. f. Physik, 1933, 80(9): 610.

[68] Miller R, Northup T, Birnbaum K, et al. Trapped atoms in cavity QED: coupling quantized light and matter[J]. J. Phys. B At. Mol. Opt. Phys., 2005, 38(9): S551.

[69] Walther H, Varcoe B T, Englert B, et al. Cavity quantum electrodynamics[J]. Rep. Prog. Phys., 2006, 69(5): 1325.

[70] Ritsch H, Domokos P, Brennecke F, et al. Cold atoms in cavity-generated dynamical optical potentials[J]. Rev. Mod. Phys., 2013, 85(2): 553.

[71] Hanson R, Kouwenhoven L, Petta J, et al. Spins in few-electron quantum dots[J]. Rev. Mod. Phys., 2006, 79(4): 1217.

[72] Wallraff A, Schuster D, Blais A, et al. Strong coupling of a single photon to a superconducting qubit using circuit quantum electrodynamics[J]. Nature, 2004, 431(7005): 162.

[73] Devoret M, Schoelkopf R. Superconducting circuits for quantum information: an outlook[J]. Science, 2013, 339(6124): 1169.

[74] Lv D, An S, Um M, et al. Reconstruction of the Jaynes-Cummings field state of ionic motion in a harmonic trap[J]. Phys. Rev. A, 2017, 95(4): 043813.

[75] Niemczyk T, Deppe F, Huebl H, et al. Circuit quantum electrodynamics in the ultrastrong-coupling regime[J]. Nat. Phys., 2010, 6(10): 772.

[76] Forn-Díaz P, García-Ripoll J, Peropadre B, et al. Ultrastrong coupling of a single artificial atom to an electromagnetic continuum in the nonperturbative regime[J]. Nat. Phys., 2017, 13(1): 3943.

[77] Yoshihara F, Fuse T, Ashhab S, et al. Superconducting qubit-oscillator circuit beyond the ultrastrong-coupling regime[J]. Nat. Phys., 2017, 13(1): 44.

[78] Rossatto D, Villas-Bôas C, Sanz M, et al. Spectral classification of coupling regimes in the quantum Rabi model[J]. Phys. Rev. A, 2017, 96(1): 013849.

[79] Casanova J, Romero G, Lizuain I, et al. Deep strong coupling regime of the Jaynes-Cummings model[J]. Phys. Rev. Lett., 2010, 105(26): 263603.

[80] Romero G, Ballester D, Wang Y, et al. Ultrafast quantum gates in circuit QED[J]. Phys. Rev. Lett., 2012, 108(12): 120501.

[81] Braak D. Integrability of the Rabi model[J]. Phys. Rev. Lett., 2011, 107(10): 100401.

[82] Pedernales J, Lizuain I, Felicetti S, et al. Quantum Rabi model with trapped ions[J]. Sci. Rep., 2015, 5: 15472.

[83] Lolli J, Baksic A, Nagy D, et al. Ancillary qubit spectroscopy of vacua in cavity and circuit quantum electrodynamics[J]. Phys. Rev. Lett., 2015, 114(18): 183601.

[84] Jaako T, Xiang Z L, Garcia-Ripoll J, et al. Ultrastrong-coupling phenomena beyond the Dicke model[J]. Phys. Rev. A, 2016, 94(3): 033850.

[85] Andersen C, Blais A. Ultrastrong coupling dynamics with a transmon qubit[J]. New J. Phys., 2017, 19(2): 023022.

[86] Crespi A, Longhi S, Osellame R. Photonic realization of the quantum Rabi model[J]. Phys. Rev. Lett., 2012, 108(16): 163601.

[87] Braumüller J, Marthaler M, Schneider A, et al. Analog quantum simulation of the Rabi model in the ultra-strong coupling regime[J]. Nat. Commun., 2017, 8(1): 779.

[88] Langford N, Sagastizabal R, Kounalakis M, et al. Experimentally simulating the dynamics of quantum light and matter at deep-strong coupling[J]. Nat. Commun., 2017, 8(1): 1715.

[89] Nielson M, Chuang I. Quantum Computation and Quantum Information[M]. [S.l.]: Cambridge Univ. Press, Cambridge, UK, 2000: 98–108, 409–414

[90] Roos C, Lancaster G, Riebe M, et al. Bell states of atoms with ultralong lifetimes and their tomographic state analysis[J]. Phys. Rev. Lett., 2004, 92(22): 220402.

[91] Haljan P, Brickman K, Deslauriers L, et al. Spin-dependent forces on trapped ions for phase-stable quantum gates and entangled states of spin and motion.[J]. Phys. Rev. Lett., 2005, 94 (15): 153602.

[92] McDonnell M, Home J, Lucas D, et al. Long-lived mesoscopic entanglement outside the Lamb-Dicke regime[J]. Phys. Rev. Lett., 2007, 98(6): 063603.

[93] Lo H Y, Kienzler D, de Clercq L, et al. Spin-motion entanglement and state diagnosis with squeezed oscillator wavepackets[J]. Nature, 2015, 521(7552): 336.

[94] Sørensen A, Mølmer K. Quantum computation with ions in thermal motion[J]. Phys. Rev. Lett., 1999, 82(9): 1971.

[95] Sørensen A, Mølmer K. Entanglement and quantum computation with ions in thermal motion [J]. Phys. Rev. A, 2000, 62(2): 022311.

[96] Sackett C, Kielpinski D, King B, et al. Experimental entanglement of four particles[J]. Nature, 2000, 404(6775): 256.

[97] Leibfried D, DeMarco B, Meyer V, et al. Experimental demonstration of a robust, high-fidelity geometric two ion-qubit phase gate[J]. Nature, 2003, 422(6930): 412.

[98] Benhelm J, Kirchmair G, Roos C, et al. Towards fault-tolerant quantum computing with trapped ions[J]. Nat. Phys., 2008, 4(6): 463.

[99] Hayes D, Matsukevich D, Maunz P, et al. Entanglement of atomic qubits using an optical frequency comb[J]. Phys. Rev. Lett., 2010, 104(14): 140501.

[100] Lamata L, León J, Schätz T, et al. Dirac equation and quantum relativistic effects in a single trapped ion[J]. Phys. Rev. Lett., 2007, 98(25): 253005.

[101] Gerritsma R, Kirchmair G, Zähringer F, et al. Quantum simulation of the Dirac equation[J]. Nature, 2010, 463(7277): 68.

[102] Zhang X, Shen Y C, Zhang J H, et al. Time reversal and charge conjugation in an embedding quantum simulator[J]. Nat. Commun., 2015, 6.

[103] Senko C, Smith J, Richerme P, et al. Coherent imaging spectroscopy of a quantum many-body spin system[J]. Science, 2014, 345(6195): 430.

[104] Lee P, Brickman K, Deslauriers L, et al. Phase control of trapped ion quantum gates[J]. J. Opt. B, 2005, 7(10): S371.

[105] Islam R, Ma R, Preiss P, et al. Measuring entanglement entropy in a quantum many-body system [J]. Nature, 2015, 528(7580): 77.

[106] Horodecki R, Horodecki P, Horodecki M, et al. Quantum entanglement[J]. Rev. Mod. Phys., 2009, 81(2): 865.

[107] Hwang M J, Puebla R, Plenio M B. Quantum phase transition and universal dynamics in the Rabi model[J]. Phys. Rev. Lett., 2015, 115(18).

[108] Puebla R, Hwang M, Casanova J, et al. Probing the dynamics of a superradiant quantum phase transition with a single trapped ion[J]. Phys. Rev. Lett., 2017, 118(7): 073001.

[109] Hwang M, Rabl P, Plenio M. Dissipative phase transition in the open quantum Rabi model[J]. Phys. Rev. A, 2018, 97(1): 013825.

[110] Dicke R. Coherence in spontaneous radiation processes[J]. Phys. Rev., 1954, 93(1): 99.

[111] Bastidas V, Emary C, Regler B, et al. Nonequilibrium quantum phase transitions in the Dicke model[J]. Phys. Rev. Lett., 2012, 108(4): 043003.

[112] Bakemeier L, Alvermann A, Fehske H. Quantum phase transition in the Dicke model with critical and noncritical entanglement[J]. Phys. Rev. A, 2012, 85(4): 1073.

[113] Kim M, Lee J, Munro W. Experimentally realizable characterizations of continuous variable Gaussian states[J]. Phys. Rev. A, 2012, 66(3): 355–358.

[114] Toyoda K, Hiji R, Noguchi A, et al. Hong − Ou − Mandel interference of two phonons in trapped ions[J]. Nature, 2015, 527(7576): 74–7.

[115] 薛瑞尼. ThuThesis: 清华大学学位论文模板[EB/OL]. 2017. https://github.com/xueruini/thuthesis.

致　谢

声　明

　　本人郑重声明：所呈交的学位论文，是本人在导师指导下，独立进行研究工作所取得的成果。尽我所知，除文中已经注明引用的内容外，本学位论文的研究成果不包含任何他人享有著作权的内容。对本论文所涉及的研究工作做出贡献的其他个人和集体，均已在文中以明确方式标明。

　　　　　　　　　　　　　　签　名：_____ 日　期：_____

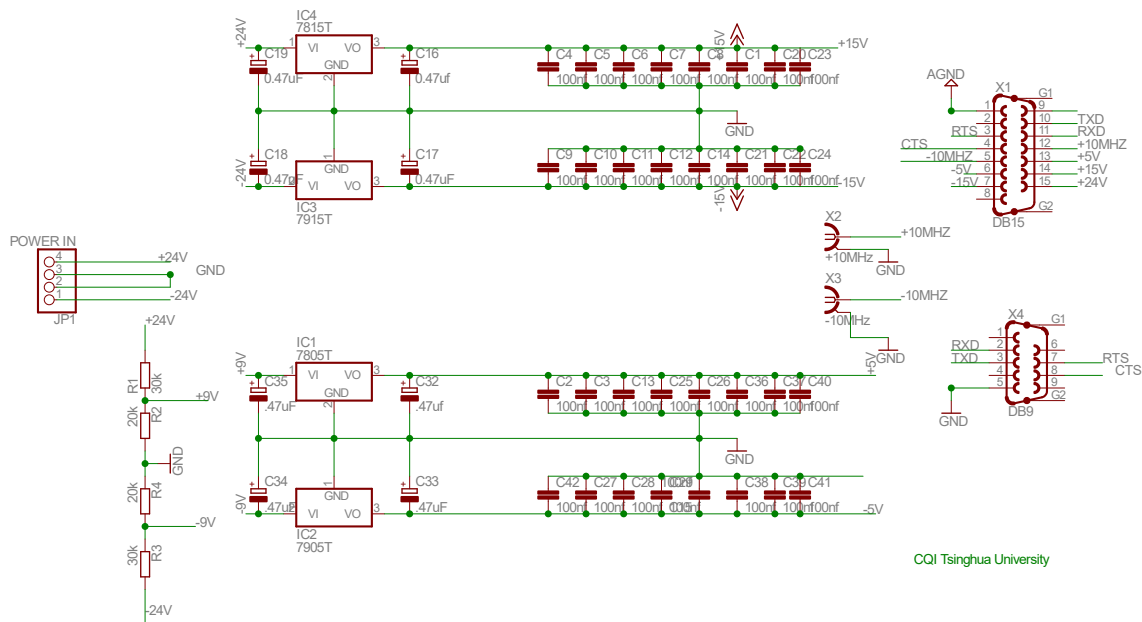# 附录 A   Schematic for the voltage regulator

图 A.1   Voltage regulator for generation of different kinds of voltage

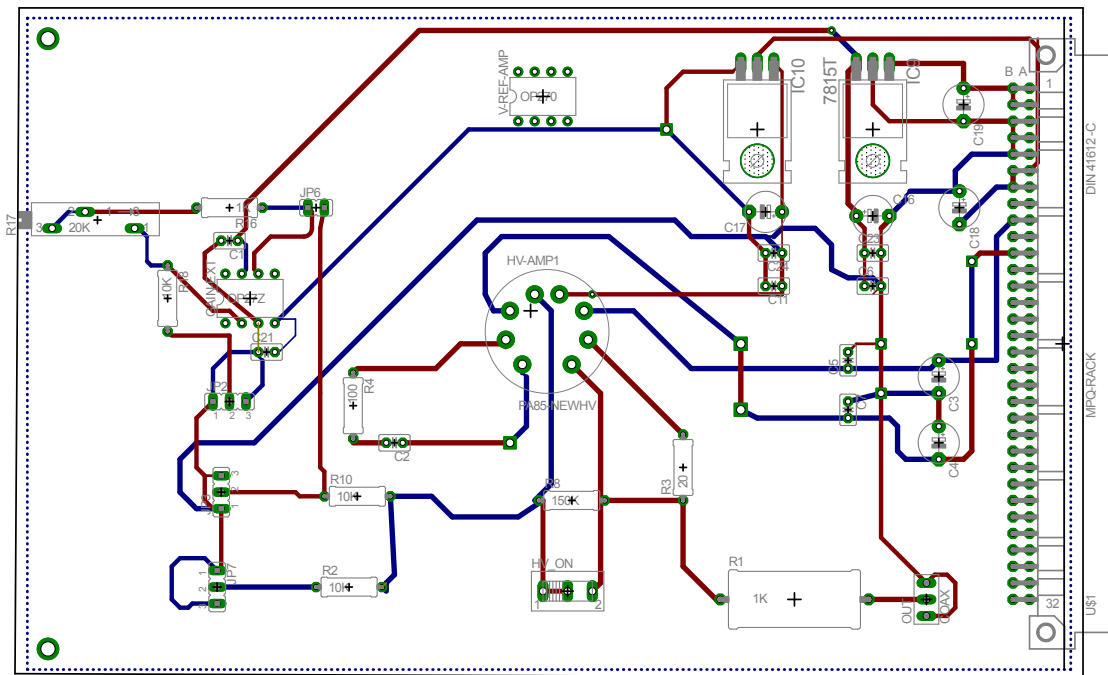# 附录 B   PCB board schematic of the high voltage, fast speed amplifier PA85

图 B.1   PCB board schematic of the high voltage, fast speed amplifier PA85
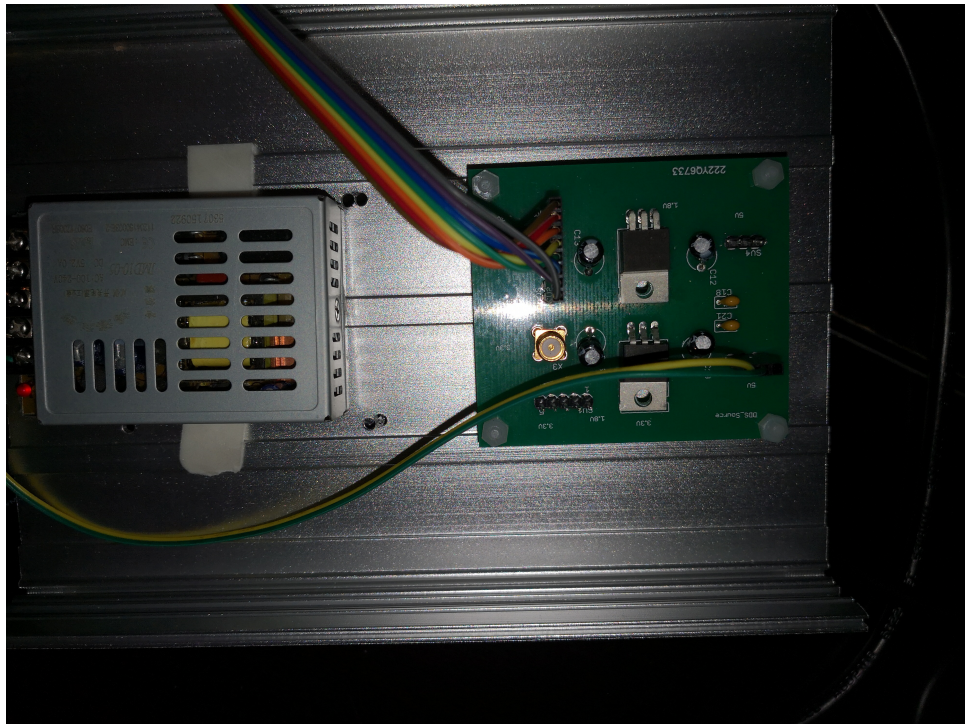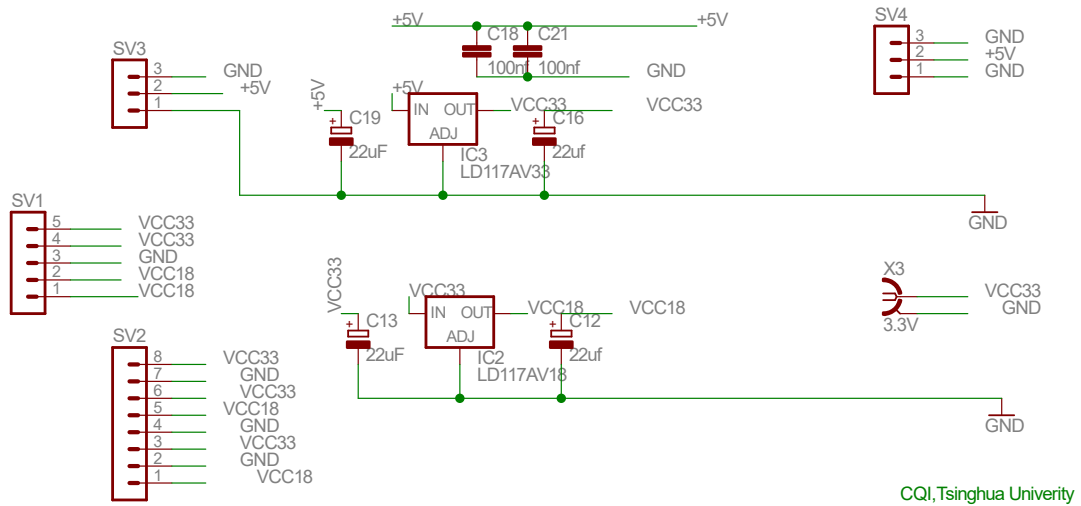
附录 C　DDS source

图 C.1　Schematic of DDS source for the AD9912 and AD9910

附录 D　Verilog code for the DDS control

I have built the Verilog code for the DDS control. We can set the frequency, amplitude throught the message send from LabView. The 8 profiles in the AD9910 make it quite atrractive for the sideband cooling in our multi ion experiments. The evaluation board offers the interface with external control of the DDS through proper set of the jump in the PCB board. When the frequency change speed is not main concern, we can actually directly use it to replace other RF source, which might much expensive. Here I list the core code for in the serial communication mode. Actually, what I did is to simulate the TTL sequence needed to communicate with the evaluation board.

```
1  /* this a single tone test, it is quick no need to communicate
2  with computer and keep send data all the time */
3  /* Keep in mind that EXT_pow_dwn need to connect to Ground always */
4  /* Single internal frequency generation */
5  module AD9910v1(clk,CS,SCLK,SDIO,IO_RST,IO_Update,Master_RST);
6  input clk;
7  output CS,SCLK,SDIO,IO_RST,IO_Update,Master_RST;
8  //F1,F0,TxEnable;//Master_RST-> MasterReset
9  //output Profile0,Profile1,Profile2;
10 reg CS=1,SDIO=0;// ,SCLK=0;//SDIO input only ,not the SDIOO??
11 reg IO_RST,IO_Update,Master_RST;
12 //reg Profile0=0,Profile1=0,Profile2=0;// intend for profile0
13 //reg F1=0,F0=0,TxEnable=1;
14 //for test
15 //output [5:0]State;
16 reg [5:0] State=0;
17 reg [7:0] SPI_State=0;
18 //output [7:0] SPI_State_Counter0;
19 //output [7:0] SPI_State_Counter1;
20 reg [7:0] SPI_State_Counter0=0,SPI_State_Counter1=0;// respective for 32 and 64 b
21 reg [7:0]  Buffer_Address;
22 reg [31:0] Buffer_Data0;// reuse it again in the design
23 reg [63:0] Buffer_Data2;// basically this data can be come from the total 96bit d
24 reg [39:0]CFR1=40'h0;
25 reg [39:0]CFR2=40'h0;
26 reg [71:0]SingTone=72'h0;
27 parameter Initial=4'd0,Start=4'd1,Config=4'd2,IO_Update2=4'd3,Config_Complete=4'd
28 parameter SPI_State0=4'd0,SPI_State1=4'd1,SPI_State2=4'd2,SPI_State3=4'd3,SPI_Sta
29 parameter Address0=8'h00,Address1=8'h02,Address2=8'h0e;
30 /* we intentially set the SDIOO-> SDIO only input ,we do not read it
   or read the value by SDO */
31 parameter Data0=32'h0000_0000,Data1=32'h1F_3F_C0_00,Data2=64'h08b5_8000_3333_3333
32 // just generate the single frequency, no need to communication
33 // parameter Data0=32'hA0A0_3333,Data1=32'h1700_c400,Data2=64'h08b5_0000_3333_3333
34 // just generate 200MHz
```

```
35  parameter Address_Width=8,Data_Width1=32,Data_Width2=64;
36  reg SCLK;
37  reg [1:0] delay=2'b00;// for s short delay;
38  //wire SCLK;
39  //assign SCLK=clk;
40  //output [1:0]sclk_state;
41  reg [1:0]sclk_state=2'b11;// to generate the sclk signal
42  reg [11:0]convert_delay=12'h00;
43  reg [2:0]io_up_delay=3'b000;
44  reg [7:0]master_delay=8'h00;
45  always @(posedge clk)
46  begin
47      case(State)
48      Initial:
49          begin
50              CS <= 1;IO_RST <= 0;
51              IO_Update <= 0;Master_RST <= 1;
52              State <= State+6'd1;
53              SPI_State <= 0;
54              SPI_State_Counter0 <= 0;
55              SPI_State_Counter1 <= 0;
56              //F1 <= 0;F0 <= 0;TxEnable <= 1;
57              Buffer_Data0 <= Data0;
58              Buffer_Data2 <= Data2;
59              Buffer_Address <= Address0;//SPI_State <= 0; send the first 0x00 addr
60              CFR1 <={Address0,Data0};
61              CFR2 <={Address1,Data1};
62              SingTone <={Address2,Data2};
63          end
64      Start:
65          begin
66              master_delay <= master_delay +1;
67              if(master_delay ==10)
68              begin
69                CS <= 0;//maybe here set it 0 much better
70              //increase the master_reset time
71                Master_RST <= 0;
72              // keep in mind that this part we may delay some time if possible
73                State <= State+6'd1;
74                master_delay <=0;
75              end
76              else
77              begin
78                  State <= Start;
79              end
80          end
81      Config:
82          begin
83          //CS <= 0;
84              case(SPI_State)
85              SPI_State0:
86                  begin
87                      //CS <= 0;
```

99

```verilog
88              if(sclk_state==0 | sclk_state == 1)
89              // generate the sclk
90              begin
91                  SCLK <= 1'b1;
92              end
93              else
94              begin
95                  SCLK <= 1'b0;
96              end
97              if (sclk_state == 3)// load data
98              begin
99                  SPI_State_Counter1 <= 0;
100                 if(SPI_State_Counter0 < (Address_Width+Data_Width1))
101                 // config 0x00 register
102                     begin
103                         SDIO <= CFR1[Address_Width+Data_Width1-1];
104                         CFR1 <= CFR1<<1;
105                         SPI_State_Counter0 <= SPI_State_Counter0+8'd1;
106                     end
107                 else
108                     begin
109                         //SDIO <= CFR1[Address_Width+Data_Width1-1];
110                         SPI_State <= SPI_State+4'd1;
111                         CS <= 1'b1; // Insert a delay
112
113                     end
114             end
115             sclk_state <= sclk_state +1;
116         end
117     SPI_State1:
118         begin
119             if( delay < 3)
120             begin
121                 delay <= delay +1;
122             end
123             else
124                 begin
125                     delay <=2'b00;
126                     CS <= 1'b0;
127                     sclk_state <= 2'b11;// reset the sclk_state load
128                     SPI_State <= SPI_State+4'd1;
129                     SPI_State_Counter0 <= 0;
130                 end
131         end
132
133     SPI_State2:
134         begin
135             //CS <= 0;
136             if(sclk_state==0 | sclk_state == 1)
137             // generate the sclk
138             begin
139                 SCLK <= 1'b1;
140             end
```

```verilog
141                        else
142                        begin
143                            SCLK <= 1'b0;
144                        end
145                        if (sclk_state == 3)// load data
146                        begin
147
148                            if(SPI_State_Counter1 < (Address_Width+Data_Width1))
149                            // config 0x00 register
150                                begin
151                                    SDIO <= CFR2[Address_Width+Data_Width1 -1];
152                                    CFR2 <= CFR2<<1;
153                                    SPI_State_Counter1 <= SPI_State_Counter1+8'd1;
154                                end
155                            else
156                                begin
157                                    //SDIO <= CFR1[Address_Width+Data_Width1 -1];
158                                    SPI_State <= SPI_State+4'd1;
159                                    CS <= 1'b1; //Insert a delay
160                                    //IO_Update <= 1;
161                                end
162                        end
163                        sclk_state <= sclk_state +1;
164                    end
165            SPI_State3: // some delay
166                    begin
167                        if( delay < 3)
168                        begin
169                            delay <= delay +1;
170                        end
171                        else
172                            begin
173                                delay <=2'b00;
174                                CS <= 1'b0;
175                                sclk_state <= 2'b11;// reset the sclk_state load
176                                SPI_State <= SPI_State+4'd1;
177                                SPI_State_Counter1 <= 0;
178                                //IO_Update <= 0;
179                            end
180                    end
181            SPI_State4:
182                    begin
183                        //CS <= 0;
184                        if(sclk_state ==0 | sclk_state == 1)// generate the sclk
185                        begin
186                            SCLK <= 1'b1;
187                        end
188                        else
189                        begin
190                            SCLK <= 1'b0;
191                        end
192                        if (sclk_state == 3)// load data
193                        begin
```

101

```verilog
194                        //SPI_State_Counter1 <= 0;
195                        if(SPI_State_Counter0 < (Address_Width+Data_Width2))
196                        // config 0x00 register
197                            begin
198                                SDIO <= SingTone[Address_Width+Data_Width2-1];
199                                SingTone <= SingTone<<1;
200                                SPI_State_Counter0 <= SPI_State_Counter0+8'd1;
201                            end
202                        else
203                            begin
204                                //SDIO <= CFR1[Address_Width+Data_Width1-1];
205                                SPI_State <= SPI_State+4'd1;
206                                CS <= 1'b1; //Insert a delay
207                            end
208                    end
209                    sclk_state <= sclk_state +1;
210                end
211            default:
212                begin
213                    State <= State+6'd1;
214                end
215            endcase
216        end
217    IO_Update2:
218        begin
219            if(SPI_State_Counter1<1) // only IO_Update for one clk
220                begin
221                    CS <= 1;
222                    IO_Update <= 1;
223                    SPI_State_Counter1 <= SPI_State_Counter1+1;
224                end
225            else      // reset them
226                begin
227                    State <= State+6'd1;
228                    SPI_State_Counter1 <= 0;
229                    SPI_State_Counter0 <= 0;
230                end
231        end
232    Config_Complete:
233        begin
234            CS <= 1;
235            //IO_Update <= 0;
236        convert_delay <= convert_delay +1;
237            //State <= 4'd4;// This part should be a Initial
238            if(convert_delay ==4)
239                begin
240                    IO_Update <= 0;
241                end
242            /* if(convert_delay == 500)
243                begin
244                    convert_delay <=12'h000;
245                    State <= 4'd0;// or this two matters?
246                    sclk_state <= 2'b11;//
```

```verilog
247                     end */ //let the program stops here
248                /* else
249                 begin
250                  //convert_delay <=12'h000;
251                    //State <= 4'd0;// or this two matters?
252                    //sclk_state <= 2'b11;//
253                    State <=Config_Complete;
254                 end */
255          end
256       default:
257          begin
258              IO_Update <= 0;
259              CS <= 1;
260              //State <= 4'd4;// This part should be a Initial,otherwise it is a de
261              State <= 4'd0;
262              sclk_state <= 2'b11;//
263          end
264       endcase
265   end
266   endmodule
```

附录 E　Mathematica source code of reconstruction the density matrix from the *Q* function measurement

```
1   Q2WFitting [ Qlist_ : List , dens_ideal_ : List , maxn_: nmax] := Module [
2       {tem , dens_tem , maxN} ,
3       ReIni = Re[ dens_ideal ];
4       ImIni = Im[ den_ideal ];
5       dens_temRe = Flatten [ Table [1/(nmax + 1) , {i , 0, nmax , 1} , {j , 0, nmax , 1}]];
6       dens_temIm = Flatten [ Table [1/(nmax + 1) , {i , 0, nmax , 1} , {j , 0, nmax , 1}]];
7       dr = 0.2;(∗ the step for amplitude ∗)
8       d_Theta = Pi /12;∗ the step for phase ∗)
9       dens = Table [ Re[ a [[ i , j ]]] + i ∗Re[ b [[ i , j ]]] , {i , 0, nmax , 1} , {j , 0, nmax , 1}
10      dens_real = Table [ a [[ i , j ]] , {i , 0, nmax , 1} , {j , 0, nmax , 1}];
11      dens_Imag = Table [ b [[ i , j ]] , {i , 0, nmax , 1} , {j , 0, nmax , 1}];
12      tan = Flatten @ dens_ ;
13      ReInitial = Flatten [ Table [{ a [[ i , j ]] , ReIni [[ i + 1, j + 1]]} ,
14      {i , 0,nmax , 1} , {j , 0, nmax , 1}] , 1];
15      ImInitial = Flatten [ Table [{ b [[ i , j ]] , ImIni [[ i + 1, j + 1]]} ,
16      {i , 0, nmax , 1} , {j , 0, nmax , 1}] , 1];
17      AllIni = Join [ ReInitial , ImInitial ];
18      tem = Sum[ Abs[ Qlist [[ i + 1, j + 1]] − Re[ Exp[−( i ∗dr )^2]∗
19          Sum[ If [ i == 0 && (m + n == 0) , 1∗dens [[m + 1, n + 1]] ,
20          ( i ^(m + n)∗( dr )^(m + n)∗Exp[−I ∗(m − n)∗ j ∗d \[ Theta ]])/ Sqrt [m! n !]
21          ∗dens [[m + 1, n + 1]]] , {m, 0, nmax , 1} , {n, 0,
22          nmax , 1}]]]^2 , {i , 0, 15, 1} , {j , 0, 23, 1}];
23      tem1 = And @@ Table [ dens [[ i + 1, i + 1]] >= 0, {i , 0, nmax , 1}] &&
24      Sum[ dens [[ i + 1, i + 1]] , {i , 0, nmax , 1}] == 1;
25      (∗ tem2=And@@Flatten [ Table [ dens [[ i +1, j +1]]==dens [[ j +1,
26      i +1]]^\[ Conjugate ] ,{ i ,0 ,nmax ,1} ,{ j ,0 ,nmax ,1 } ] ] ; ∗)
27      tem2 = And @@ Flatten [ Table [ b [[ i , j ]] + b [[ j , i ]] == 0, {i , 0, nmax ,1} ,
28      {j , 0, nmax , 1}]];
29      tem3 = FindMinimum [{ tem , tem1 && tem2 } , AllIni , WorkingPrecision −> 4];
30      dens_tem = tem3 [[2]];
31      dens /. dens_tem
32  ];
```

个人简历、在学期间发表的学术论文与研究成果

个人简历

1988 年 7 月 18 日出生于湖南省宁远县。

2008 年 9 月考入哈尔滨工业大学物理系应用物理学专业，2012 年 7 月本科毕业并获得理学学士学位。

2012 年 9 月免试进入清华大学交叉信息研究院攻读理学博士学位至今。

发表的学术论文

[1] **Dingshun Lv**, Shuoming An, Zhenyu Liu, Jing-Ning Zhang, Julen S. Pedernales, Lucas Lamata, Enrique Solano, Kihwan Kim. Quantum simulation of the quantum Rabi model in a trapped ion. *Phys. Rev. X* **8**, 021027 (2018)

[2] **Dingshun Lv**, Shuoming An, Mark Um, Junhua Zhang, Jing-Ning Zhang, M. S. Kim, and Kihwan Kim, Reconstruction of the Jaynes-Cummings field state of ionic motion in a harmonic trap, *Phys, Rev. A* **95**, 043813 (2017)

[3] Shuoming An , **Dingshun Lv**, Adolfo del Campo and Kihwan Kim, Shortcuts to adiabaticity by counterdiabatic driving for trapped-ion displacement in phase space, *Nat. Commun.* **7**, 12999 (2016)

[4] Mark Um, Junhua Zhang, **Dingshun Lv**, Yao Lu, Shuoming An , Jing-Ning Zhang, Hyunchul Nha, MS Kim, Kihwan Kim, Phonon arithmetic in a trapped ion system, *Nat. Commun.* **7**, 11410 (2016)

[5] Shuoming An , Jing-Ning Zhang, Mark Um, **Dingshun Lv**, Yao Lu, Junhua Zhang, Zhang-Qi Yin, H. T. Quan and Kihwan Kim, Experimental Test of Quantum Jarzynski Equality with a Trapped Ion System, *Nat. Phys.* **11**, 193−199 (2015)

[6] Jiyong Park, Junhua Zhang, Jaehak Lee, Se-Wan Ji, Mark Um, **Dingshun Lv**, Kihwan Kim, and Hyunchul Nha, Testing Nonclassicality and Non-Gaussianity in Phase Space, *Phys. Rev. Lett.* **114**, 190402 (2015)